University of California

Los Angeles

Mechanical Entrainment of Saccular Hair Cell Bundles

A dissertation submitted in partial satisfaction

of the requirements for the degree

Doctor of Philosophy in Physics

by

Yuttana Roongthumskul

2014

Abstract of the Dissertation

Mechanical Entrainment of Saccular Hair Cell Bundles

by

Yuttana Roongthumskul

Doctor of Philosophy in Physics

University of California, Los Angeles, 2014

Professor Dolores Bozovic, Chair

Mechanical detection of auditory and vestibular system displays exquisite sensitivity, with sub-nanometer detection threshold. The system is also highly nonlinear, exhibiting sharply tuned frequency selectivity and compression of dynamic range. Detection of sounds and vibrations is mediated by the sensory hair cells, which transduce mechanical inputs into electrical signals via hair bundles' deflections. Experiments have consistently shown that hair bundles are not just passive detectors, as they spontaneously oscillate and respond to mechanical stimulus in an active manner. A number of theories based on nonlinear dynamics have described the active hair bundle as a nonlinear system poised near a Hopf bifurcation. Prior studies of mechanical response of hair bundles were done in spontaneously oscillating hair bundles, with mechanical stimulus fluctuating around bundles' resting positions. These conditions, however, might not be true under *in vivo* conditions. In fact, hair bundles from the bullfrog sacculus are coupled to an overlying membrane, which imposes a steady state offset to the bundle position, and suppresses bundles' spontaneous activity. In this dissertation, we study entrainment of hair bundles from the bullfrog sacculus by sinusoidal stimuli under different mechanical manipulations: offsets and couplings. First, multimode oscillations are more frequently observed upon application of a small negative offset onto spontaneous

oscillating hair bundles. Using a numerical model based on detailed physiology of hair bundle, this complex temporal profile requires an additional element - a variable gating spring - with a stiffness that varies with calcium concentration. The dynamics of the process are slow compared to other timescales in the bundle, i.e. gating of transduction channels and slow adaptation process. Second, oscillating hair bundles subject to weak mechanical stimuli are extremely sensitive, with response in the phase histogram already observed at 0.4-pN stimulus. Time-dependent phase-locking behavior at slightly higher signal amplitudes exhibits phase slips, indicating that the system undergoes phase-locking via a SNIC bifurcation. Study of hair bundle dynamics under mechanical offsets reveals a spiking regime, which is even more sensitive to stimulus compared to the oscillatory regime. Larger mechanical offset yields suppression of spontaneous activity, during which spikes can be evoked by stimulus. Evoked spikes occur at a preferred phase of the stimulus cycle, and exhibit a constant amplitude, regardless of signal amplitude and frequency, and leading to an amplifying movement. Finally, we study how coupling between hair bundles affects their mechanical response. Synchronization of bundles' spontaneous movements is always observed, regardless of the original characteristic frequencies of hair bundles prior to coupling. While some coupled bundles show an enhancement, we find that, in general, coupling only two bundles does not significantly improve the sensitivity and frequency tuning.

The dissertation of Yuttana Roongthumskul is approved.

Amy Rowat

Mayank Mehta

Robijn Bruinsma

Dolores Bozovic, Committee Chair

University of California, Los Angeles

2014

Table of Contents

List of Figures

List of Tables

Acknowledgments

First of all, I would like to express my great appreciation to His Majesty King Bhumibol Adulyadej of Thailand, and Her Royal Highness Princess Maha Chakri Sirindorn, the founder and the director of the Anandamahidol foundation, for granting me the most prestigious scholarship. I would like to thank my advisor Dolores Bozovic for being a great mentor. Thank for the countless hours of stimulating discussions, and her outstanding ability to spot subtle, overlooked features in the data. Without her advice and ideas, this thesis would not have been possible. Thank you to my lab mates past and present for all the great time we spent together. Thank you to Lea Fredrickson, for almost being my second advisor, Elliott Strimbu, Albert Kao, Bas Meenderink, and Yuki Quinones, for helping a theorist learn how to do experiments. Thank you to David Rowland, Marcos Nunez, Jae hyun Lee, Michael Levy, Tracy Zhang, and Elizabeth Mills. I would also like to thank my Thai friends at UCLA for all the fun we had and for always being there for me. Thank you P'Two, P'Ping, P'Knot, and Pink for helping me through my first two years in this country. Thank you P'Ice, P'Na, Nae, Pop, and Tov for our friendships in the land on the other side of the world from our home. Thank you Jenny Lee for her kind support through the tough time I had in the first year. Last but not least, I would like to especially thank my family: my parents, my aunt, and my sisters, for always being very supportive, and for their understanding.

Vita

1986	Born in Bangkok, Thailand.
2008	B.S. (Physics), Chulalongkorn University, Bangkok, Thailand.
2008-2011	Teaching Assistant, Physics and Astronomy Department, UCLA.
2011-present	Graduate Student Researcher, Physics and Astronomy Department, UCLA

Publications

1. Y. Roongthumskul, L. Fredrickson-Hemsing, A. Kao, and D. Bozovic. "Multiple-timescale dynamics underlying spontaneous oscillations of saccular hair bundles" Biophys. J. 101 (2011) 603-610.

2. D. Rowland, Y. Roongthumskul, J.-H. Lee, J. Cheon, and D. Bozovic. "Magnetic Actuation of Hair Cells" Appl. Phys. Lett. 99 (2011) 193701.

3. L. Fredrickson-Hemsing, C. E. Strimbu, Y. Roongthumskul, and D. Bozovic. "Dynamics of Freely Oscillating and Coupled Hair Cell Bundles under Mechanical Detection" Biophys. J. 102 (2012) 1785 - 1792.

4. Y. Roongthumskul, R. Shlomovitz, R. Bruinsma, and D. Bozovic. "Phase slips in oscillatory hair bundles" Phys. Rev. Lett. 110 (2013) 148106.

5. R. Shlomovitz, Y. Roongthumskul, R. Bruinsma, and D. Bozovic. "Phase-locked spiking and stochastic resonance of hair cells" Interface focus. *submitted*

CHAPTER 1

Introduction

1.1 Hearing

Auditory and vestibular organs in the inner ear exhibit remarkable sensitivity, frequency discrimination, and dynamic range. The human ear is sensitive to sound waves ranging from 20 - 20,000 Hz, spanning over six orders of magnitude in sound pressure level [50]. An untrained individual can distinguish two tones differing in frequency by 0.5% [44], indicating an exquisite frequency selectivity. An observation that cochlea is filled with fluid led to the first notion, made by Gold in 1948, that the inner ear must employ an active process in amplifying a weak incoming signal to overcome dampening due to viscosity dampening. Later studies revealed that at the threshold of hearing displayed by the mammalian cochlea, sound evokes vibrations of the sensory epithelium - the basilar membrane - with an amplitude of 0.3 nm, which is smaller than those caused by thermal fluctuations [72]. This level of exquisite sensitivity dropped by 99% post-mortem [71], suggesting the presence of active mechanisms. Moreover, the upper range of sound pressure level (6 orders of magnitude larger than threshold) was found to result in only 10-nm vibrations of the epithelium. This compression of the dynamic range indicated that the inner ear is not only active, but also highly nonlinear. In 1980s, the discovery of otoacoustic emissions - sound emitted from the ear in a quiet environment - confirmed both of these assumptions [51, 65].

Detection of sound and ground vibrations relies on the transduction of a me-

chanical input into an electrical signal [50]. This process of mechano-electrical transduction is performed by hair cells, the detectors of the inner ear. Each hair cell has a cluster of 20-300 stereocilia, called a hair bundle, protruding from its apical surface, shown in Fig. 1.1A. These stereocilia, composed of tightly bound actin cores, are arranged in rows of increasing height, and coupled to nearest neighbors via extracellular links. The tallest row of stereocilia is connected to a kinocilium - the only true cilium in the bundle, composed of microtubules. In hair bundles of some species, including mammals, the kinocilium is present only during development, and then disappears as the hair cells reach maturity. In many organs, hair bundles are coupled to overlying structures, such as the otolithic membrane in the sacculus and the tectorial membrane in mammalian cochlea, which provide mechanical coupling between hair bundles. These sensory epithelia are unique in the configuration of their chemical environment, with the apical side, including hair bundles, immersed in endolymph (high potassium, low calcium), and the basal side exposed to perilymph (low potassium, moderate calcium).

Despite the differences between structures that conduct mechanical stimuli along the auditory pathways and possibly provide mechanical amplification in different species, sound waves ultimately evoke hair-bundle deflections. Displacement of a hair bundle toward taller stereocilia opens transduction channels, mechanosensitive ion channels that resides within the bundle. This leads to an inward ionic current, which depolarizes the hair cell's membrane potential, and further triggers action potentials that get conveyed to the brain. The schematic diagram of the transduction process is shown in Fig. 1.1B. Active motility has been observed in hair bundles from organs in some species [17, 41]. Therefore, hair bundles have been proposed as one of the candidates for the source of active processes and nonlinearity of the inner ear.

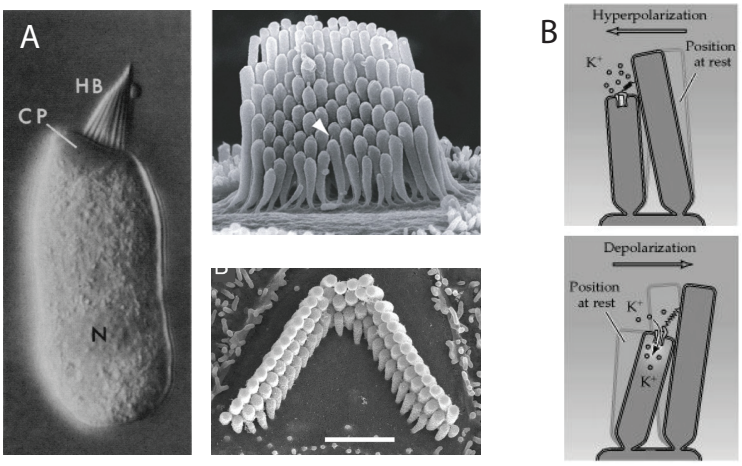

Figure 1.1: Hair bundles and transduction process
(A) Variation in hair bundle morphology. *Left*, an optical image a hair cell from the bullfrog sacculus. Protruding from the cuticular plate (*CP*) at the apical surface of the cell body (*N* denotes nucleus) is the hair bundle (*HB*) [43]. *Top right*, SEM image of a hair bundle from the chicken cochlea [44]. *Bottom right*, top-down SEM image of an outer hair bundle from the rat cochlea [7]. (B) Schematic diagram illustrates transduction by a hair bundle. Deflection of a hair bundle toward the tallest row of stereocilia leads to opening of transduction channels [66].

1.2 Bullfrog Sacculus

In order to study basic principles of the transduction process and detection mechanisms, one must focus on the hair bundles. However, due to technical difficulties in performing experiments on hair bundles from mammalian cochlea, much of our understanding of the bundle functions and dynamics comes from studying hair bundles in lower vertebrate auditory and vestibular organs, especially those from the bullfrog sacculus. The bullfrog sacculus is an auditory/vestibular organ which detects low-frequency sound and vibrations (20-120 Hz) [77]. Hair cells in the sacculus are arranged in a quasi-hexagonal pattern on an essentially flat epithelium, shown in Fig. 1.2A. Hair bundles from the sacculus are naturally coupled to an overlying structure called the otolithic membrane (OM), a $\sim$ 25-30 μm thick, gelatinous layer, via the kinociliary bulbs, shown in Fig. 1.2B. Observations made in [25] showed that the OM imposes not only mechanical coupling to hair bundles,

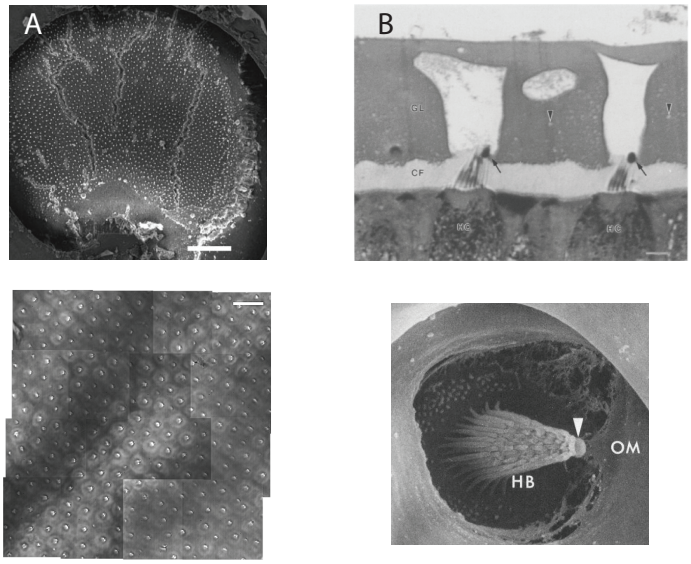

Figure 1.2: Bullfrog saccular epithelium and otolithic membrane
(A) Top-down images of the bullfrog sacculus (*top*: SEM image [80], *bottom*: zoomed-in optical image [67]). The otolithic membrane was removed in *bottom* image. (B) Hair bundles when attached to the overlying otolithic membrane (*top*: optical image of a fixed preparation [48], *bottom*: SEM image [21]).

but also mechanical offsets. Specifically, when attached to the OM hair bundles are pulled towards their kinocilium.

1.3 Saccular Hair Bundles

In this section, elements and function of hair bundles from the bullfrog sacculus are reviewed, including hair bundle morphology, transduction process, and adaptation process. Some of the properties described here also apply to hair bundles from a variety of organs and species.

Hair bundles from the bullfrog sacculus are typically $\sim$ 7-10 μm tall, with $\sim$ 10 μm in diameter. Each bundle is composed of 30-50 stereocilia, with the tallest row connected to a kinocilium. A single stereocilium is thought to be a rigid rod, which tapers at the base with a few tens of actin filaments at the point of insertion in the cuticular plate; hence, the stereocilium only deflects at

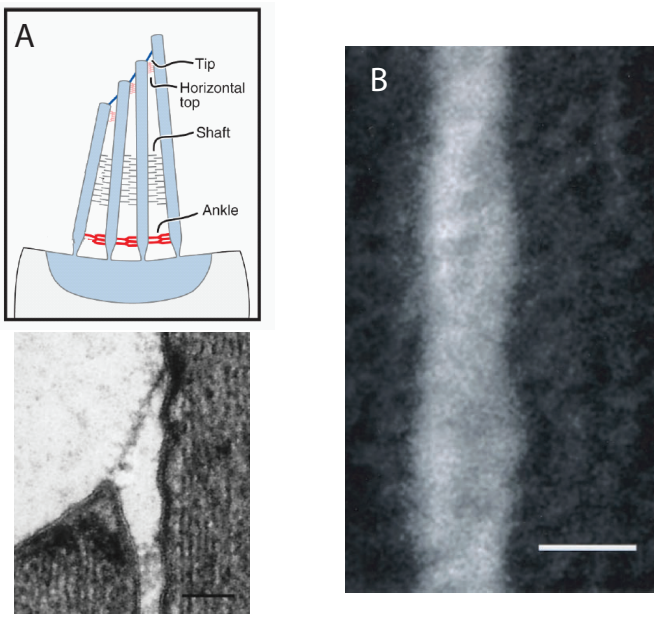

Figure 1.3: Side links and tip link structure
(A) *Top* Schematic diagram illustrates various links between stereocilia [85]. *Bottom* TEM image of a tip link connecting two adjacent stereocilia [49]. Note that the tip link was in a tensed state as the bundle was slightly deflected in the positive direction. (B) Helical structure of the tip link [49].

its base [23]. As mentioned earlier, each stereocilium is coupled to its nearest neighbors via extracellular links at the base of the bundle (ankle links), along the length of the cilia (shaft connectors), and near the tips of the cilia (horizontal top connectors) [85], as shown in Fig. 1.3A. These links ensure coherent motion between the cilia, and the bundle therefore moves as a unit, with no splaying within the bundle [53]. Measurement based on a laser differential interferometry reported the passive stiffness of a bundle as 350 μN/m, and its drag coefficient $\sim$127 nNs/m [18, 53].

Among these extracellular links, the link that governs the transduction process is the tip link, connecting the top of a stereocilium to the side of a taller adjacent cilium, shown in Fig. 1.3A. High-resolution imaging of tip links reveals a helical structure, shown in Fig. 1.3B, with 8-11 nm diameter and $\sim$ 150 nm in length [49]. Study of the molecular composition indicates that the tip links are

composed of cadherin23 at the upper end and protocadherin15 at the lower end. Molecular dynamic simulations suggest an overlap of these two molecules at the site of binding [79], and that the stiffness of a tip link is very large (40-60 mN/m), making it inextensible [78].

Mechano-electrical transduction is mediated by the transduction channels embedded in the membrane of the stereocilia. The exact location of these channels in bullfrog saccular hair bundles is not yet known. Results from calcium imaging indicate that the channels are located at both ends of the tip links [56] (while only on the lower end in mammalian bundles [8]). However, numerical simulations and activation energy calculations suggest that channels should only be on one end of the tip links [82]. Studies on the basic properties of transduction channels show a unitary conductance of 12.7 pS, with a reversal potential close to 0 mV [40]. The channels are also nonselective, allowing an influx of ions up to 1.2 nm in diameter [85].

Application of an abrupt step deflection to a hair bundle evokes an inward transduction current with only 25 μs delay. This rapid response raises the "gating-spring model" which states that the transduction channel is attached to an elastic element called the gating spring. Increasing tension in the tip link due to bundle deflection directly reduces the activation energy and increases the channel opening probability [16, 3]. The activation curve of bundle displacement vs. transduction current is well described by a Boltzmann function, as shown in Fig. 1.4A, indicating that 15%-20% of transduction channels are open at rest. Detailed measurements of channel gating indicate that the channel moves by $\sim$ 2.5 nm upon opening with gating spring stiffness $\sim$ 1000 μN/m, suggesting an additional elastic element in series with the tip link.

In response to a sustained stimulus, transduction current shows a peak corresponding to opening of the channels, then a decay to the resting level with time, as shown in Fig. 1.4B, commonly known as an adaptation process. Application

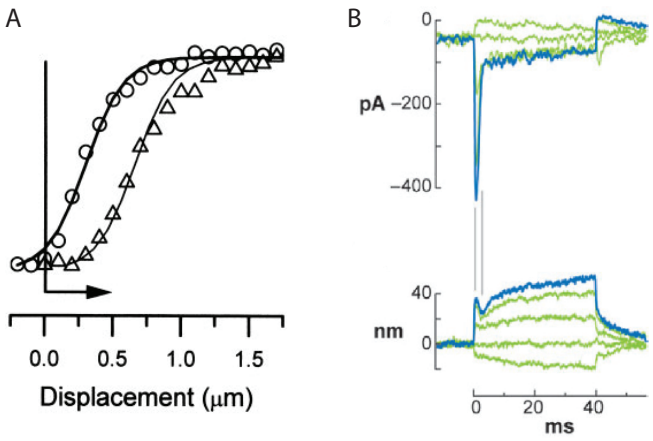

Figure 1.4: Electrical response and adaptation processes
(A) Inward transduction current as a function of bundle displacement (activation curve) of a hair bundle from the bullfrog sacculus [20]. The curve shifts along the displacement axis (following the arrow) in response to a positive prolonged deflection. (B) Adaptation processes observed in the transduction current and the corresponding hair bundle motion [85]. Step deflection was applied from 1 - 40 ms.

of a large step deflection reveals, usually in high-calcium endolymph (4 mM), two distinct adaptation processes: a fast adaptation which completes within a few ms after the peak response in the current, and a slow process that takes place over a few tens of milliseconds [20]. Hair bundle motion associated with the adaptation processes is illustrated in Fig. 1.4B, where fast adaptation results in a "twitch" motion [6, 14]. While the exact mechanism underlying the fast adaptation is still not known, several theories have been proposed, all of which assume that the process are mediated by calcium influx through the transduction channels [14, 10].

The slow adaptation process has been shown to be calcium dependent [21], and corresponds to a shift in the activation curve along the displacement axis in the direction of the stimulus, Fig. 1.4A [21, 35]. The speed of adaptation is shown to be $\sim$ 1-2 μ/s, corresponding to that of myosin motors climbing/slipping along actin. Studies of myosin localization suggest that a myosin 1c complex, located near the transduction channel, is responsible for the slow adaptation process in bullfrog saccular hair bundles [31, 37, 26]. The motor complex is also thought to

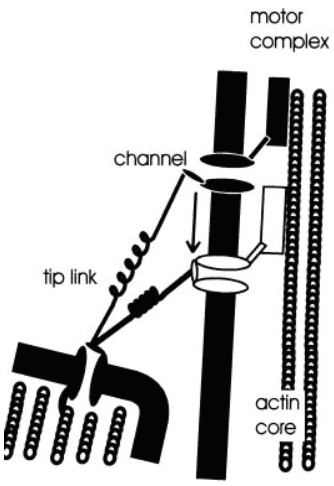

Figure 1.5: Myosin motor model
Schematic diagram of the transduction apparatus. Myosin motor complex can climb and slip along the stereocilia, allowing the repositioning of the channels. As the location of the transduction channels is not exactly known, this diagram posits the channels at both ends of the tip link.

directly anchor to the transduction channel, and be able to move the channel along the plasma membrane of the bundle, thus relaxing or storing tension in the tip link to modify the channel open probability, Fig. 1.5 [41, 30, 27]. Calcium is thought to modulate the adaptation by binding to calmodulin, found to be co-localized with the myosin 1c complex. Slow adaptation appears to be asymmetric, with a greater, constant speed upon positive deflection, and slower, tension-dependent speed in the relaxing direction [35, 74]. However, adaptation is incomplete, as the activation curve moves by only 80% of the stimulus amplitude, with a fixed limit $\sim$ 100-500 nm in the negative direction [74].

1.4 Spontaneous Hair Bundle Motility

Hair bundles from the bullfrog sacculus exhibit spontaneous oscillations under *in vitro* conditions [41]. This phenomenon is described as a result of the interplay between gating of the transduction channels and the slow adaptation [62, 58]. It

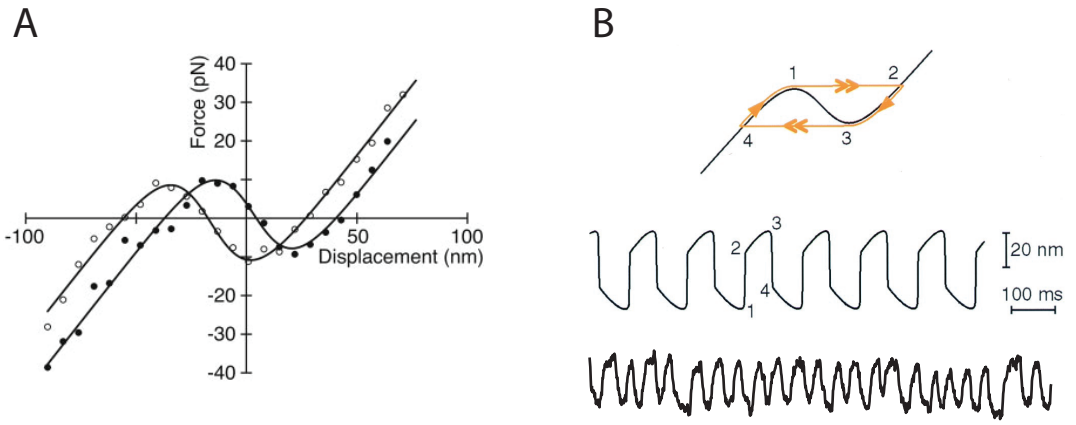

Figure 1.6: Negative stiffness and spontaneous oscillations
(A) Measurement of the force-displacement curve of an oscillating hair bundle in the channel-opening state (filled circles), and -closing state (open circles) [32] shows negative stiffness. Notice the shift due to slow adaptation process. This shift, as illustrated in (B), can results in spontaneous oscillations [62]. Bundle motion obtained from experimental data is shown in the bottom trace of (B).

has been shown that the opening (closing) of the transduction channels is associated with a bundle's displacement in the positive (negative) direction [42]. Thus, within the displacement corresponding to the operating range of the channel, the bundle stiffness appears to be significantly smaller than the actual passive stiffness. Later measurements of the force-displacement curve done in lower Ca^{2+} concentration indicate that this gating compliance leads to a regime of negative stiffness of the bundle, shown in Fig. 1.6A, resulting in an instability [62]. Slow adaptation shifts this curve along the line whose slope corresponds to the stiffness of the bundle's pivot, thus shifting the position of instability [32, 62]. The interplay between these two mechanisms gives rise to a spontaneous oscillation, as shown in Fig. 1.6B.

One can explain the spontaneous oscillations from a biophysical point of view [45]. Starting from a hair bundle in the channel-opening state, calcium influx diffuses from the channel to the binding sites of the adaptation motor, presumably calmodulin in myosin 1c tail domain. Binding of calcium promotes detaching of myosin from actin, causing the whole transduction apparatus, including the

motor complexes along with the transduction channels, to slip downward along the stereocilia. Due to the bundle's geometry, as the insertion point of the upper end of the tip link displaces, the hair bundle additionally exhibits a slow movement in the channel-opening direction. This reduces tension in the tip link, thus relaxing the gating spring, and the transduction channels can close, causing a rapid motion in the opposite direction. Calcium within the bundle then diffuses away and gets extruded through PMCA Ca^{2+} pumps [86], allowing the myosin motors to continue climbing along the actin. Similarly, displacement of the upper end of the tip link causes slow movement of the bundle, and simultaneously builds up tension in the gating spring, such that the transduction channels can reopen. These processes result in a "relaxation oscillation", defined as a rapid excursion followed by a slow movement, as observed experimentally, Fig. 1.6B.

1.5 Mechanical Response of Hair Bundles

Mechanical manipulations on individual hair bundles have been shown to affect the spontaneous oscillation profiles. Stimulations are typically delivered to a hair bundle via a glass fiber attached to the kinociliary bulb, or the top row of stereocilia (details described in Chapter 2). An application of small amplitude sinusoidal stimuli on an oscillating hair bundle results in an entrainment, illustrated as a peak in the Fourier transform at the stimulus frequency, shown in Fig. 1.7A. The degree of phase locking, defined as the fraction of the root-mean-square amplitude of the bundle movement at the stimulus frequency, increases with stimulus amplitude, and eventually saturates, shown in Fig. 1.7B [60]. The stimulus amplitude at which the phase-locking reaches the maximum value becomes larger with a larger mismatch between the stimulus frequency and the characteristic frequency of the bundle.

Analysis of the phase-locked amplitude, extracted from the Fourier transform

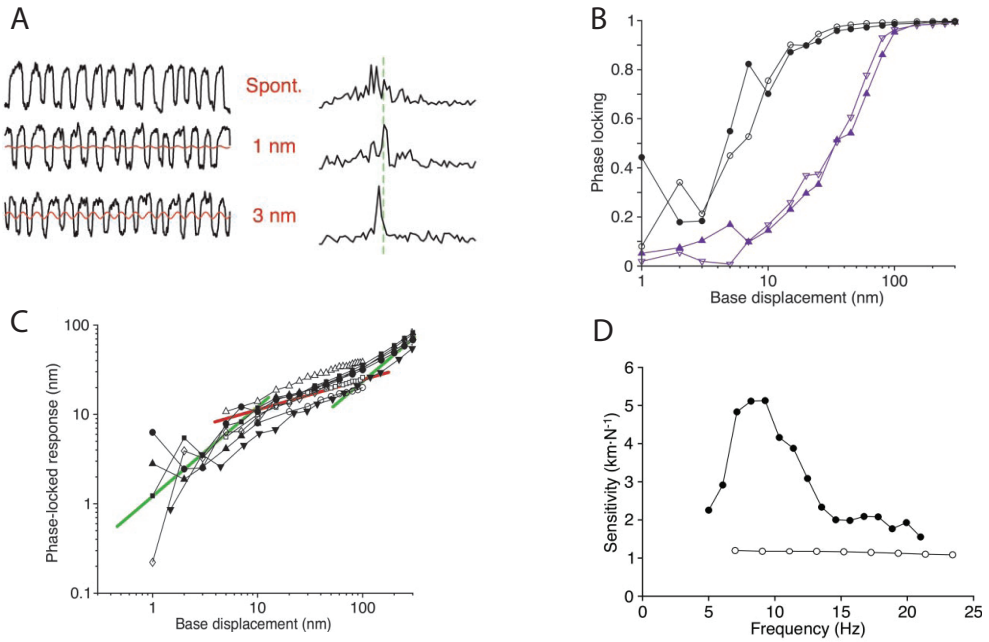

Figure 1.7: Mechanical response of oscillating hair bundles
(A) Hair bundle motion subject to sinusoidal stimuli, shown in red traces. The Fourier transform of bundle motion is shown in the right. Dashed line indicates the stimulus frequency. (B) Degree of phase locking calculated from the Fourier transform of the bundle motion, with the stimulus amplitude close to (circles) and far from (triangles) the characteristic frequency of the hair bundle. (C) Phase-locked response as a function of stimulus amplitude shows the regime of compressive nonlinearity. (D) Phase-locked amplitude of an oscillating bundle (filled circles), and a passive bundle (open circles) at different stimulus frequencies [60]

of the bundle motion at the stimulus frequency, reveals a regime of compressive nonlinearity, during which the phase-locked amplitude exhibits a power-law dependence on the stimulus amplitude, with exponent < 1, illustrated in Fig. 1.7C. Although the exponents observed experimentally vary among bundles, the fit of a one-third exponent seems to capture the behavior of the collective plot shown in Fig. 1.7C, in agreement with the observed basilar membrane response value [72].

Hair bundle response to sinusoidal stimuli of different frequencies, but fixed amplitude, displays a frequency selectivity (Fig. 1.7D), with the peak response corresponding to the characteristic frequency of the bundle, and quality factor of ~ 1. The averaged difference between the phase of the stimulus and that of the bundle oscillation exhibits zero-crossing at the characteristic frequency of the bundle, with a phase lead (lag) for low (high) frequency signal.

Calculation of the work done by a bundle subject to a sinusoidal stimulus confirms that hair bundle oscillations require active work [59], suggesting that the bundle could amplify an incoming signal. Active work is defined as the difference between the dissipative work due to viscous drag , and work delivered from the glass fiber. Another proof of the requirement of an active process for hair bundle oscillations employs the fluctuation-dissipation theorem (FDT), which generally states the condition of a system in thermal equilibrium. Calculation of the response function and the autocorrelation function shows that bundle oscillations violate the FDT, indicating that the system is not in thermal equilibrium [61], thus eliminating the possibility that a hair bundle can be a passive bi-stable system driven by noise.

Resting positions across bundles also significantly affects oscillation profiles. Application of a step deflection on a hair bundle evokes a transient response, with a rapid excursion in the direction of the stimulus followed by a slow movement in the same direction [58], similar to what is observed in a viscoelastic system. The oscillation recovers with a gradually increasing amplitude within 300 ms after the

onset of the deflection (Fig. 1.8A). Hair bundle oscillation under prolonged steady-state offset is shown in Fig. 1.8B. While positive deflection significantly increases the oscillation frequency, negative deflection has the opposite effect. In some hair bundles, the spontaneous oscillations display complex temporal profiles with oscillations interrupted by quiescent intervals. This behavior is more pronounced upon an application of a small negative deflection. This suggests an additional manifold in the bundle dynamics that has not yet been captured in the current models, as described in the previous section.

To explore the continuous change in bundle dynamics under different deflections, slowly varying offset in both positive and negative directions is applied to the bundle [25]. As shown in Fig. 1.8C, large deflections result in asymmetric bundle oscillations, preferring the channel-opening state for positive ramp, and channel-closing state for negative ramp. Spike-like behavior is observed in bundle motion before suppression of the active motility.

1.6 Theoretical Description of Hair Bundle Dynamics

Theories based on nonlinear dynamics have been proposed to describe active hair bundle dynamics. Around 2000, several theoretical studies proposed that mechanical sensitivity of a hair bundle can be explained by tuning the system near a Hopf bifurcation [15, 11], at which a stable fixed point becomes unstable, and a stable limit cycle emerges [81]. This theoretical description was also generalized to the auditory system [22]. Later, the validity of a Hopf bifurcation description was confirmed by the observations of spontaneous oscillations, frequency tuning, and compressive nonlinearity with a one-third exponent [60]. A normal form of a supercritical Hopf (or Andronov-Hopf) bifurcation can be written as [22]

$$\dot{z} = (\mu + i\omega_0)z - |z|^2 z \tag{1.1}$$

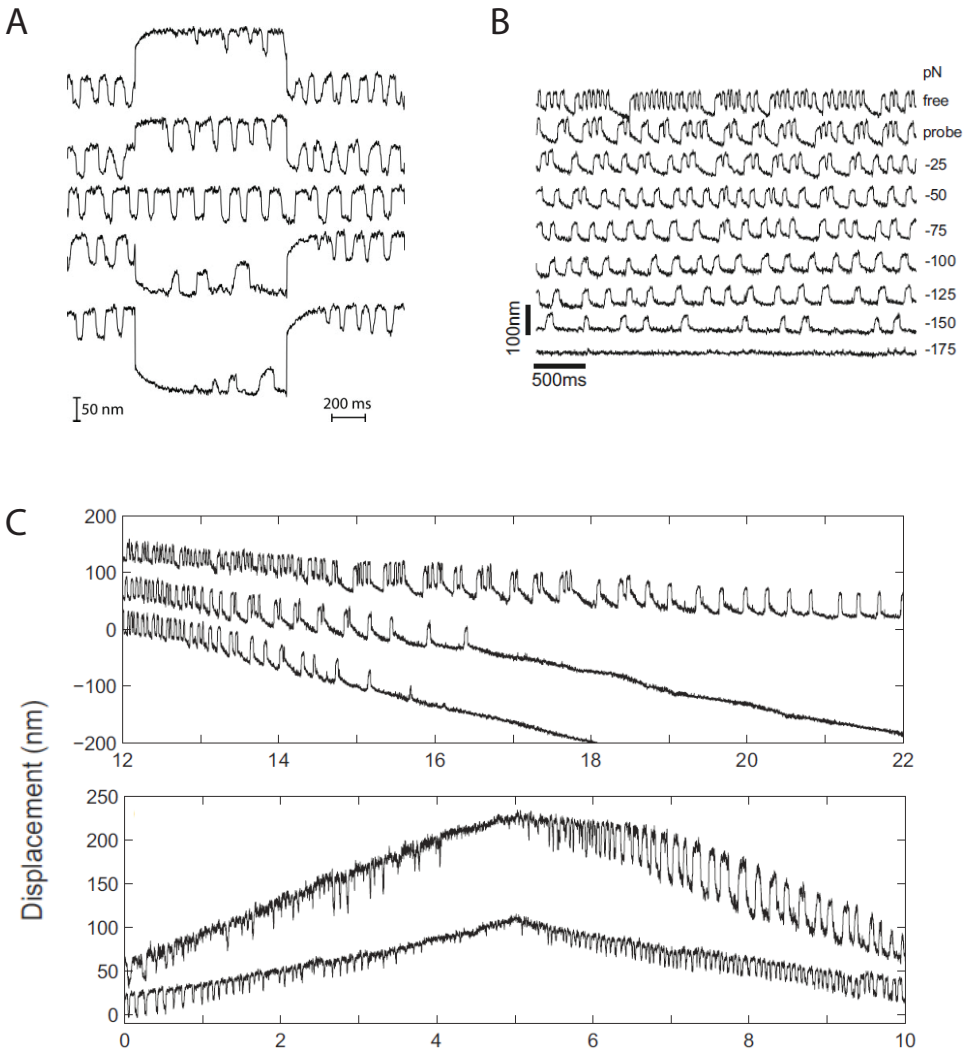

Figure 1.8: Effects of mechanical offsets on spontaneous oscillations (A) Transient response to step deflection [58]. (B) Effects of a steady-state deflection in the negative direction, multimode behavior is more pronounced [75]. (C) Effects of slowly varying offset in both positive and negative directions [25]

where z denotes a complex variable, whose real part is the (bundle) position, and imaginary part is some internal parameter, interpreted as the adaptation and other dynamics in the cell. ω_0 is the characteristic frequency of the system (bundle), and μ is the control parameter. The solution of Eq 1.1 remains quiescent at $z = 0$ when $\mu < 0$, and exhibits limit-cycle oscillation when $\mu > 0$ with amplitude $\sqrt{\mu}$. For hair bundles, this explains the existence of spontaneous oscillations.

In the presence of a driving force, $F = F_0 \exp i\omega t$, the solution of Eq. 1.1 takes the form $z = R \exp i\omega t + i\phi$, with ϕ denoting phase difference. Adding the driving force term to the right hand side of Eq. 1.1, one obtains

$$F^2 = R^6 - 2\mu R^4 + R^2[\mu^2 + (\omega - \omega_0)^2] \tag{1.2}$$

This relation predicts both frequency selectivity and compressive nonlinearity in the response (R). For a system at the bifurcation point ($\mu = 0$), compressive nonlinearity with an exponent of one-third is observed at any stimulus amplitude for small detuning ($\omega - \omega_0$), $R = F^{1/3}$. The system also exhibits amplification for small stimulus amplitude (F <1). For nonzero detuning, the onset of the compressive nonlinearity regime occurs at sufficiently large stimulus amplitude, the magnitude of which grows with detuning, while a small driving force leads to a linear response with constant gain. Including thermal fluctuations in the model yields similar results, with a linear regime at weak signal increasing with noise level [55].

An elaborate treatment of a general form of Hopf bifurcation (both supercritical and subcritical) shows that the exponent of the nonlinear regime varies varies once the system departs from the bifurcation point and for nonzero detuning, and that there always exists a regime of fixed response, independent of the forcing amplitude [55]. This could explain the broad range of exponents observed in experimental data [70].

1.7 Outline of the Dissertation

In this current work, we focus on mechanical entrainment of hair bundle oscillations under different mechanical manipulations, relating to more natural conditions in which hair bundles are coupled to the overlying membrane Details on materials and methods used in this work are explained in chapter 2. As described earlier, the otolithic membrane imposes mechanical offsets onto the bundles, and provides coupling between bundles. As illustrated in Fig. 1.8, multimodal behavior is more pronounced upon application of a small negative offset to spontaneously oscillating bundles. Therefore, in chapter 3, we use numerical simulations to explain the mechanisms underlying this multimodal oscillation. Next, in chapter 4, we study mechanical entrainment of oscillating hair bundles by small sinusoidal stimuli without additional offset, and we compare the experimental data with theories based on nonlinear dynamics. To imitate the effects of the otolithic membrane, in chapter 5 we again explore the dynamics of hair bundles subject to sinusoidal stimuli, now comparing results from varied mechanical offsets. Finally, chapter 6 describes how mechanical coupling between hair bundles affects entrainment.

CHAPTER 2

Materials and Methods

2.1 Biological Preparation

All animal-handling protocols were approved by the UCLA Chancellor Animal Research Committee (Protocol Number ARC 2006-043-13C) in accordance with federal and state guidelines. Adult American bullfrogs (*Rana catesbeiana*) were anesthetised with 200 to 600 μL of 50 mg/mL sodium pentobarbitol, pithed and decapitated. The sacculus from the inner ear was then excised in artificial perilymph, containing 110 mM Na^+, 2 mM K^+, 1.5 mM Ca^{2+}, 113 mM Cl^-, 3 mM D-glucose, 1 mM sodium pyruvate, 1 mM creatine, and 5 mM HEPES. The preparation was mounted into a two-compartment chamber, with the apical side immersed in artificial endolymph (2 mM Na^+, 118 mM K^+, 0.25 mM Ca^{2+}, 118 mM Cl^-, 3 mM D-glucose, and 5 mM HEPES), and the basal side in perilymph. The otolithic membrane was gently lifted off with an eyelash tool after 8-minute enzymatic dissociation with 50 μg/mL collagenase IV (Sigma Aldrich) at room temperature.

2.2 Imaging and Tracking of Hair Bundle Motion

Preparations were imaged under an upright optical microscope (Olympus B51X) with a 20X water-immersion objective (Olympus XLUMPLF20XW). The images were further magnified to 400X with a double-Gauss lens, and recorded at 500-2000 frames per second by a high-speed Complementary Metal Oxide Semiconduc-

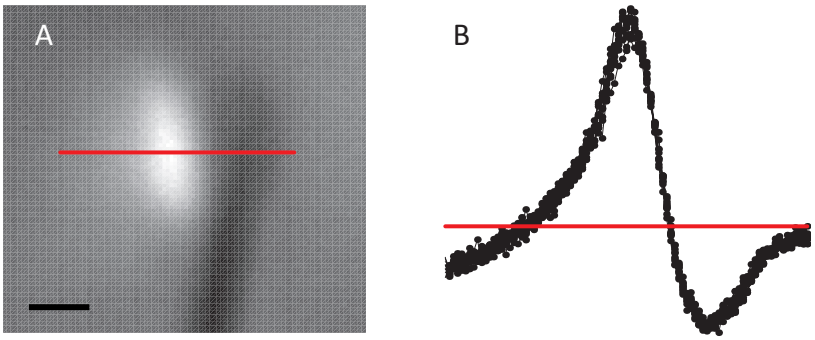

Figure 2.1: Intensity profile and tracking of hair bundle motion.
(A) A top-down optical image of a hair bundle with a glass fiber, appearing as shadow, attached to the tallest row of stereocilia. The scale bar (black) indicates 1 μm distance. The intensity profile corresponding to the red line is shown in (B). (B) Intensity profile of the cross section, with the red line indicating the averaged level of intensity profile. Center of gravity is calculated only from the intensity above the mean level.

tor (CMOS) camera (Photron FASTCAM SA1.1). The spatial scale was routinely calibrated with a 600 linepair per mm Ronchi ruling (Edmund Optics) and was typically $\sim$ 50 - 54 nm per pixel.

Hair bundle motion was extracted from the video records. In each frame, the intensity profile obtained from a row of pixels, parallel to the direction of bundle motion, was subtracted by its average. The bundle position was determined from the center of mass calculated within the window width larger than the range of bundle motion (Fig. 2.1). To improve the signal-to-noise ratio, 10-20 vertically adjacent rows of pixels were tracked and averaged, depending on the size of the bundle imaged.

2.3 Probe Fabrication and Hair Bundle Stimulation

Glass probes were used to mechanically stimulate hair bundles. 1-mm diameter borosilicate glass capillaries (WPI Inc.) were pulled with a Flaming/Brown pipette puller (Sutter Instrument Co.). The fibers were then pulled again at approximately right angles with a custom built microforge to obtain desired probe

stiffness. In experiments that involve coupling of two adjacent hair bundles, the tips of the fibers were then placed $\sim$ 1-2 mm above the microforge, and heated for $\sim$ 1 second. Thermal expansion of the fibers rendered eyelash-shaped-like probes necessary for simultaneously attaching two hair bundles, while avoiding other bundles on the epithelium. To enhance optical contrast, the glass fibers were sputter coated with gold-paladium via a Hummer sputtering system (Anatech, Ltd.).

The stiffness and viscous drag of a fiber were measured using the method following [34]. The equation of motion for the fibers tip is given by,

$$\xi \frac{dx}{dt} + kx = F, \tag{2.1}$$

where ξ, and k are viscous drag, and fiber stiffness, respectively. F represents the Langevin force due to thermal fluctuations. The fiber's mass term is omit since the probes are overdamped. Fourier transform of Eq. 2.1 yields,

$$\tilde{x}(\omega) = \frac{\tilde{F}(\omega)}{k + i\omega\xi}. \tag{2.2}$$

According to the Fluctuations Dissipations Theorem, it can be shown that the Fourier Transform of the Langevin force is given by,

$$|\tilde{F}(\omega)|^2 = 4k_B T \xi_F \tag{2.3}$$

where k_B is the Boltzmann's constant and T is the tempurature. Eq. 2.2 then becomes

$$|\tilde{x}(\omega)|^2 = \frac{4k_B T \xi}{k_F^2 + \omega^2 \xi^2}. \tag{2.4}$$

To estimate the fiber stiffness and viscous drag, the motion of the fiber's tip was recorded in water at room temperature at 10,000 fps for 3 seconds. The trace was divided up into 0.1-s long sections and the Fourier Transform was computed

from each section. The power spectral density was then fitted with Eq. 2.4 in high-frequency limit, to approximate the viscous drag, and low-frequency limit, to approximate the stiffness as follows,

$$\xi = \frac{4k_BT}{\omega^2|\tilde{x}(\omega)|^2}, \qquad \omega \to \infty \tag{2.5}$$

$$\frac{k^2}{\xi} = \frac{4k_BT}{|\tilde{x}(\omega)|^2}, \qquad \omega \to 0 \tag{2.6}$$

Probe stiffness used in all experiments was ∼100 - 200 μN/m. Probes were coated with 2 mg/mL concanavalin-A to enhance the adhesion, then attached to the tallest rows of stereocilia or the kinocilium of hair bundles. For experiments involving large positive offsets, the probes were attached only to the kinocilium which provided better adhesion, possibly due to larger surface area. Probes were mounted at the base to a piezoelectric stack actuator (PiezoJena A4/12) whose amplifier (PiezoJena ENT 400) was controlled with a function generator (Tektronics AFG3022). Mechanical stimuli were sent to the base of the probe.

CHAPTER 3

Multiple-timescale Dynamics Underlying Spontaneous Oscillations of Saccular Hair Bundle

The results of this chapter appeared in the publications:

1. "Multiple-timescale Dynamics Underlying Spontaneous Oscillations of Saccular Hair Bundle" in Biophysical Journal 101 (2011) 603 - 610. The authors are Yuttana Roongthumskul, Lea Fredrickson-Hemsing, Albert Kao, and Dolores Bozovic.

2. "Dynamics of Freely Oscillating and Coupled Hair Cell Bundles under Mechanical Detection" in Biophysical Journal 102 (2012) 1785 - 1792. The authors are Lea Fredrickson-Hemsing, C. Elliott Strimbu, Yuttana Roongthumskul, and Dolores Bozovic.

3. "Magnetic Actuation of Hair Cells" in Applied Physics Letter 99 (2011) 193701 - 3. The authors are David Rowland, Yuttana Roongthumskul, Jae-Hyun Lee, Jinwoo Cheon, and Dolores Bozovic.

3.1 Introduction

Under *in vitro* conditions, hair bundles of the bullfrog sacculus exhibit spontaneous oscillations at amplitudes up to ∼100 nm, at 5 - 50 Hz. We showed previ-

ously that these oscillations are mutually uncorrelated, with frequencies uniformly and randomly distributed across the epithelium [67]. We observed that the majority of active hair bundles exhibit multimode oscillations, with long quiescent periods interrupting oscillatory behavior. Similar to bursting behavior seen in neuronal firing patterns [47], this temporal characteristic indicates the existence of an additional manifold with slower dynamics. Prior numerical simulations in the field have described the more regular limit-cycle oscillations observed in hair bundles loaded with an elastic probe [58, 83, 63]. Our data indicate that freely oscillating bundles may access a different dynamics regime, hence, in this chapter, we propose modifications to the current models to describe the observed complex temporal patterns by introducing a variable gating spring element that includes slow calcium-binding dynamics.

Experiments accompanying numerical simulations in this chapter were performed by Lea Fredrickson-Hemsing, Albert Kao, David Rowland, and Jae-Hyun Lee. We explored the impact of mechanical and ionic manipulation on the oscillation patterns in hair bundles that exhibited this bursting-type behavior. We showed that varying external calcium concentration and imposing a mechanical load affect both the fast component of the oscillations as well as the occurrence of quiescent intervals. We explored these same effects numerically and showed that this additional element in the model captures a rich array of experimental observations.

3.2 Numerical Model

The numerical model used in this work was based upon previous theoretical simulations of hair bundle mechanics [58, 63, 83, 45, 36].

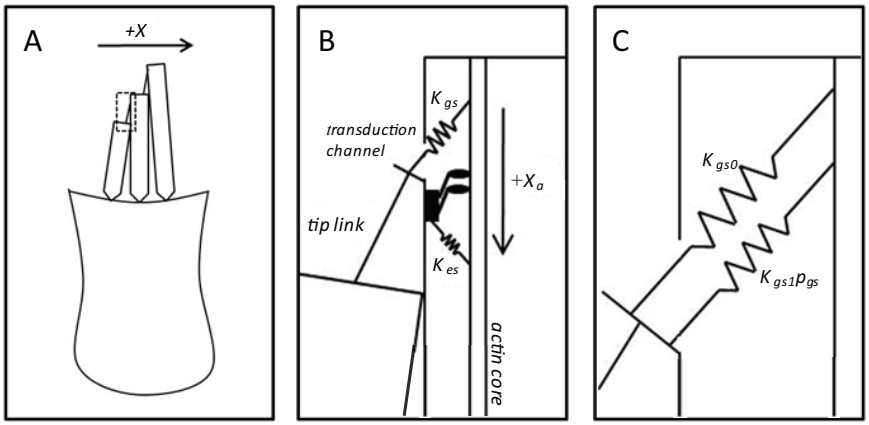

Figure 3.1: Schematic diagram of the mechanical model of a hair bundle. (A) A hair cell with a few of the 30-50 stereocilia that typically comprise a bundle. Horizontal displacement of the bundle is denoted by X, with positive direction chosen to be towards the tallest stereocilia. The transduction complex (dashed box in(A)) is depicted in (B). Displacement of the myosin motors, denoted by X_a, is taken to be positive in the downward direction. We arbitrarily depict the channel to be at the top end in the diagram but note that placing the channel at the lower end of the tip link would not significantly alter the model. The myosin motors are anchored to the insertional plaque near the transduction channel (black rectangle in the diagram). The variable gating spring with stiffness K_{gs} is illustrated in (C). The gating spring consists of two elastic elements in parallel, one of which has a calcium-dependent stiffness ($K_{gs,1}p_{gs}$), while the stiffness of the other element is constant ($K_{gs,0}$). The total stiffness of the combined springs (K_{gs}) is always positive.

3.2.1 Hair bundle mechanics

The hair bundle is modeled as a rigid structure with elastic components. The inertial force is neglected, as the system oscillates in a liquid environment (endolymph) at low Reynolds number. The drag force is proportional to the velocity, with drag coefficient ξ. The main contribution to the stiffness of the bundle arises from the pivots of the stereocilia and the tip links, which connect neighboring stereocilia and attach on one of the ends to the transduction channels. These mechanically gated, nonselective ion channels open and close in response to bundle deflection. A schematic diagram of a hair bundle is shown in Fig. 3.1. We only consider bundle displacement (X) along the axis of sensitivity, corresponding to the direction of increasing height of the stereocilia comprising the bundle. The displacement of the myosin-motor complex along the axis parallel to the stereocilium is denoted by X_a; following convention, the downward direction is defined to be positive. Newton's second law yields the equation of motion for the hair bundle:

$$\xi\frac{dX}{dt} = -N\gamma K_{gs}(\gamma X - X_a + X_c - p_o d) - K_{sp}(X - X_{sp}) + K_f(\Delta - X) + \eta(t) \quad (3.1)$$

The first term on the right represents the tension in the gating spring, where N is the number of transduction channels, γ is the geometrical gain for the hair bundle, K_{gs} is the gating spring stiffness, X_c is the resting extension of the gating spring with all channels closed, p_o is the open probability of the transduction channel, and d is the gating swing distance of the transduction channel. The extension of the gating spring is assumed to be along the stereociliary axis (X_a direction). The second term represents the passive stiffness element of the bundle, with K_{sp} denoting the combined stiffness of all the connections between adjacent stereocilia, as well as their innate stiffness, determined at their pivots. The offset

X_{sp} is the resting position of an unloaded bundle in the absence of gating springs. The next term accounts for the force exerted by an attached glass fiber, where Δ is the displacement of the fiber base and K_f is the stiffness of the fiber. The noise due to stochastic forces acting on the bundle is denoted by η (see Fluctuations in the system).

The transduction channel is described as a two-state system, with its opening probability following the Boltzmann distribution. The energy difference between the open state and the close state has two contributions: the intrinsic energy difference due to the conformational change (ΔE^0) and the extension of the gating spring (d). The channel gating is assumed to be instantaneous, and therefore, the open probability is always in equilibrium with the bundle displacement. At temperature T, the open probability of the transduction channel is

$$p_o = \frac{1}{1 + \exp(\frac{\Delta E^0 - K_{gs} d(\gamma X - X_a + X_c - d/2)}{k_B T})} \tag{3.2}$$

The energy difference ΔE^0 is determined from Eq. 3.2 at the resting value of open probability $(p_{o,0}) = 0.5$.

3.2.2 Calcium influx

During channel opening, a fraction of the cation inflow is carried by calcium ions, which enter the stereocilia and diffuse to the myosin motors to which they bind. The calcium influx through a transduction channel is well approximated by the Goldman-Hodgkin-Katz current equation [38]:

$$I_{Ca} = p_o \frac{P_{Ca} z^2 e F V_M [Ca^{2+}]_{ext}}{k_B T (1 - \exp(\frac{zeV_M}{k_B T}))} \tag{3.3}$$

in which P_{Ca} is the calcium permeability, z is the valence of the calcium ion, e is the electron charge, F is the Faraday constant, $[Ca^{2+}]_{ext}$ is the calcium concen-

tration in endolymph, and V_M is the membrane potential. We assume the resting calcium concentration inside the stereocilia to be negligible, and thus omit it in our equations. In this model, we assume the membrane potential to be a constant.

The calcium ions diffuse rapidly to the binding sites at myosin motors; therefore, the calcium concentration at the motors is assumed to equilibrate instantly to

$$[Ca^{2+}]_{motor} = \frac{-I_{Ca}}{2\pi z F D_{Ca} r_m} \tag{3.4}$$

where D_{Ca} is the diffusion coefficient of a calcium ion, and r_m is the distance from the transduction channel to the myosin motors. Following convention, inward current is defined to be negative.

3.2.3 Adaptation

Calcium binding to the myosin motors affects the stability of their actin binding, and allows them to slip along the actin core in response to the force exerted by the gating spring [28, 39]. The slipping reduces the tension stored in the gating spring and allows the re-closure of the transduction channels. After the calcium ions are instantaneously extruded from the stereocilia during the closed-channel state, the myosin motors restore tension in the gating spring by climbing along the actin filaments.

In the absence of calcium, myosin motors climb along the actin filaments at a constant rate. The slipping rate depends on the tension exerted on the myosin-motor complex by the gating spring, and on the binding of calcium (binding probability p_m). The velocity of the myosin-motor array along the length of a stereocilium is given by:

$$\frac{dX_a}{dt} = -C + S[K_{gs}(\gamma X - X_a + X_c - p_o d) - K_{es}(X_a - X_{es})] + \frac{\eta_a(t)\gamma}{\lambda_a} \tag{3.5}$$

where C is the rate of climbing, S is the rate of slipping, and K_{es} is the stiffness of the extension spring connecting the myosin motors to the actin core. The resting extension of this spring is given by X_{es}, and η_a denotes noise similar to η (see Fluctuations in the system). For simplicity, the rate of slipping (S) is assumed to linearly depend on p_m. Hence,

$$S = (S_{max} - S_{min})p_m + S_{min} \tag{3.6}$$

With the assumption that the dynamics of binding are instantaneous, the binding probability to the motors is given by:

$$p_m = \frac{1}{1 + \frac{k_{m,off}}{k_{m,on}[Ca^{2+}]_{motor}}} \tag{3.7}$$

with $k_{m,on}$ and $k_{m,off}$ denoting the rates of calcium binding and unbinding to the myosin motors. Its resting value ($p_{m,0}$) is calculated from Eq. 3.3, 3.4, and 3.7 at $p_{o,0}$. The climbing rate is constant over time but dependent on $p_{m,0}$: $C = (1 - p_{m,0})(C_{max} - C_{min}) + C_{min}$.

3.2.4 Slow dynamics

We posit a variable gating spring element, intracellularly in series with the tip link, which consists of a constant spring stiffness in parallel with one of variable stiffness (see Fig. 3.1C). Calcium binding to the variable element decreases its stiffness thus rendering the overall gating spring more elastic. For simplicity, we assume the gating stiffness K_{gs} to linearly decrease with the probability of calcium binding (p_{gs}):

$$K_{gs} = K_{gs0} - K_{gs1}p_{gs} \tag{3.8}$$

where K_{gs0} is the gating stiffness in the absence of calcium, and K_{gs1} is the slope of stiffness change with bound calcium.

This variable gating spring introduced here is analogous to a relaxation element previously proposed to capture fast channel re-closure [58, 10]. In contrast, the dynamics of calcium binding and unbinding from the variable gating spring are assumed to be slow with respect to those at the myosin motors, and thus introduce a slow timescale into our system. This binding probability follows the standard rate equation:

$$\frac{dp_{gs}}{dt} = k_{gs,on}[Ca^{2+}]_{gs}(1 - p_{gs}) - k_{gs,off}p_{gs} \tag{3.9}$$

with $k_{gs,on}$ and $k_{gs,off}$ denoting the rates of binding and unbinding of calcium to the variable gating spring. $[Ca^{2+}]_{gs}$ denotes the calcium concentration at this site. The location of this variable gating spring is assumed to be in close proximity to the myosin motors, and therefore $[Ca^{2+}]_{motor} \approx [Ca^{2+}]_{gs}$.

3.2.5 Fluctuations in the system

We incorporate noise terms into our model that were previously shown to play a role in simulated spontaneous oscillations [63]. The noise $\eta(t)$ in the bundle's equation of motion (Eq. 3.1) accounts for channel clatter and hydrodynamic friction. The noise $\eta_a(t)$ for myosin displacement (Eq. 3.5) arises from the force due to the stochastic binding and unbinding of the motors to actin filaments. All the noise terms are assumed to be Gaussian with zero mean, with the fluctuation-dissipation theorem characterizing the autocorrelation function:

$$\langle \eta(t)\eta(0) \rangle = 2k_B T \lambda \delta(t) \tag{3.10}$$

$$\langle \eta_a(t)\eta_a(0) \rangle = 2k_B T \lambda_a \delta(t) \tag{3.11}$$

where λ and λ_a are the friction coefficients of the hair bundle and the myosin motors respectively, following notations in [63]. We neglect any effects of calcium fluctuations.

3.2.6 Simulation protocol

The numerical simulations were performed in MATLAB, using the fourth-order Runge-Kutta method with a time step of 0.1 ms. Table 3.1 lists all of the parameter values used in the simulations presented. The following criteria were used to distinguish regular from complex oscillations: For a noiseless simulation, regular limit-cycle oscillations (referred to as *single-mode oscillation* in the figures) have only one channel-opening and closure per cycle, while bursting-type ones (referred to as *multimode oscillation* in the figures) have multiple open and closed states per cycle. The channels are defined as open if the probability p_o exceeds 0.5 and closed otherwise.

3.3 Results

3.3.1 Complex temporal profile

The phenomenon of spontaneous motility observed in hair bundles of the amphibian sacculus has been characterized by a limit-cycle oscillation [83]. Prior theoretical work has examined the effects of noise on these oscillations, including thermal fluctuations in the ambient water bath, channel clatter, and stochastic binding and unbinding of myosin motors to and from the actin core [63]. Incorporating these noise terms into the system of differential equations describing hair bundle motion captures many of the features experimentally observed in spontaneous oscillations.

Recording with a CMOS camera allows us to track 10-20 hair bundles per

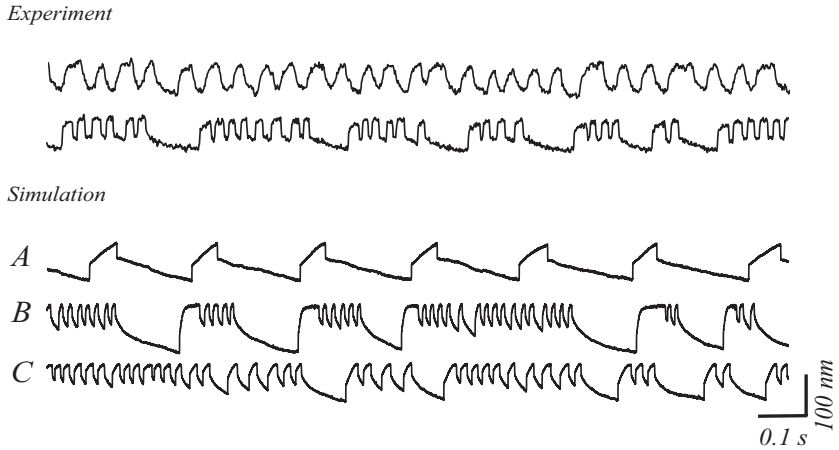

Figure 3.2: Spontaneous oscillation profiles of hair bundles.
Experiment Time-dependent displacement measured in two different hair bundles. The top trace shows an example of a single-mode oscillation with a single dominant period, while the bottom trace shows a multimode oscllation, with oscillatory behavior interspersed with quiescent intervals. (A) Numerical simulation of spontaneous oscillations, with the gating spring stiffness set to be constant. (B) and (C) Examples of two numerical simulations, which display quiescent intervals interspersed with oscillatory behavior as observed in experimental data. Parameters used in simulation of B (C) are those of Cell 1 (Cell 2) in Table 3.1. Numerical simulation shown in (A) used the same set of parameters as in (B), with constant gating stiffness equal to the time-averaged value from (B).

field of view, and hence observe spontaneous oscillations in many cells from each preparation. Secondly, we readily record bundle motion without an attached fiber, thus probing its intrinsic oscillation pattern. The top trace of Fig. 3.2 (*Experiment*) shows an example of a single limit-cycle oscillation. We observed, however, that the majority display complex temporal profiles, with long pauses occurring intermittently with oscillatory behavior as seen in the bottom trace of Fig. 3.2 (*Experiment*). The intervals of quiescence can last hundreds of milliseconds and typically show a slow negative movement of the bundle, indicative of the climbing phase of the myosin.

To capture the intermittent pauses, or multi-mode oscillatory behavior, we include a variable gating spring - an elastic element of tunable stiffness, hypothesized to be in series with the tip link. We assume the calcium dependence of the

variable gating stiffness to be linear. Further, to account for the slow modulation of the oscillatory behavior, we assume the kinetics of calcium binding and dissociation to and from this element to be slow with respect to that of the myosin motor complex. Fig. 3.2, B and C show examples of simulations for two sets of parameters (representing 2 simulated "cells") which yield complex oscillatory behavior qualitatively similar to experimental observations. Without the inclusion of the variable gating spring, the multi-mode oscillation is not observed: Fig 3.2A shows a simulation performed with the same set of parameters as in Fig 3.2B but with a constant gating stiffness, set to equal to the time-averaged gating stiffness of the simulation in Fig 3.2B.

In general, a multimode oscillation does not arise in a two-dimensional system as it would show trajectory crossings in a two-dimensional phase portraits. Hence, we introduce a third dimension into the system by including a variable gating spring in the model. An example of a three-dimensional phase portrait of a noiseless multi-mode oscillation is shown in Fig. 3.3. The system moves along the trajectory in a clockwise direction from a top-down view: the higher peak of the velocity corresponds to the first opening of the channels after a quiescent interval; the bundle subsequently deflects in the positive direction as myosin motors slip; upon channels closing, the bundle position drifts in the negative direction before the channels re-open, corresponding to the lower peak in the velocity. Note that the openings and closings of the channels occur at different positions of the adaptation motors.

In Fig. 3.4, we show traces from a simulation demonstrating the effects of noise on the active bundle motility predicted by the model. The top traces in both A and B show spontaneous oscillations for two simulated cells, without the inclusion of noise terms. Effects of thermal jitter and stochastic attachment and detachment of myosin motors to and from the actin filaments are introduced into the simulations shown in the bottom traces. As can be seen from the records, noise can strongly

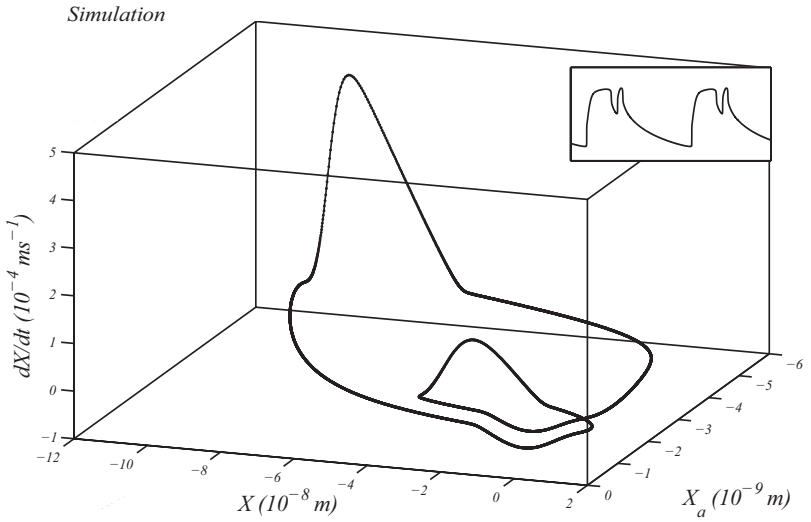

Figure 3.3: Phase portrait of a simulation of a noiseless multimode oscillation. Parameters used in the simulation are those of Cell 3 in Table 3.1.

affect the oscillation profiles. Fig. 3.4*A* illustrates a case where the addition of noise changed the behavior of a simulated cell from that of regular oscillation to one with sporadic quiescence. For other choices of parameters (example shown in Fig. 3.4*B*), the presence of noise only introduces variation in the timing of the quiescent intervals. This indicates that the bursting-type behavior is sensitive to the choice of model parameters, and is affected by the inclusion of noise terms.

3.3.2 Parameter dependence of multiple oscillatory behavior

With the inclusion of slow calcium dynamics, our numerical simulations capture the bursting-type behavior observed experimentally; the effect was however sensitively dependent upon the choice of parameters. We therefore systemically varied key parameters in the simulations without the inclusion of noise terms, to determine the range of values for which the oscillations were single-mode oscillation, multi-mode oscillation, or entirely suppressed.

The impact of calcium binding upon the variable gating stiffness and on the myosin motor activity was seen to play an important role in determining the

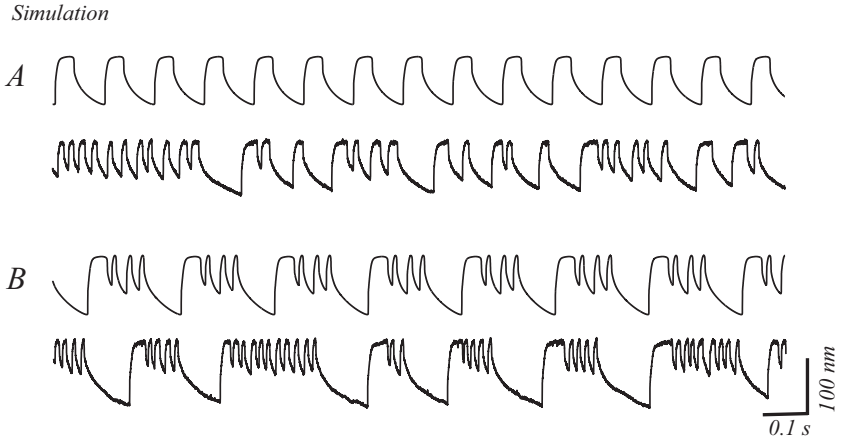

Figure 3.4: Simulations of the effects of noise on the oscillation profiles. For each panel, the top trace shows a simulation of a noiseless spontaneous oscillation. The corresponding bottom traces show simulations obtained with the same set of parameter values, but with noise terms added. (A) The oscillation becomes multi-mode in presence of noise (parameters of Cell 4, Table 3.1), while the noise only causes the irregular occurrence of the quiescent intervals in (B) (parameters of Cell 1 in Table 3.1).

motile behavior. Fig. 3.5 shows a summary plot, where S_{max} (maximal slipping rate of myosin motors) and K_{gs1} (slope of the gating stiffness change with calcium binding) were incrementally varied. As shown in the figure, qualitatively different oscillation profiles were observed in different regimes of the parameter space. Varying these parameters simultaneously is analogous to the experiment in which the calcium concentration in the endolymph is changed, as S_{max} and K_{gs1} describe the calcium sensitivity of the myosin motor complex and the variable gating spring, respectively.

In Fig. 3.6, we plot the results of a numerical study where the stiffness of the stereocilary pivots (K_{sp}) and the offset position of the bundle due to the stereociliary pivots (X_{sp}) were systematically varied in the model. The steady-state terms were found to have a profound effect upon the oscillation profiles, as illustrated in the diagram. These numerical results are consistent with our experimental observations [24], where imposed offsets were shown to modulate and even suppress spontaneous oscillations in hair bundles (example shown later in Fig. 3.9). This parameter space also corresponds to the experiment where the overall stiffness of the bundle is manipulated by imposing a mechanical load on the bundle (examples shown later in Fig. 3.10).

In Fig. 3.7, we plot the time evolution of key parameters (X, p_m, and p_{gs}) during a simulated multimode oscillation. We find that the transduction channel's opening probability varies through most of its full range during the fast component of the oscillation. Probability of calcium binding to the myosin motors (Fig. 3.7B) likewise shows the full range of modulation. Binding probability to the variable gating spring, on the contrary, shows only partial modulation during the fast cycles (as seen in Fig. 3.7C). Consistent with the imposed slow dynamics, modulation reaches its full extent only over the slower timescales that include the quiescent intervals.

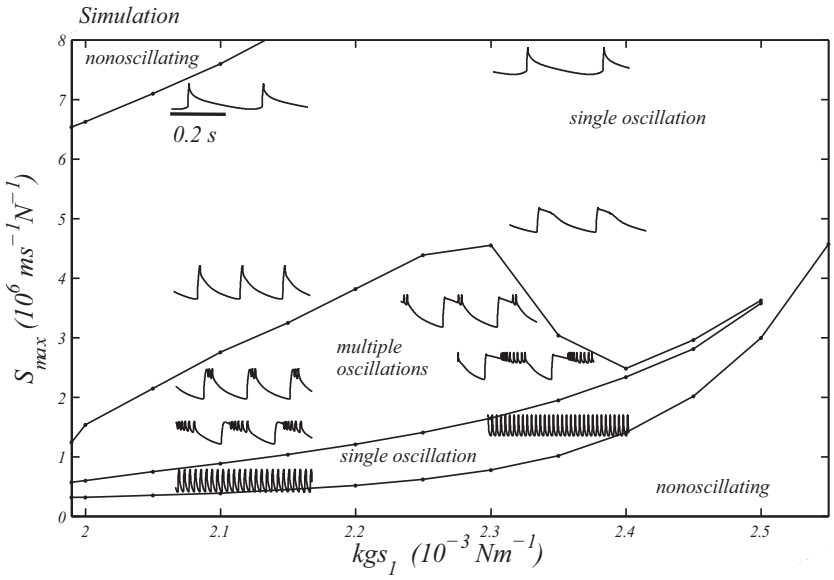

Figure 3.5: Oscillation profiles over the parameter space of S_{max} and K_{gs1}. The diagram shows various states of the hair bundle: stable (*nonoscillating*), oscillating with regular patterns (*single-mode oscillation*), or showing complex bursting-type behavior (*multimode oscillation*). Examples of the oscillations with different parameter values are shown in the insets located in regions that correspond to their parameters values. The horizontal scale bar indicates 0.2 second time interval for all of the oscillations shown. The displacement of each oscillation is independently scaled. Note that the two non-oscillating regions are due to different stabilities: in the low-S_{max} region, most of the channels stay open, and in the high-S_{max} region, most of the channels remain closed. Regimes that show single-mode oscillation likewise show different patterns, though no sharp transition exists at high K_{gs1}. The region with S_{max} higher than that of the '*multimode oscillation*' region shows spike-like profiles with periodicity determined by the quiescent interval and the region with lower S_{max} shows only fast component of the oscillations. Parameters used in the simulation are those of Cell 1 in Table 3.1.

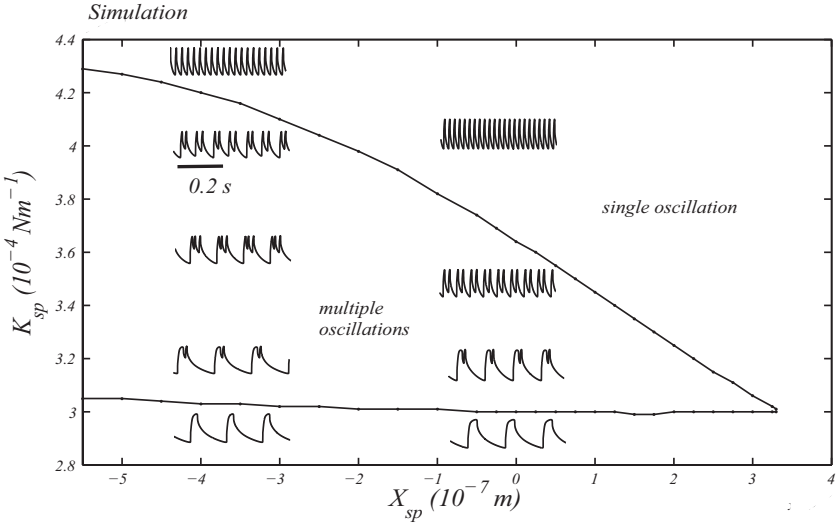

Figure 3.6: Oscillation profiles over the parameter space of K_{sp} and X_{sp}.
The diagram determines the '*multimode oscillation*' and '*single-mode oscillation*' states of the hair bundle, as in Figure 4. Examples of oscillations are illustrated in the insets located in the areas corresponding to their parameter values with the same scale bar indicating 0.2 second time interval. The '*single-mode oscillation*' region with high K_{sp} shows only fast oscillations, while the '*single-mode oscillation*' region with low K_{sp} shows oscillations with a dominant slow period. Parameters used in the simulation are those of Cell 1 in Table 3.1.

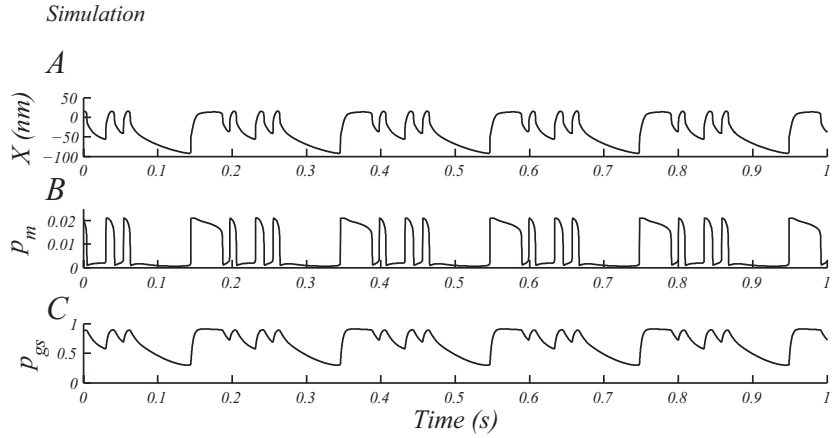

Figure 3.7: Plots of the parameter variation from the simulation of a noiseless oscillation.
Data obtained from oscillations shown in Fig. 2B. (A) The position of the hair bundle (X). (B) The probability of calcium binding to the myosin motors (p_m). (C) The probability of calcium binding to the variable gating spring (p_{gs}). Notice that the decay of p_{gs} during the channel-closed state is significantly slower than that of p_m, illustrating the slow dynamics of calcium binding at the variable gating spring. Parameters used in the simulation are those of Cell 1 in Table 3.1.

3.3.3 Effects of external calcium concentration

Previous experiments have shown calcium to have a strong effect on the active motility of hair bundles: increasing its concentration in endolymph causes a reduction in the amplitude and an increase in the frequency of spontaneous oscillation [58, 6]. We measured the effects of this ionic manipulation on motile hair bundles that displayed multimode oscillatory pattern. The faster component of the oscillation showed an increase in the characteristic frequency. Notably, the duration of the open channel state was more strongly affected than that of the closed state, resulting in a spike-like profile. The duration of the quiescent intervals were, on the contrary, only slightly shortened by the increase in calcium. Fig. 3.8*A* shows an example of measurements in which the concentration of calcium in endolymph solution was incrementally raised; Fig. 3.8*B* shows numerical simulations under the same conditions. As can be seen from the traces, the model captures the impact of the ionic manipulation on both the fast and slow components of the oscillation profile.

3.3.4 Mechanical offsets imposed on the bundle position

Mechanical offsets imposed on the bundle position were seen to strongly affect its oscillatory behavior, as it can serve as a dynamic parameter that tunes the frequency of spontaneous oscillation and induces a bifurcation crossing from oscillatory to the quiescent state. Fig. 3.9*A* shows the results of an experiment in which a steady-state offset was imposed on a bundle with a flexible glass fiber, and Fig. 3.9*B* shows the accompanying numerical simulation. Consistent with the experimental observations, deflections in the negative direction reduce the number of oscillations during each burst and extend the duration of the quiescent intervals. Deflections in the positive direction, on the contrary, eliminate the quiescent intervals and result in single-mode oscillations. Similar behavior during

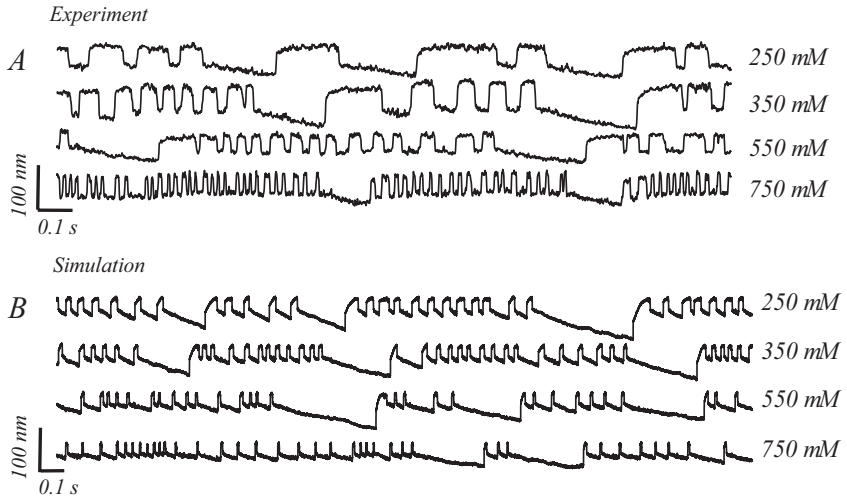

Figure 3.8: Effects of calcium concentration in the endolymph upon characteristics of the oscillation.
(A) Experimental records of spontaneous motility obtained from the same hair bundle under 4 different calcium concentrations: 250, 350, 550, and 750 μM. (B) Numerical simulations under the same calcium concentrations as in the experiment. Both display similar effects: at higher concentration, the fast component of the oscillation becomes faster and smaller in amplitude, while the slow component does not show a significant change. Parameters used in the simulation are those of Cell 5 in Table 3.1.

the transitions between the multi- and the single-mode regime was observed upon applying continuously varying offsets on the resting bundle position, as shown in Fig. 3.10*Experiment*. In the experiment, mechanical force was exerted on micron-sized ferromagnetic magnetite (Fe_3O_4) particles (Thermo Scientific) attached to a hair bundle using a permanent magnet. This allowed us to observe oscillation profiles at different offsets without effects from viscous drag imposed by the glass fiber. Our numerical model reproduced both the transitions in oscillation profiles due to continuously increasing (Fig. 3.10 *Simulation, middle trace*) and decreasing (Fig. 3.10 *Simulation, lower trace*) offsets. This behavior is also illustrated in Fig. 3.6 which examines numerically effects analogous to the imposed offsets. Positive steady-state deflections shift the system from multimode oscillation to single-mode oscillation regime. Moderate negative offsets maintain bursting-type behavior while increasing the duration of the quiescent interval. Further offsets eliminate the short-period component of the oscillations, leading to a single-mode oscillation with a spike-like pattern.

Application of larger offsets enabled us to explore the oscillation profiles near the suppression of the spontaneous activity. As shown in Fig 3.11 *Experiment*, where a triangle wave offset was applied to the bundle, large positive (negative) deflection led to a spike-like bundle motion with preferential channel-opening (-closing) state. The recovery of the spontaneous oscillations exhibited history dependence, with the onset of oscillations occurring at bundle positions larger that of the suppression (Fig. 3.11 *Experiment,B*). The numerical model well captured the behaviors observed experimentally both during positive (Fig. 3.11 *Simulation, A*), and negative (Fig. 3.11 *Simulation, B*) offset.

3.3.5 Stiffness of the mechanical load

Multi-mode oscillations are more often observed in unencumbered bundles than those under an external load. In Fig. 3.12*A*, we illustrate three measurements

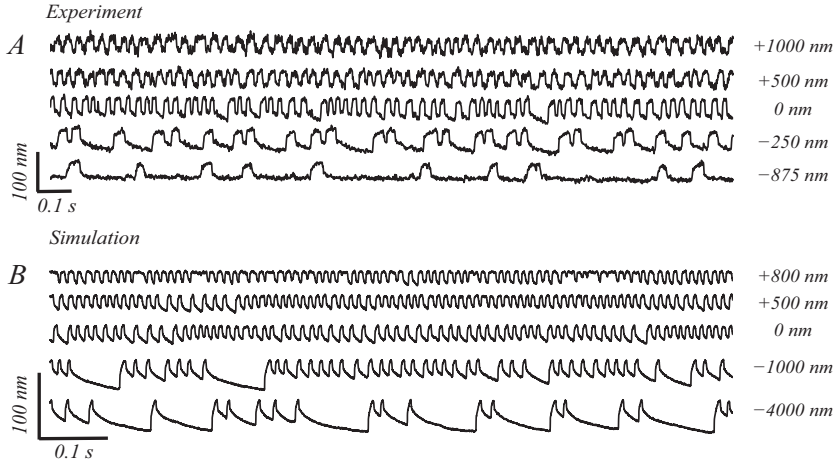

Figure 3.9: Effects of steady-state offsets imposed on an oscillating hair bundle. (A) Experimental records, where constant deflections were imposed on the bundle via a glass probe of stiffness 100 μN/m. (B) The corresponding numerical simulation. For offsets in the positive direction, the oscillations are faster and smaller and the quiescent intervals disappear. In the negative direction, however, the quiescent intervals occur more frequently and eventually become the dominant component of the oscillation profile. Parameters used in the simulation are those of Cell 1 in Table 3.1.

of spontaneous bundle motility before and after the attachment of a glass probe. With light loading, the occurrence of quiescent intervals was reduced, while the higher-frequency components remained unchanged (Fig. 3.12A, *left*). Stronger loading led to a reduction in the amplitude and an increase in the characteristic frequency of oscillation, and eliminated the occurrence of quiescent intervals (Fig. 3.12A, *middle*). Further increase in the stiffness of the load (Fig. 3.12A, *right*) led to a near-suppression of innate oscillations. Fig. 3.12B displays the numerical simulations corresponding to these experiments. The stiffness of the attached load (K_f in Eq. 3.1) was incrementally increased in the calculation to capture the full range of effects. The numerical simulations reproduce all the main features of the experimental data: quiescent pauses are suppressed, the oscillation frequency increases, and the amplitude decreases. This is analogous to an increase in the parameter K_{sp}, leading to a crossing from multi- to single-mode oscillatory regimes shown in Fig. 3.6.

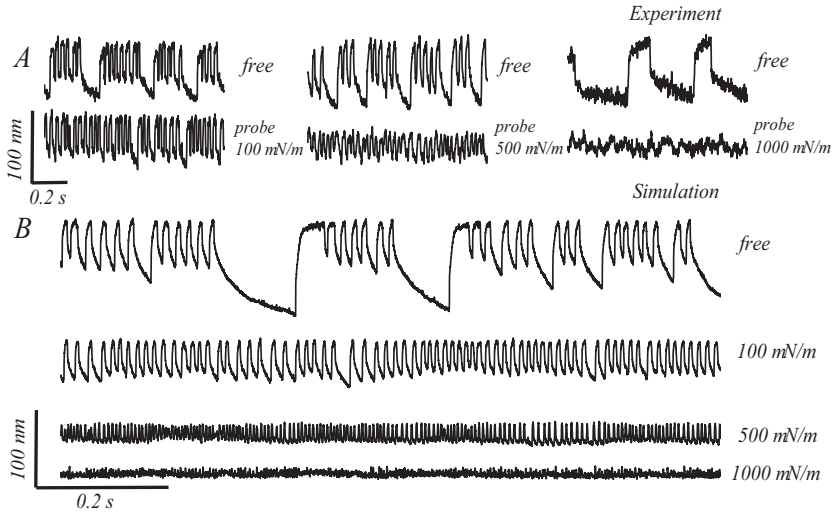

Figure 3.10: Effects of mechanical loading.
Data were obtained experimentally (A) and theoretically (B). The top traces in each of the panels in (A) represent the oscillation profiles of free bundles. Upon light loading, 100 μN/m, the quiescent intervals disappear (A, *left*); with an intermediate load, 500 μN/m, the oscillations become fast and small (A, *middle*); heavy loading, 1000 μN/m, finally suppresses the oscillation (A, *right*). The simulations of hair bundle oscillations under the same set of loading conditions captures the full range of behavior (B). Parameters used in the simulation are those of Cell 1 in Table 3.1.

3.4 Conclusion

Direct gating of transduction channels in the stereocilia has been established as the fundamental mechanism behind mechano-sensation in hair cells. Tip links connecting neighboring stereocilia were proposed to comprise the gating spring and introduced into numerical models to explain the nonlinear mechanical response [42, 29]. Recent molecular dynamic simulations indicated however that the tip link itself is far too stiff to constitute the putative gating spring [78]. As the structural integrity of the tip link and its connection to the transduction channel is crucial for the proper detection of sound [44], it must constitute one of the elements of the full mechano-electrical transduction complex. An elastic element in series with the tip link would be consistent with both sets of results.

The numerical model presented in this chapter incorporates a variable gating spring, composed of a spring of constant stiffness in parallel with one of calcium-dependent compliance. As there are 30-50 stereocilia in a hair bundle, each with a gating spring, and potentially multiple calcium binding sites on each element, the linear term constitutes the simplest mean-field approximation for the calcium-dependent stiffness of the gating spring. Possible coorperativity of calcium binding to multiple sites on the variable gating spring is not considered in this model. Also note that the variable gating spring might be interpreted as any spring element within a bundle that regulates the degree of nonlinearity of the system.

The dynamics of calcium association and dissociation from the proposed variable gating spring are assumed to be slow with respect to other timescales in the system, most notably that of the myosin motor activity. Introduction of a slow dynamic into our model allowed us to reproduce the complex temporal patterns, observed in hundreds of spontaneous oscillations recorded in the course of these experiments.

To characterize the factors determining the temporal profiles of spontaneous

motility, we explored the space of key parameters in the model and classified the resultant oscillations. We found a strong dependence on calcium sensitivity of the variable gating stiffness and on the rate of myosin-based adaptation. Hence, any cellular mechanism that would fine-tune the internal calcium concentration would affect the steady-state gating spring stiffness and thus have a strong impact on the oscillation dynamics. Ion channels found in the hair cell soma were shown to form an electronic circuit that can exhibit resonance, tuning, and spontaneous voltage oscillations [46, 73]. In a previous publication [68], we showed that inhibiting or modulating the activity of the somatic system qualitatively changed the temporal profiles of the spontaneous mechanical oscillations of the bundle. Somatic ion channels comprise a possible control system via the membrane potential that could modulate internal calcium levels and thus affect the variable gating stiffness [36].

Offsets imposed on the resting position of the bundle or of the adaptation motors were seen to profoundly influence oscillation characteristics in the simulations. This is consistent with our experimental findings that steady-state deflections can regularize, modulate, or entirely suppress spontaneous oscillations [25]. In chapter 5, we also study of deflections on mechanical entrainment of individual hair bundles. The effects of calcium and steady-state mechanics may be inter-linked in the hair cell, with offsets in the bundle position introduced by stiffening or softening of internal gating elements, modulated in turn by calcium binding.

Table 3.1: Parameter values in simulations

Parameter	Definition	Cell1	Cell2	Cell3	Cell4	Cell5
r_m (nm)	Distance from the transduction channel to adaptation motor	20	100	20	20	20
N	Number of transduction channels			45		
γ	Geometrical gain of stereociliary shear motion			0.14		
d (nm)	Distance of gating spring relaxation on channel opening			7		
$p_{o,0}$	Resting open probability of transduction channels			0.5		
$k_{m,on}$ ($\times 10^6$/sM)	The rate of calcium binding to the adaptation motor	30	10	30	10	10
$k_{m,off}$ ($\times 10^3$/s)	The rate of calcium unbinding from the adaptation motor	15	5	15	5	5
S_{max} ($\times 10^6$m/sN)	The maximal rate constant for slipping adaptation	0.64	0.8	0.8	0.55	0.4
S_{min} (m/sN)	The minimal rate constant for slipping adaptation			0.5		
C_{max} ($\times 10^{-6}$m/s)	The maximal rate constant for climbing adaptation	0.058	0.04	0.058	0.055	0.02
C_{min} (m/s)	The minimal rate constant for climbing adaptation			0.5		
X_{sp} (nm)	Resting deflection of stereociliary pivots	236	200	236	190	200
X_{es} (nm)	Resting deflection of extension spring	0	40	0	20	0
X_c (nm)	Resting extension of gating spring with channel closed	17	16	17	15	14
K_{es} (μN/m)	Stiffness of extent spring			140		
K_{sp} (μN/m)	Stiffness of stereociliary pivots	310	550	310	330	300
K_{gs0} (μN/m)	Stiffness of gating spring in the absence of calcium	2550	3000	2550	2200	2650
K_{gs1} (μN/m)	The slope of stiffness change with bound calcium	2000	2800	2000	1600	2100
$K_{gs,on}$ ($\times 10^6$/sM)	The rate of calcium binding to the variable gating spring	30	60	30	30	5
$K_{gs,off}$ (1/s)	The rate of calcium unbinding from the variable gating spring	30	50	30	33	3.3

CHAPTER 4

Phase-Locking Behavior of Individual Hair Bundles With No Additional Offset

The results of this chapter appeared in the publication Phase Slips in Oscillatory Hair Bundles in Physical Review Letters 110 (2013) 148103. The coauthors are Roie Shlomovitz, Robijn Bruinsma, and Dolores Bozovic.

4.1 Introduction

4.1.1 Mechanical response of oscillating hair bundles: Analysis based on phase-locked amplitude

Mechanical stimulation of single hair bundles by sinusoidal force of intermediate amplitude (∼1-10 pN) was previously shown to exhibit a regime of compressive nonlinearity [60]. The phase-locked component of the bundle response, obtained from the Fourier transform of the bundle motion at the stimulus frequency, showed a one-third power-law dependence on the stimulus amplitude. Smaller stimulus amplitudes resulted in a linear response. Furthermore, the onset of the compressive nonlinearity regime also happened at higher stimulus amplitude for larger frequency mismatch between the stimulus and that of the bundle. This observed behavior is in agreement with a theoretical description of a dynamical system being poised at or near a supercritical Hopf bifurcation in the presence of noise.

Our recent study observed an Arnold tongue in the phase-locked amplitude

of the bundle response over a broad range of stimulus amplitude and frequency, suggesting the validity of the normal form equation of the supercritical Andronov-Hopf bifurcation [24]. This generalized the bifurcation description of oscillating hair bundles, since the normal form equation also exhibited a saddle-node bifurcation on an invariant circle (SNIC) at small stimulus amplitudes, where the oscillation amplitude of the stimulated bundle remained unaffected.

While the previous studies focused on the phase-locked amplitude of the bundle response, the phase behavior remained unexplored. Therefore, in this chapter, we studied the phase dynamics of stimulated single hair bundles at small stimulus amplitudes.

4.1.2 Stochastic Adler equation

The Adler equation describes the phase-locking behavior of a driven system crossing a SNIC bifurcation. It can be obtained from the normal form of Hopf bifurcation in the limit of weak stimulus.

$$\dot{z} = (\mu + i\omega_0)z - |z|^2 z + Fe^{i\omega t} \tag{4.1}$$

where the real part of z represents the bundle motion, and F is the amplitude of the external stimulus. μ, ω_0, and ω are the control parameter, the characteristic frequency of the bundle oscillation, and the stimulus frequency, respectively [22, 81].

We seek the response of hair bundle to external sinusoidal stimulus of the form $z = re^{i\phi}$, where r is the phase-locked amplitude of the bundle response, and ϕ is the phase of the bundle oscillation. We define the phase difference between the stimulus and the bundle oscillation as

$$\Delta\phi(t) = \phi(t) - \omega t \tag{4.2}$$

Substituting the expected solution for z into Eq. 4.1, one obtains expression of phase-locked amplitude and phase difference.

$$\dot{r}(t) = \mu r(t) - r(t)^3 + F\cos\Delta\phi(t) \tag{4.3}$$

$$\Delta\dot{\phi}(t) = -\Delta\omega - \epsilon\sin\Delta\phi(t) \tag{4.4}$$

with $\Delta\omega = \omega - \omega_0$ a frequency detuning, and $\epsilon = \frac{F}{r}$ a coupling strength [64].

Without stimulus, the steady-state solution for r becomes $\mu^{1/2}$, for positive μ. This solution also yields a good approximation for stimulus force smaller than $F \ll \mu^{3/2}$. Therefore, in this limit, external stimulus only affects the phase dynamics of the system, while the oscillation amplitude remains constant.

The Adler equation, Eq. 4.4, describes the dynamics of phase difference of a driven oscillator near SNIC bifurcation as an over-damped particle moving under a tilted washboard potential, a periodic potential energy landscape with a tilt due to frequency detuning ($\Delta\omega$) [64, 84].

Close to a bifurcation, the Adler equation predicts a characteristic behavior of phase difference, called phase slips, during which a sudden shift of 2π is observed [84]. The duration between phase slips and their direction depends on the frequency detuning. Positive phase slips (gaining 2π) occur with positive detuning. As the detuning becomes smaller, phase slips occur less frequently with the dependence $\tau \sim |\Delta\omega - \Delta\omega_c|^{-1/2}$, where τ represents the average duration between successive phase slips, $\Delta\omega_c$ denotes the detuning at which the complete phase locking occurs [9].

In the presence of noise, the stochastic Adler equation reads

$$\Delta\dot{\phi}(t) = -\Delta\omega - \epsilon\sin\Delta\phi(t) + \eta(t) \tag{4.5}$$

where the noise term η satisfies $\langle \eta(t)\eta(t') \rangle = 2T\delta(t-t')$, with T an effective noise temperature [33].

In [2], Ambegaokar *et al.* presented a treatment of thermally activated phase slips in Josephson Junctions. Converting to notation used in our system, the tilted washboard potential is obtained from an integral of Eq. 4.4.

$$U = -\Delta\phi\Delta\omega - \epsilon\cos\Delta\phi \tag{4.6}$$

In the limit of small detuning, in the presence of noise, $\frac{\Delta\omega}{\epsilon} \to 0$, the frequency of phase slips is given by

$$\nu_{ps} = \frac{\Delta\omega}{2\pi}[I_0(\frac{\epsilon}{T})]^{-2} \tag{4.7}$$

where I_0 is the modified Bessel function of the first kind.

Also in this limit, the phase-locked amplitude can be estimated from the ensemble average:

$$|\tilde{X}(\omega)| = \langle r\cos(\Delta\phi)\rangle = r\frac{\int\cos(\Delta\phi)\exp(-\frac{U}{T})d(\Delta\phi)}{\int\exp(-\frac{U}{T})d(\Delta\phi)} = r\frac{I_1(\epsilon/T)}{I_0(\epsilon/T)} \tag{4.8}$$

where the integrals are computed over the range [0,2π]. I_0 and I_1 are modified Bessel functions of the first kind, and r is the measured amplitude of spontaneous oscillations.

The analytic form of the effective diffusion coefficient calculated from the Adler equation is given by [69]

$$D_{eff} = D_0 4\pi^2\frac{\int dx I_{\pm}(x)I_{+}(x)I_{-}(x)}{[\int dx I_{\pm}(x)]^3} \tag{4.9}$$

where

$$I_{\pm}(x) = \int dy\exp\{\pm[U(x)-U(x\pm y)]/T\} \tag{4.10}$$

and $U(x) = \Delta\omega x - \epsilon\cos(x)$ is the tilted washboard potential. x and y denote the phase difference $\Delta\phi$. All the integrals are computed over the range [0,2π].

4.2 Materials and Methods

Experimental setups used in this work are as described in chapter 2. Mechanical stimulations were sent to the base of the glass fiber attached to the top row of stereocilia. The probe stiffness was $\sim$ 100-150 μN/m.

4.2.1 Data analysis : Phase determination

We utilize the phase portrait of the hair bundles displacement and velocity to extract its instantaneous phase of oscillation. The motion of the bundle is low-pass filtered at 100 Hz cutoff frequency, with offset removed. Any slow drift in the bundle motion is subtracted by fitting a polynomial of the second order to the displacement; therefore, the zero crossings of the oscillations occur roughly half-way between the open and closed states. Five-point derivative of the bundle motion is then numerically calculated to obtain the velocity. The bundle velocity is proportional to the oscillation frequency ($\dot{\phi}$), which is estimated from the duration between zero crossings, in each cycle of the oscillation. The instantaneous phase is determined by $\phi = \arctan(\frac{1}{\dot{\phi}}\frac{\dot{x}}{x})$. The phase is then unwrapped, and the phase of the stimulus (ωt) is subtracted to obtain the unwrapped phase difference.

4.2.2 Data analysis : Estimation of effective diffusion coefficient

In the absence of external stimulation, the phase of hair bundle oscillation exhibits diffusive behavior. The diffusion coefficient (D) is defined as

$$\langle(\phi(t+\tau) - \phi(t))^2\rangle_t - \langle\phi(t+\tau) - \phi(t)\rangle_t^2 = 2D\tau \tag{4.11}$$

where $\langle ... \rangle_t$ denotes time average. The diffusion coefficients of the hair bundle oscillations are extracted from a log-log plot of $\langle (\phi(t+\tau) - \phi(t))^2 \rangle_t$ vs τ by fitting a linear function of slope one. The diffusion coefficient is determined from the intercept.

4.3 Results

In this chapter, we focused on the nonlinear response of spontaneously oscillating hair bundles to a weak stimulus so that it had only a negligible effect on the amplitude of innate motility. No additional mechanical offset was superposed to the stimulus. We observed that the spontaneous oscillations can intermittently phase lock to weak drives, leading to a staircase structure in $\Delta\phi(t)$, characteristics of a class of nonlinear systems. We demonstrated the presence of phase slips, studied the statistics of their occurrence under various drive amplitudes, and detuning ($\Delta\omega$), and compared the measurements to theoretical predictions based on the stochastic Adler equation.

4.3.1 Ensemble response to weak stimuli

At low amplitudes of stimulation (0.2 - 3 nm at the base of the stimulus fiber), individual traces of hair bundle motion seemed unaffected, with the noisy innate oscillation dominating over the sinusoidal signal (Fig. 4.1A). Upon averaging over multiple presentations, a phase-locked signal emerged (Fig. 4.1B), indicating that the drive affected the statistics of the phase distribution. In Fig. 4.1C, we present a two-dimensional plot of the time-dependent probability distribution of $\Delta\phi$. The distribution was obtained from 45 presentations of the stimulus. The stimulation amplitude was 1.7 nm, corresponding to the force amplitude (f_0) of $\sim$ 0.4 pN exerted on a perfectly stationary bundle.

The stimulus frequency ω was close to the natural frequency ω_0 of the hair

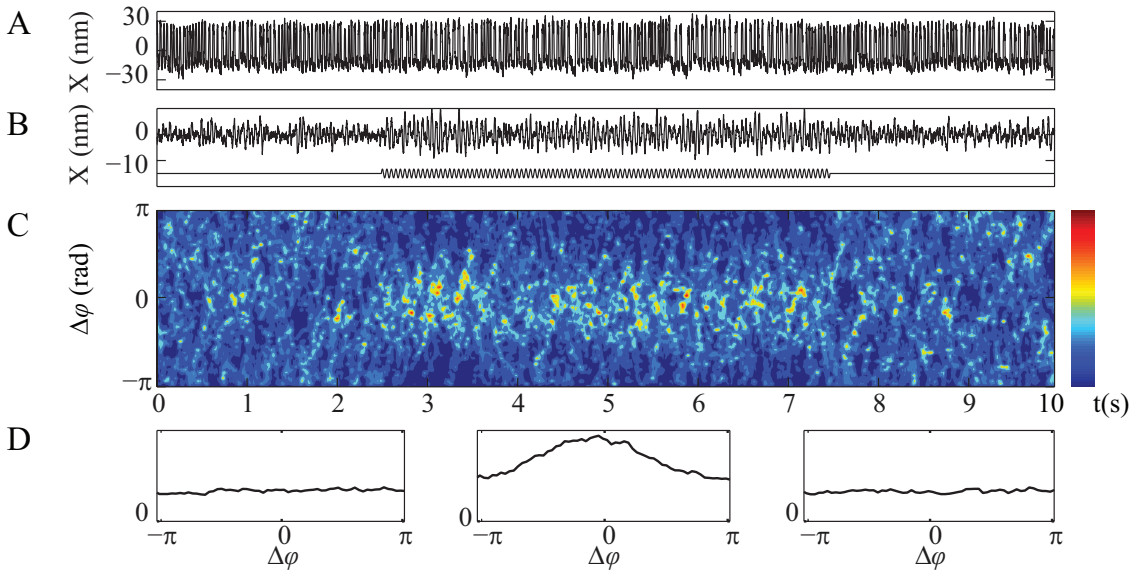

Figure 4.1: Contraction of the phase distribution induced by a weak stimulus. (A) An example of hair bundle spontaneous oscillations with 1.7 nm stimulus applied from 2.5 to 7.5 seconds ($\omega = 20$ Hz, $\omega_0 = 21.5$ Hz). (B) The averaged response of the bundle (top), performed over 40 presentations, and the stimulus profile (bottom). (C) Time-dependent histogram of $\Delta\phi(t)$. The color-coded scale indicates the height of the histogram in arbitrary units. (D) Time-averaged histogram, in arbitrary units, of $\Delta\phi(t)$ before (left), during (middle), and after the stimulation (right). Histograms of freely oscillating, and driven interval are averaged over 2.5 and 5 seconds, respectively.

bundle. Note that the statistical distribution of the phase contracts during the stimulus. Time averaged phase distributions for both the free and driven system are shown in Fig. 4.1D.

The probability distribution of $\Delta\phi(t)$ acquired a more complex structure when the hair bundle was driven by the slightly higher amplitude of 2.5 nm ($f_0 \sim$ 0.5 pN) at $\omega > \omega_0$ (15 and 7.5 Hz, respectively). Fig. 4.2 shows histograms of $\Delta\phi(t)$. During applied stimulus, the phase probability distribution displayed plateaus (Fig. 4.2B), indicating the existence of intervals of phase locking that were separated by integer multiples of 2π.

In Figs. 4.2A and 4.2C, the same analysis was applied to records taken before and after application of the stimulus, respectively, with the instantaneous phase

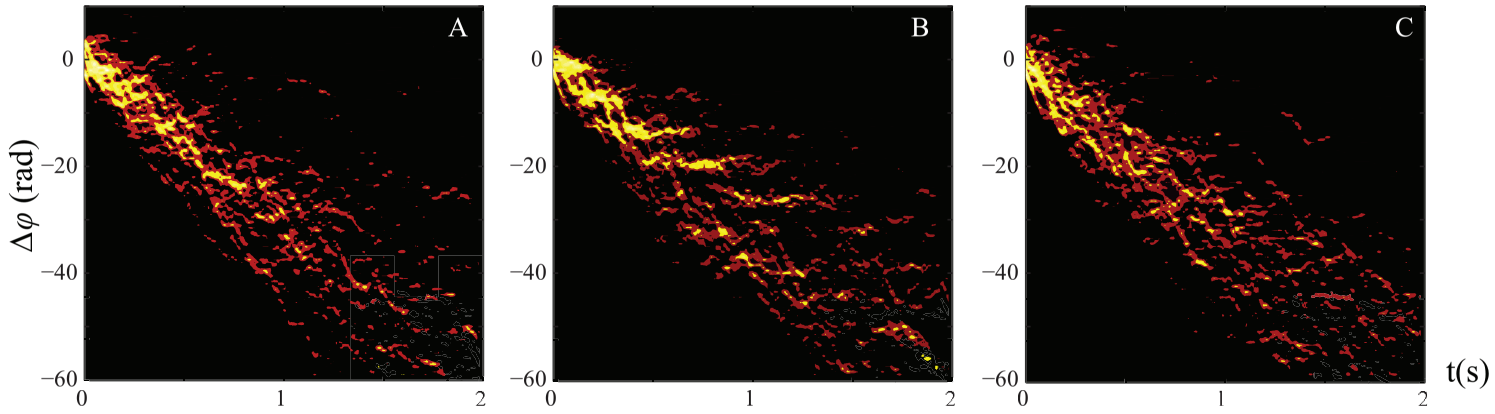

Figure 4.2: Time evolution of the histogram of the unwrapped $\Delta\phi(t)$.
(A), (C) The histogram of the unwrapped $\Delta\phi(t)$ without stimulus, before and after the stimulation, respectively. (B) The phase histogram during stimulation shows plateaus indicating phase-locking in the ensemble response. The color-coded scale indicates the height of the histogram in arbitrary units.

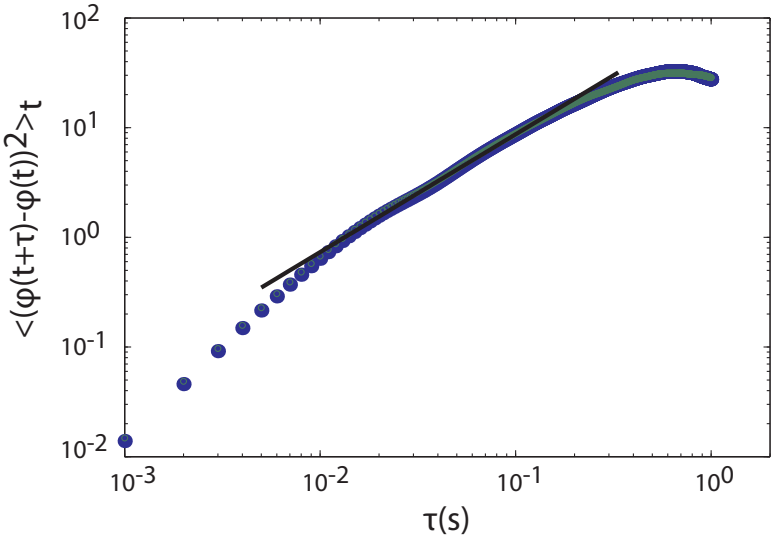

Figure 4.3: Phase diffusion of spontaneous oscillations in the absence of stimulation
The phase diffusion was calculated, following the procedure described in Data Analysis, from data shown in Fig. 4.2A (blue circles), and Fig. 4.2C (green squares). Each trace was obtained from an averaging over 50 presentations. The black line is the linear fit of slope one.

difference extracted with respect to a zero-amplitude signal. The phase histograms did not exhibit plateaus but rather showed a broadening of the distribution that was consistent with phase diffusion. The diffusion coefficients were extracted from Fig 4.3, as described in Data Analysis. Note that the phase became super-diffusive for small τ due to a low-pass filter, applied to the raw traces to enable extraction of the phase. The diffusion coefficients were 51.6 s^{-1} and 48.8 s^{-1} for the oscillations before and after stimulation, respectively.

4.3.2 Occurrence of phase slips

We next explored phase-locking dynamics in the individual traces. Fig. 4.4 displays $\Delta\phi(t)$ of one hair bundle as a function of time, extracted from a single trace of motion over the course of the applied stimulus. The sequence of panels corresponds to records taken at increasing f_0. At very small stimuli (Fig. 4.4A), below

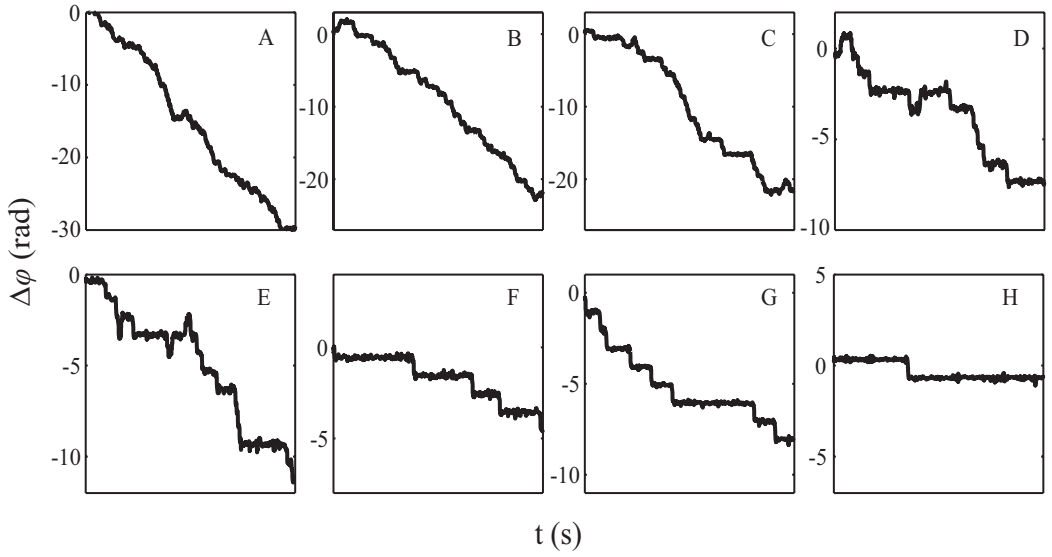

Figure 4.4: Time evolution of $\Delta\phi(t)$ at different stimulus amplitudes. From (A) to (H), the stimulus amplitudes (f_0) are 0.2, 0.35, 0.5, 0.6, 0.7, 0.8, 1.0, and 1.2 pN, respectively. The stimulus frequency is fixed at 10 Hz, with $\omega_0 \sim 14$ Hz. Phase-locking intervals can be observed for f_0 above ∼0.5 pN (C) and extend in duration as the stimulus amplitude increases.

∼5 nm (∼ 0.3 pN), the time trace of $\Delta\phi(t)$ drifted linearly with time, consistent with a biased random walk. By subtracting the drift due to nonzero $\Delta\omega$, a phase diffusion coefficient was extracted, yielded 107.2 s^{-1}.

As the stimulus amplitude was increased (Fig. 4.4B), plateaus began to appear in $\Delta\phi(t)$, becoming more pronounced with increasing stimulus (Fig. 4.4C). At drive amplitudes above ∼5 - 10 nm (∼0.3 - 0.6 pN), the time-dependent traces displayed intervals of phase locking, interspersed with phase slips (Fig. 4.4D - 4.4H). Increased levels of stimulus led to increased durations of the plateaus in $\Delta\phi(t)$, and the reduction in the rate of phase slip production. The direction of the average phase slip was determined by the sign of the detuning ($\omega - \omega_0$).

To extract the characteristics of bundle motion during a phase slip, defined as a change of 2π that occurs on a time scale shorter than the period of the imposed drive, we performed an average over multiple phase slips in individual traces. The detected events were aligned so that the centers of motion coincide (see Fig. 4.5).

Figure 4.6A displayed three examples of phase slips, obtained from averages taken over 51, 36, and 31 events, respectively. The top and middle of Fig. 4.6 illustrate the bundle motion during a phase slip with positive detuning, where the skip in the oscillation occurred from the positive or negative phase of the active motion. Negative detuning resulted in an additional oscillation during the phase slip (Fig. 4.6A, bottom).

There existed a correlation between phase slip production and nonlinearity in the amplitude response. We extracted $|\tilde{X}(\omega)|$ from the same hair bundle as shown in Fig. 4.4, as well as time traces of $\Delta\phi(t)$. In the low stimulus regime, where $|\tilde{X}(\omega)|$ increased linearly with f_0 (Fig. 4.6B, blue dots), diffusive behavior was observed in $\Delta\phi(t)$ (Fig. 4.6B, inset B). At f_0 corresponding to the compressive regime (black dots), $\Delta\phi(t)$ exhibited the staircase structure indicative of phase slips (Fig. 4.6B, inset A). Finally, high drive amplitudes suppressed the phase slips and perfectly entrain the motion (Fig. 4.6B, inset C). In this regime, the amplitude of the phase-locked response was proportional to f_0 (Fig. 4.6B, green dots).

4.3.3 Predictions from stochastic Adler equation

In a prior publication, we showed that the main features of the experimentally observed Arnold Tongue could be reproduced by the normal form equation for the Hopf bifurcation [24]. Fig. 4.6B constitutes a slice through the response space, taken at a fixed frequency. The figure illustrates that the nonlinear growth of $|\tilde{X}(\omega)|$ correlated with the occurrence of phase slips in its $\Delta\phi(t)$. Throughout the regime of weak stimulation ($\sim$0.1 - 10 pN), the amplitude of spontaneous oscillation remained constant. Hence, we proposed that the relevant variable to describe the dynamics of bundle motion in response to weak signals is the phase degree of freedom. We showed that the stimulus amplitude dependence of the phase-locked amplitude ($|\tilde{X}(\omega)|$), the rate of phase slips (ν_{ps}), and the effective

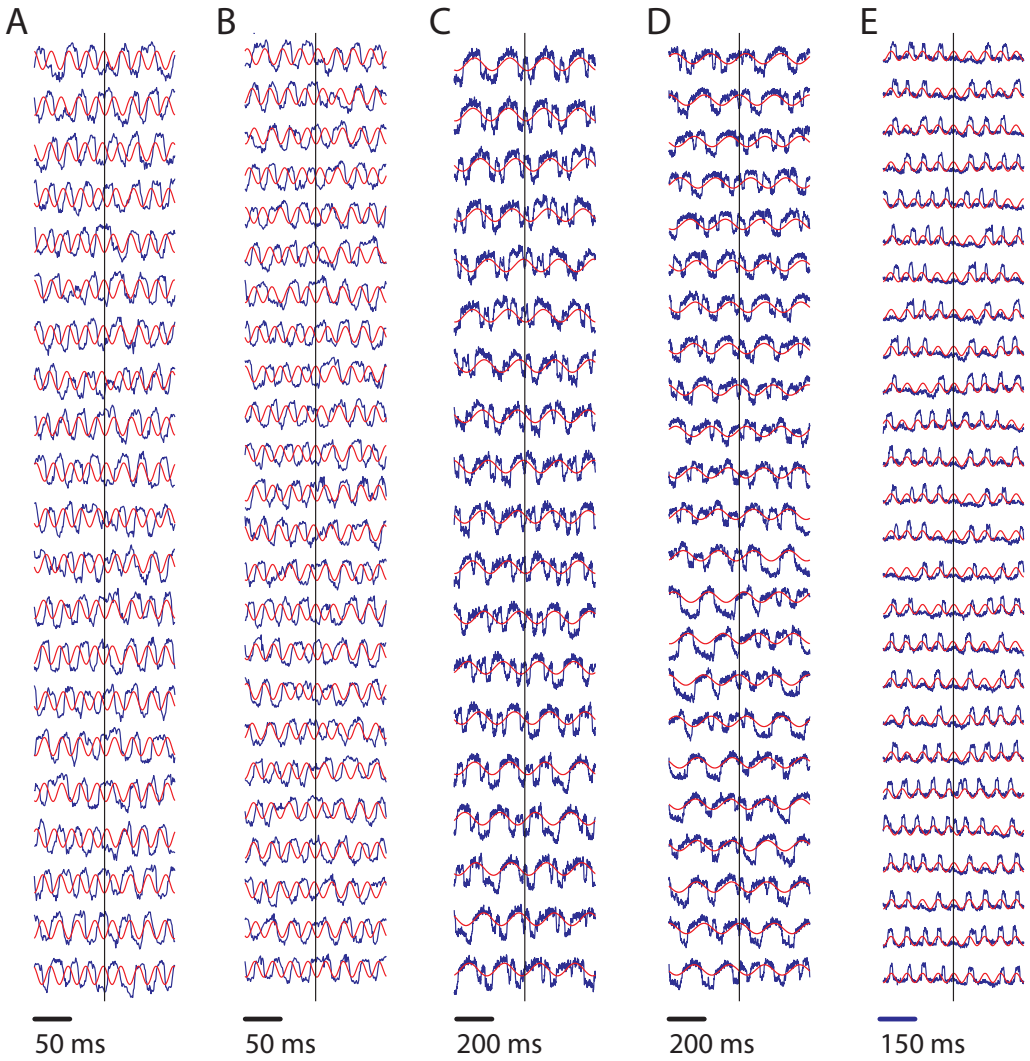

Figure 4.5: Examples of bundle motion during individual phase slips
The averaged motion of (A) and (B) is shown in Fig. 4.6A (top), (C) and (D) is shown in Fig. 4.6A (middle), and (E) is shown in Fig. 4.6A (bottom).

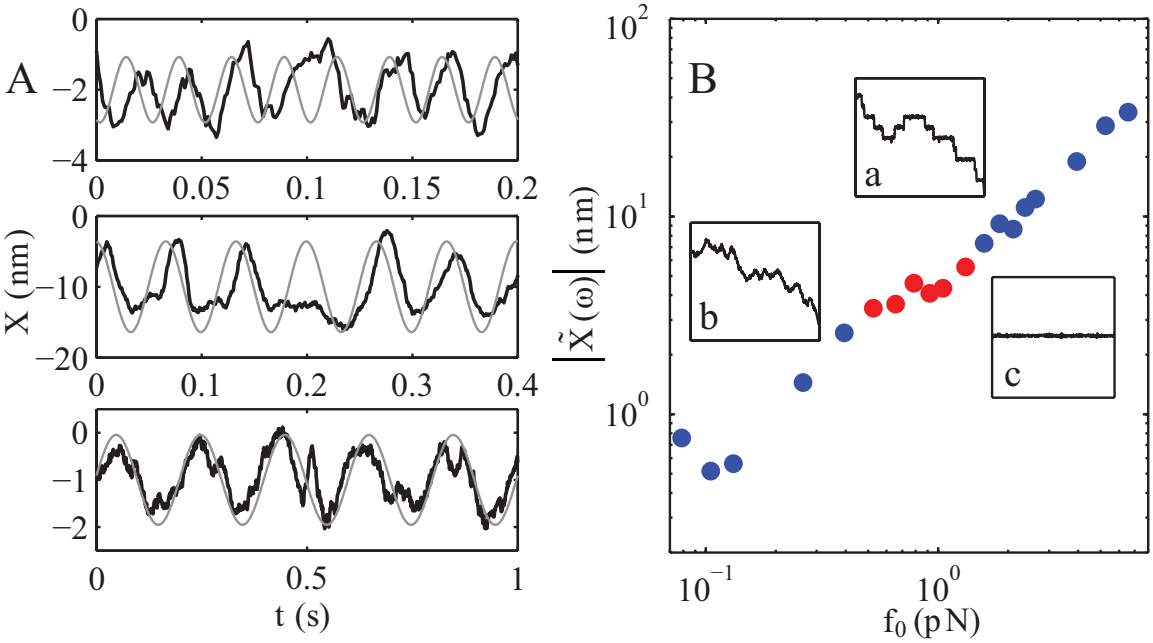

Figure 4.6: Correlations between phase slips, bundle motion, and phase-locked amplitude

(A) Characteristic dynamics of hair bundle motion during a phase slip. The superimposed gray lines indicate the averaged stimulus during the phase slip. Top, Middle: Phase slip associated with positive detuning ($\omega = 40$ Hz, $\omega_0 = 30$ Hz, and $\omega = 15$ Hz, $\omega_0 = 10$ Hz, respectively). Bottom: A phase slip associated with negative detuning ($\omega = 5$ Hz, $\omega_0 = 6.5$ Hz). (B) Correlation between the appearance of phase slips and the compressive nonlinearity. Red dots indicate the stimulus amplitudes at which the phase slips occur. Blue dots indicate the linear regimes.

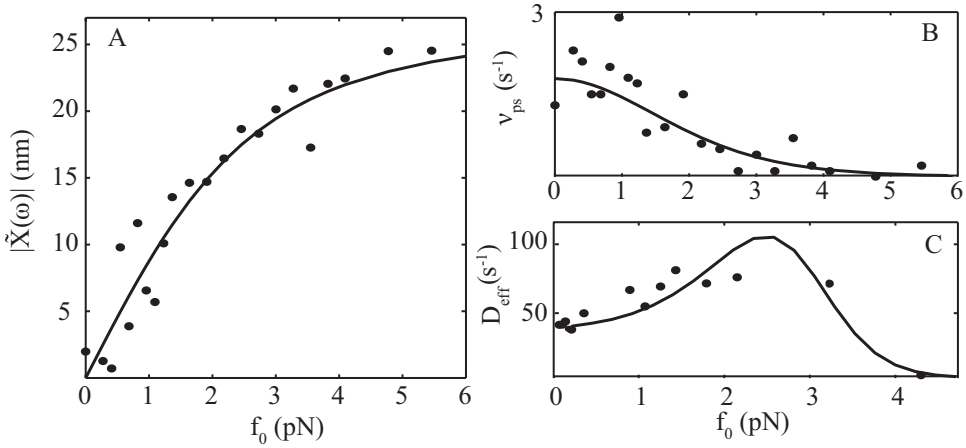

Figure 4.7: Comparison with the Adler equation.
Analytic solutions (solid lines) are superposed on experimental data (dots). (A) Phase-locked amplitude as a function of f_0 ($\omega = 5$ Hz, $\omega_0 = 4.5$ Hz). The measured $r = 28$ nm. The proportionality constant $\epsilon/T = 0.66 f_0$, is obtained from the fit. (B) Rate of phase slip production as a function of f_0. The fit of the analytic solution is plotted with the same fitting parameter as in (A), with $\Delta\omega = 4.7$ rad/s. (C) D_{eff} predicted by Eq. 4.5 and extracted from the data. The proportionality constant $\epsilon/T = 0.63 f_0$ and $D_0 = 40\ s^{-1}$ are obtained from the fit, with $\Delta\omega$ fixed at the measured value of 60 rad/s.

diffusion coefficient (D_{eff}) can be well captured by the stochastic Adler equation (Eq. 4.5).

In Fig. 4.7, we compared our measurements with predictions based on Eq. 4.5. Fig. 4.7A displays $|\tilde{X}(\omega)|$, with the analytical prediction at zero detuning superposed, $|\tilde{X}(\omega)| = r(I_1(\epsilon/T))/(I_0(\epsilon/T))$ [84, 2]. The bundle was stimulated with low $\Delta\omega$ (4.7 rad/s), for 10 s. Only the low (diffusive) and intermediate (phase-slipping) regimes are shown. Since the coupling strength (ϵ) was linearly dependent on f_0, the proportionality constant between ϵ/T_{eff} and f_0 was the only fitting parameter. The oscillation amplitude was estimated to be 28 nm obtained from fitting the histogram of the bundle position with a double-Gaussian distribution. The fit in Fig. 4.7A yielded $\epsilon/T_{eff} = 0.66 f_0$.

Fig. 4.7B displays the frequency of phase slip production (ν_{ps}), as a function of f_0, from the same recordings as in Fig. 4.7A. In the limit of small $\Delta\omega$, the rate

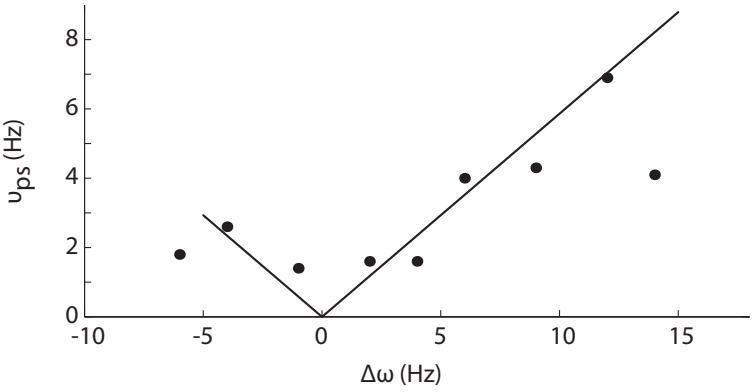

Figure 4.8: Frequency dependence of phase slip production.
The stimulus amplitude is 10 nm, corresponding to the $f_0 = 1.4$ pN. The fitting parameter is $\epsilon/T_{eff} = 1.07 f_0$. Linear dependence is observed

for thermally activated phase slips is $\nu_{ps} = \frac{\Delta\omega}{2\pi}[I_0(\frac{\epsilon}{T})]^{-2}$. The relation between ϵ/T_{eff} and f_0 was used as extracted from Fig. 4.7A.

We also examined the dependence of the rate of phase slip production on $\Delta\omega$, at a fixed f_0. The experimental result showed a linear dependence which is consistent with the theoretical prediction as shown in Fig. 4.8. The stimulus amplitude was kept constant at 10 nm. The fitting parameter was $\epsilon/T_{eff} = 1.07 f_0$.

For the stimulus amplitude that did not induce entrainment, the phase of the bundle oscillation exhibited diffusive behavior, as shown in Fig. 4.3. When the stimulus amplitude reached ∼10 nm, phase slips occurred, and the overall behavior of the phase became non-diffusive. However, by subtracting a slow drift due to any preference in the direction of phase slips, the effective diffusion coefficient (D_{eff}) can be extracted from Eq. 4.11 as well. For higher stimulus amplitudes, during which phase slips rarely occurred, the effective diffusion coefficient was poorly defined (Fig. 4.9).

Fig. 4.7C compares the measured D_{eff}, from the same hair bundle as the top of Fig. 4.6A, with the theoretical prediction. The fitting parameters yielded $\epsilon/T_{eff} = 0.63 f_0$ and $D_0 = 40 s^{-1}$, with $\Delta\omega$ fixed at 60 rad/s.

To further test the validity of the stochastic Adler equation, we independently

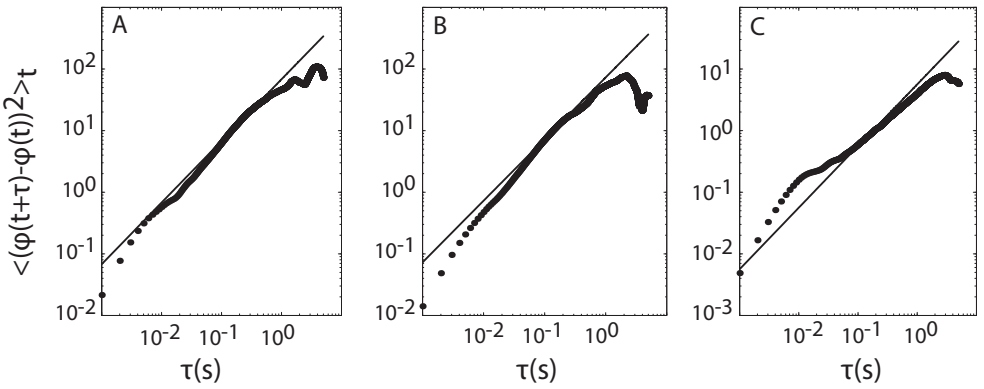

Figure 4.9: Phase diffusion under different stimulus amplitudes.
Data obtained from results shown in Fig. 4.7C. (A) At 4 nm (0.86 pN) stimulus, the phase is diffusive with $D_{eff} = 34\ s^{-1}$. (B) At 15 nm (3.225 pN) stimulus, $D_{eff} = 36.4\ s^{-1}$. The black solid lines indicate the linear fit of slope one. (C) At 20 nm (4.3 pN) stimulus, a phase slip occurs only once during the recording, and the linear regime is not apparent in the plot. The extracted D_{eff} is 2.8 s^{-1}. The black solid line is the linear fit of slope one.

extracted ϵ from the averaged Eq. 4.5, and T_{eff} from the autocorrelation function of $\Delta\phi(t)$ during phase locking. By averaging the Adler equation, we obtained a linear plot between $\langle \frac{d}{dt}\Delta\phi \rangle$ and $\langle f_0 \sin \Delta\phi \rangle$ with α and $\Delta\omega$ being the slope and the intercept, respectively, as shown in Fig. 4.10A. The coupling strength and the detuning extracted were $\epsilon = 5.6 f_0$ and $\Delta\omega = 4.83$ rads.

To estimate the effective temperature, the autocorrelation of the phase difference during the phase-locking regime was fitted with exponential decay of the form $C(t) = C_0 e^{-t/\tau_c}$ with $T = C_0/\tau_c$. The averaged autocorrelation function with exponential fit is shown in Fig. 4.10B. The effective temperature extracted was approximately 7.75. The ratio ϵ/T was then 0.7, consistent with the number obtained from the fits in Fig. 4.10B ($\epsilon/T = 0.66$).

4.3.4 Long-term effects of entrainment

Apart from contraction of phase space observed during weak mechanical stimulation, some hair bundles also exhibited more regular spontaneous oscillations

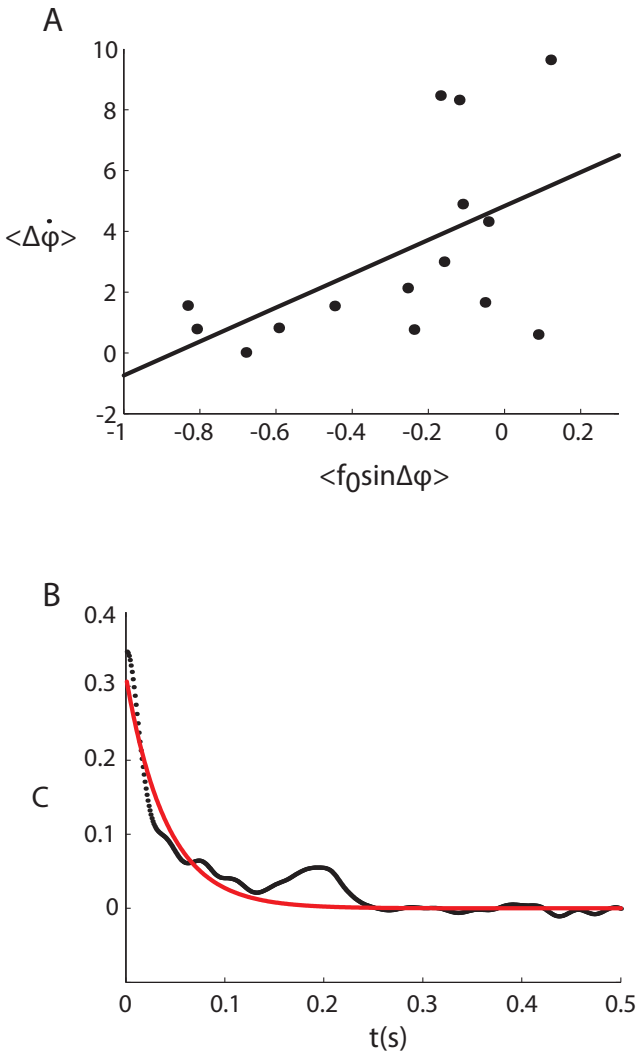

Figure 4.10: Estimates of ϵ and T_{eff}.
(A) The averaged phase velocity versus $\langle f_0 \sin(\Delta\phi)\rangle$. Each point is obtained from recording with different stimulus amplitude. The proportionality constant of the coupling strength and the detuning are extracted from the slope and the intercept of the fit (black line), respectively. (B) Autocorrelation function of the phase during phase-lock intervals. The plot is averaged over 4 recordings with different stimulus amplitudes. The exponential fit (red line) is used to extract the effective temperature.

post-stimulation. Fig. 4.11A illustrates the autocorrelation function of hair bundle oscillation obtained before, and after stimulation of 2.5 nm amplitude, at 20 Hz, slightly lower that the characteristic frequency of the bundle. 40 bursts of 2-second stimuli were applied, with ∼1.5 seconds pauses. Autocorrelation function was calculated from 0.5-second long recordings before and after each burst of stimulation, then averaged over 40 presentations. As readily seen from Fig. 4.11A, bundle oscillation became more correlated after the stimulation, resulting in a slower decay in the autocorrelation function.

In some experiments, hair bundles was stimulated for $\sim$ 5 - 7 minutes. Interestingly, phase-locking behavior of some bundles was enhanced over the course of the experiment. This improvement was not apparent in individual traces, but in the ensemble average. We applied 45 presentations of identical stimulus, as in Fig. 4.1, and calculated averaged traces. Each averaged trace was obtained from averaging increasing number of presentations (from 1 to 45) in chronological order, and reversed. Fig 4.11B plots the longest phase-locking period, i.e., the longest duration between two successive phase slips, of averaged traces. As the number of recordings used in the averaging increased, the duration extended, until reaching the whole duration of stimulation, indicating complete phase-locking, when the first 42, or the last 34 presentations were used in averaging. Fig. 4.11C shows the time at the onset of the longest period of phase-locking. Similar to Fig. 4.11B, the onset of the longest phase-locking coincided with the onset of stimulation when the first 42 , or the last 34 presentations were used in the averaging. Both analyses suggested that the hair bundle was more easily entrained after ∼1 - 2 minutes of stimulation.

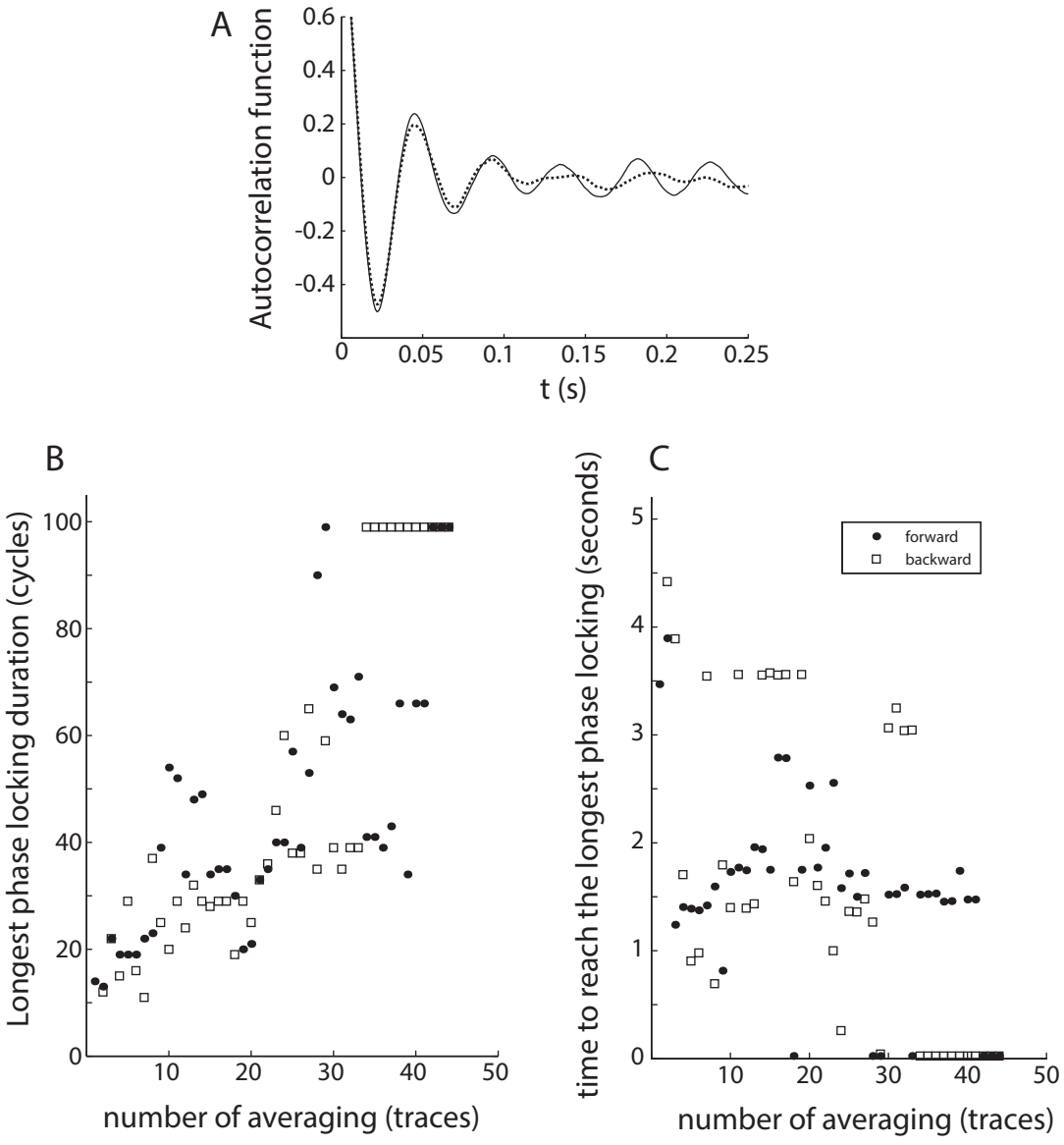

Figure 4.11: Long-term effects of entrainment.
(A) Autocorrelation function obtained from 0.5-second recordings before (dashed line), and after (solid line) stimulation of 2.5 nm at 20 Hz. (B) Longest duration of phase-locking obtained from traces of different averaging, in chronological order of the experiment (open squares), and reversed (filled circles). (C) Time at the onset of the longest phase-locking, obtained from traces of different averaging, as in (B).

4.4 Conclusion

Prior theoretical studies described the dynamics of the auditory system by proximity to a supercritical Hopf bifurcation [11, 22], shown to capture the amplification and frequency selectivity observed in the cochlea. Here, we examine the response of spontaneously oscillating hair bundles under *in vitro* conditions, indicating that the system is not in the immediate vicinity of a supercritical Hopf bifurcation. We find that the dynamics at low stimulus amplitudes are well described by the stochastic Adler equation, which displays a transition between the spontaneous and mode-locked oscillation. The transition occurs via a SNIC [81] and is characterized by a regime in which the phase difference $\Delta\phi(t)$ between the oscillator and the stimulus displays phase slips. The staircase structure observed in the phase difference is one of the classic signatures of mode locking in a system described in prior literature by a tilted washboard potential [84].

While the occurrence of spontaneous oscillation under *in vivo* conditions remains unknown, the existence of spontaneous otoacoustic emissions indicates that such an instability can arise. In the presence of spontaneous oscillation, weak signals lead to a contraction in the distribution of the instantaneous phase of hair bundles. We observe that, at slightly higher amplitudes of stimulation, contraction in the distribution of phase does not proceed in a uniform fashion, but rather leads to the appearance of phase-locked plateaus in the response. Mode-locked intervals are interrupted by sudden phase slips of 2π, leading to the staircase structure characteristic of this class of nonlinear systems [84]. Hence, even at amplitudes of applied force that are too small to evoke complete entrainment, intermittent intervals of phase locking occur in the active oscillation of individual bundles. We propose that the phase degree of freedom dominates the hair bundle response in this regime, and is well described by the stochastic Adler equation.

Entrainment of active motility by weak signals, with the bundles poised in

the regime of intermittent mode locking, could provide a sensitive mechanism of detection. Crossing of the SNIC bifurcation, however, does not lead to frequency selectivity of the response. The sacculus, a vestibular and auditory organ specializing in low frequencies, is known to have convergent patterns of enervation, with each neuron connected to an ensemble of hair cells. Phase locking of an ensemble of oscillatory hair bundles constitutes a potential mechanism of detection in biological systems that display high sensitivity and broad frequency tuning.

CHAPTER 5

Phase-Locking Behavior of Single Hair Bundles Under Mechanical Offsets

Part of the results in this chapter appeared in the publication "Phase-locked spiking and stochastic resonance of hair cells" submitted to Interface Focus. The authors are Roie Shlomovitz, Yuttana Roongthumskul, Robijn Bruinsma, and Dolores, Bozovic.

5.1 Introduction

Under appropriate conditions, hair bundles of certain species can exhibit spontaneous limit cycle oscillations [58, 17], one of the signatures of an underlying active amplifier. When hair bundles are deflected by sound waves, tip links connecting the individual stereocilia are placed under tension, leading to the opening of mechanically sensitive ion channels. Gating of the transduction channels in the stereocilia leads to bi-stability in the position of the bundle. An adaptation process, mediated by an array of myosin motors physically connected to the transduction complex, continuously adjusts the position of the bundle. Significant noise is evident in this innate motility, with variation in the local frequency and phase of the oscillation. External signals of much smaller amplitude have been shown to entrain the spontaneous motion [59].

Theories based on nonlinear dynamics have been proposed to describe active hair bundle motility [24, 75, 57]. Higher order nonlinearities have been shown to

lead to rich bifurcation diagrams in the phase space. Dependent on the internal parameters, the auditory system could be poised near a number of different bifurcations, which determine the characteristics of its phase-locking to the applied stimulus. The theoretical models describe the nonlinear response observed experimentally, and predict the amplification of low-amplitude stimuli. In a recent study, we showed that at low amplitudes of an imposed sinusoidal drive, phase-locking of spontaneously oscillating bundles occurs via a saddle-node bifurcation, characterized by the occurrence of phase slips, sudden excursions of 2π, at a rate that is dependent on the amplitude and detuning of the applied drive, as described in chapter 4. We measured the occurrence of phase slips in the response of the hair bundle and showed that the dynamics of the observed behavior were consistent with the stochastic Adler equation [64].

Under natural conditions, hair bundles of the bullfrog sacculus are coupled to an overlying otolithic membrane [48, 5]. Hair bundles were shown not to exhibit spontaneous oscillations when connected to the otolithic membrane, indicating that loading can tune them across the bifurcation. Our observations indicated that attachment to the membrane may impose an offset on the position of the bundle with respect to its freestanding state [25, 48]. We therefore examined the effects of mechanical deflection on the dynamic state of the bundle, and found the active oscillation to be suppressed by the application of an offset, with the transition displaying either frequency or amplitude modulation or an admixture of the two [25].

In this chapter, we explore the dynamic response of hair bundles under large mechanical offsets, until suppression of spontaneous oscillation is achieved. To capture the regime where the system is quiescent, but still poised in the vicinity of the bifurcation, we apply gradual ramps or sequential steps to the positions of the hair bundles. We observe the occurrence of 'spikes'–sudden and rapid excursions of the hair bundle–under a range of imposed deflections. These spikes

are stochastic, but are readily phase-locked by an imposed sinusoidal stimulus. We demonstrate that this spiking regime leads to a significant amplification of the signal and explore its mechanisms with a numerical simulation.

5.2 Materials and Methods

5.2.1 Mechanical stimulus

Mechanical stimuli were applied to a hair bundle at the base of a glass fiber, as described in chapter 2. Probes were coated with concanavalin-A, then attached only to the kinociliary bulb, which provided better adhesion, possibly due to larger surface area. In this chapter, two types of mechanical offsets were applied to the base of the glass fiber: steady-state and slowly increasing deflections, both away and toward the kinocilia. However, to imitate the natural deflections imposed on hair bundles under the otolithic membrane, most data analysis were done on data obtained from positive deflections.

In some experiments, sinusoidal stimuli with different amplitudes and frequencies were applied, simultaneously with a large static offset, on the bundle. A constant offset was applied as a square wave, with the bundle returning to the original position upon the cessation of each sinusoidal stimulus train, to avoid the effects of long-term adaptation. The order of stimuli presented was also randomized to avoid any consistent cumulative effects of adaptation.

5.2.2 Data analysis

5.2.2.1 Spike detection procedure

In the recordings where slowly increasing offsets were applied to the bundle, slow drifts in the bundle motion were removed from the data, so the channel-opening state fluctuates around zero. The traces were divided into 1-second long sections.

The histogram of the bundle position of each section was calculated, and peaks of the histograms corresponding to the channel opening position were fit with a quadratic polynomial. This value was subtracted from the raw trace, defining zero position to be that of the channel-opening state. The ramp-subtraction procedure is shown in Fig. 5.1.

A spike detection procedure was applied to the ramp-subtracted traces. A Gaussian distribution was fit to the histogram of the bundle position around the channel-opening state to determine the standard deviation of the distribution (Fig. 5.2). To ensure that the detected spikes are well above the noise level, a threshold was chosen to be 4 times this standard deviation. Any excursion of the bundle beyond the threshold was defined to be a spike. This threshold was fixed for all of the applied bundle offsets.

If sinusoidal stimuli were applied, the passive response of the bundle was removed prior to applying spike detection software. The passive response was determined by fitting a sine wave at the stimulus frequency to the bundle motion, ignoring any displacements larger than 10 nm in the negative direction.

Once spikes were detected, their amplitudes were defined as the absolute minima of the excursions. The spike duration was defined as the interval between the two adjacent threshold-crossings, thus slightly underestimating the full spike duration. Spike phase was defined as the phase of the stimulus cycle at the instant when the bundle motion crosses the threshold away from channel-opening state.

5.2.2.2 Calculation of work and power

Active work was calculated according to [59]. The drag force was calculated based on the bundle velocity, while the force delivered by the stimulus fiber is due to the relative motion between the base of the probe and the tip of the hair bundle.

$$F_d = -\xi \frac{dx}{dt}$$

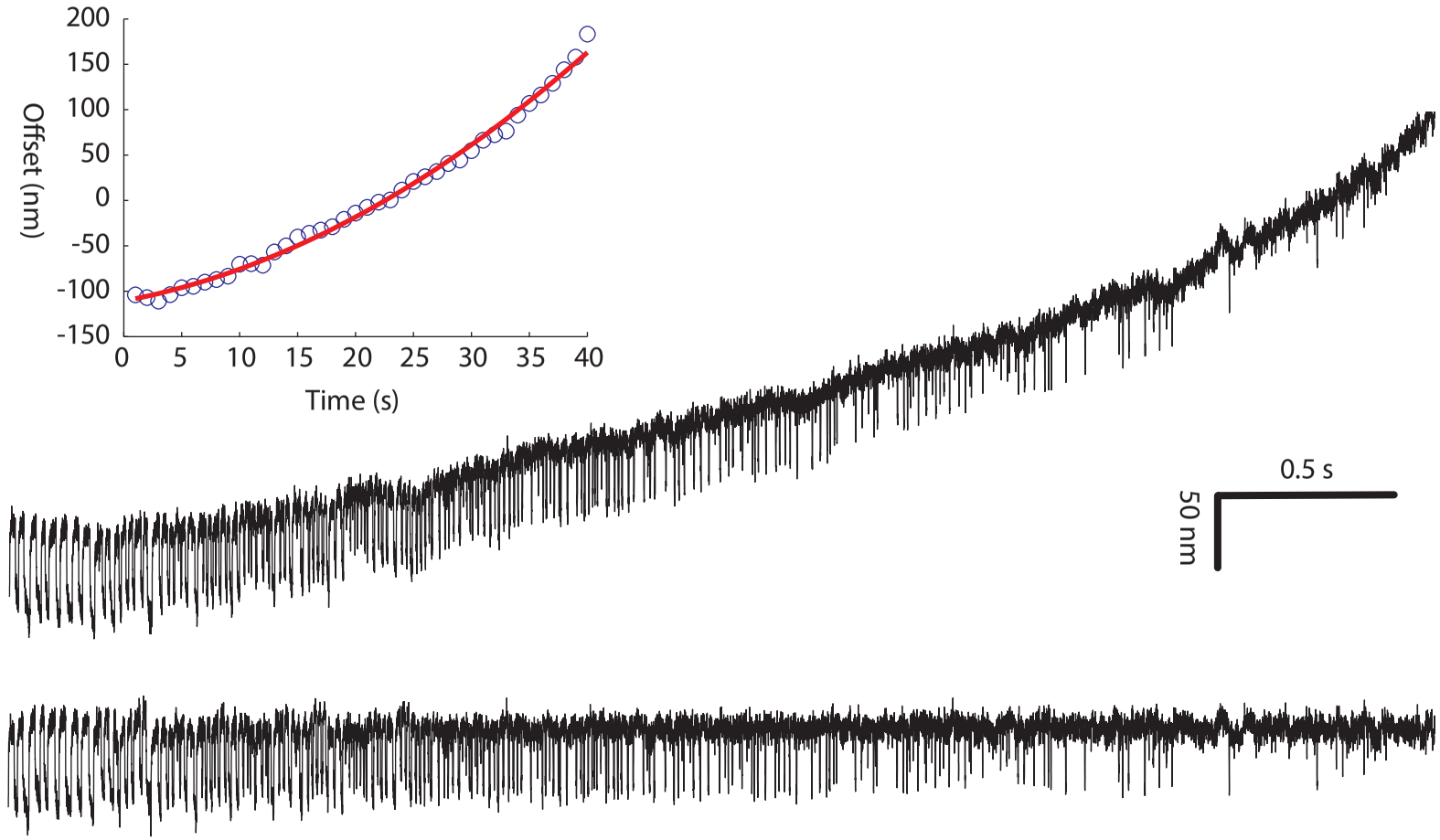

Figure 5.1: Ramp subtraction procedure

Spontaneous oscillation profile under positive ramp offset (top trace). The offset as a function of time was extracted from the peak of the histogram of the bundle position calculated from each 1-second long section, then fitted with a quadratic polynomial. This fit was subtracted from the recording to obtain the ramp-subtracted trace, shown in the bottom trace.

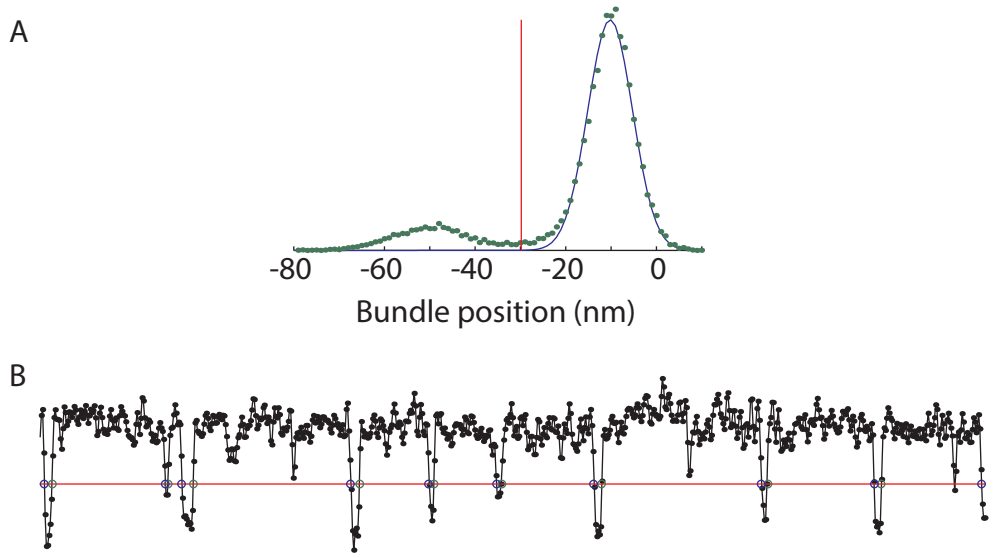

Figure 5.2: Spike detection procedure
(A) Histogram of the bundle position after ramp subtraction. Blue line shows the Gaussian fit around the channel opening state. Spike detection threshold is indicated by the vertical red line corresponding to 4 times standard deviation from the Gaussian fit. (B) Ramp-subtracted trace with spike detection threshold (red line). Any excursion exceeding the threshold is considered as a spike.

$$P_d = -\xi(\tfrac{dx}{dt})^2$$
$$F_{sf} = k_{sf}(\Delta - X(t))$$
$$P_{sf} = k_{sf}(\Delta - X(t))\tfrac{dx}{dt}$$

where ξ represents the combined drag coefficient of a hair bundle, and the stimulus fiber. The value for a hair bundle is taken from [18] (127 nNs/m). The stiffness k_{sf}, and ξ of the fiber are obtained from the calibration explained in chapter 2 ($k_{sf} \sim 150$ μN/m, $xi \sim$ 200-300 nNs/m).

The active power was defined as the difference between the dissipated power performed by the bundle in overcoming the drag force and the power delivered by the stimulus fiber.

$$P_{ac} = \xi(\frac{dx}{dt})^2 - k_{sf}(\Delta - X(t))\frac{dx}{dt}. \tag{5.1}$$

This active power was then integrated over the course of a spike, or a stimulus cycle to obtain the active work.

5.3 Results

We studied the response of hair bundles under various degrees of steady-state deflection and subject to mechanical sinusoidal stimuli of different amplitudes and frequencies. The Bullfrog sacculus was placed in a two-compartment-chamber configuration with the apical and basal sides of the epithelium exposed to artificial endolymph and perilymph, respectively. A flexible glass fiber was used to apply a static or a slowly increasing force toward or away from the kinocilium, with a maximum force ∼200 pN, corresponding to a deflection of ∼0.5-1 μm at the top of the bundle. Hair bundles were found to exhibit spike-like motions under intermediate deflections.

5.3.1 Effects of mechanical offsets on hair bundle oscillations

Under *in vitro* conditions, decoupled hair bundles from the Bullfrog sacculus typically exhibit spontaneous oscillations, with comparable durations spent in the channel-opening and -closing states. To capture the behavior of hair bundle oscillations at different deflections, a ramp of linearly increasing offset was applied to the base of the glass fiber attached to the bundle. The ramp speed applied to the base of the probe was 22 nm/s, corresponding to force 3.3 pN/s applied to a stationary bundle, chosen to be slow with respect to the rate of adaptation [20].

As the bundle was gradually deflected toward the kinocilium (defined to be the positive direction), an increase in the oscillation frequency was observed, together with a decrease in the amplitude of oscillation. In a significant fraction of the hair bundles studied, under larger deflections, the oscillations became increasingly asymmetric, favoring the channel-opening state, and exhibiting only brief excursions in the negative direction, away from the kinocilium. Thus, the relative time interval spent in the channel-opening state increased under applied offset. In this study, the spiking regime is defined to be the regime in which the ratio

between the interval of channel-closing to those of channel-opening is less than 20%. The threshold for spike detection is illustrated with dotted lines in the lower panels, Fig 5.3A.

Analysis of spikes under positive deflection showed that these mechanical spikes demonstrated a gradual reduction in the amplitude (Fig. 5.3B) and a decrease in the duration (Fig. 5.3C). This reduction in amplitude was also observed in recordings at a higher frame rate (2000 fps), and thus was not due to under-sampling (Fig. 5.4). Spike duration can be as short as 10 ms, indicating that a spiking bundle has an inherent ability to undergo one-to-one phase locking up to 100 Hz. The occurrence of spikes was previously shown to be stochastic, as the interspike intervals followed a Poisson distribution [76]. The spike rate decreased with increasing offset (Fig. 5.3D), until the motion was eventually completely suppressed.

Calculation of work done by a bundle over the course of one spike suggests that spike occurrence requires an active mechanism. Active work was defined as the difference between the dissipated work performed by the bundle in overcoming the drag force and the work delivered by the stimulus fiber [59]. Positive active work indicated that the dissipated work exceeded the work performed on a bundle by the stimulus fiber. Total active work done by the bundle per spike (Fig. 5.3E) in the spontaneous spiking regime was $\sim$80 zJ, slightly below that of the total active work performed per cycle in the oscillatory regime ($\sim$100 zJ). Calculation of the active power delivered at any instant during a spontaneous spike (Fig. 5.3F) showed that over the course of the channel closing, the bundle generated active work of $\sim$110 zJ. Restoring force exerted by the elastic glass fiber assisted channel re-opening, hence the bundles performed a net negative work of $\sim$ -30 zJ.

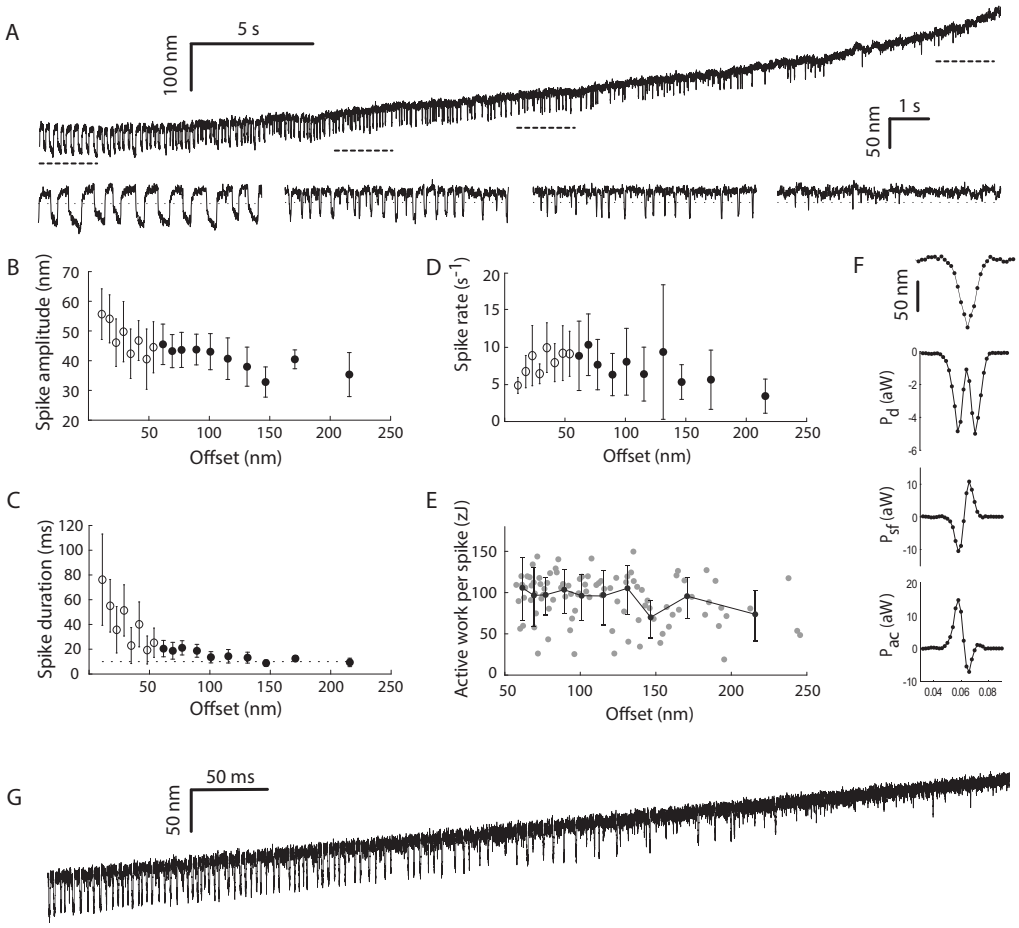

Figure 5.3: Characteristics of the spiking regime.
(A) Spontaneous oscillations of a hair bundle under a slowly increasing positive offset (22 nm/s). Lower panels are the zoom-ins of 4 different sections of the full trace, labeled by dashed lines. Dotted lines indicate the threshold used for spike detection, corresponding to 4 times the standard deviation obtained from a histogram of the bundle position. From (B) to (E), each point represents the averaged value obtained from 10 successive spikes. (B) Spike amplitude as a function of bundle offset in the oscillating (open circles) and spiking regime (filled circles). (C) Spike duration at different bundle offsets. The duration saturated at ∼10ms, corresponding to a frequency of 100 Hz. (D) Spike rate showed a peak at the end of the oscillating regime, and decreased in the spiking regime. (E) Active work produced by the bundle during each spike (gray dots). (F) Averaged behavior of bundle motion during a spike (top panel) and power from the viscous drag (P_d), power delivered from stimulus fiber (P_{sf}), and active power performed by the bundle (P_{ac}). (G) Numerical simulations of spontaneous oscillations of a hair bundle under a slow ramp offset (See Numerical Simulations).

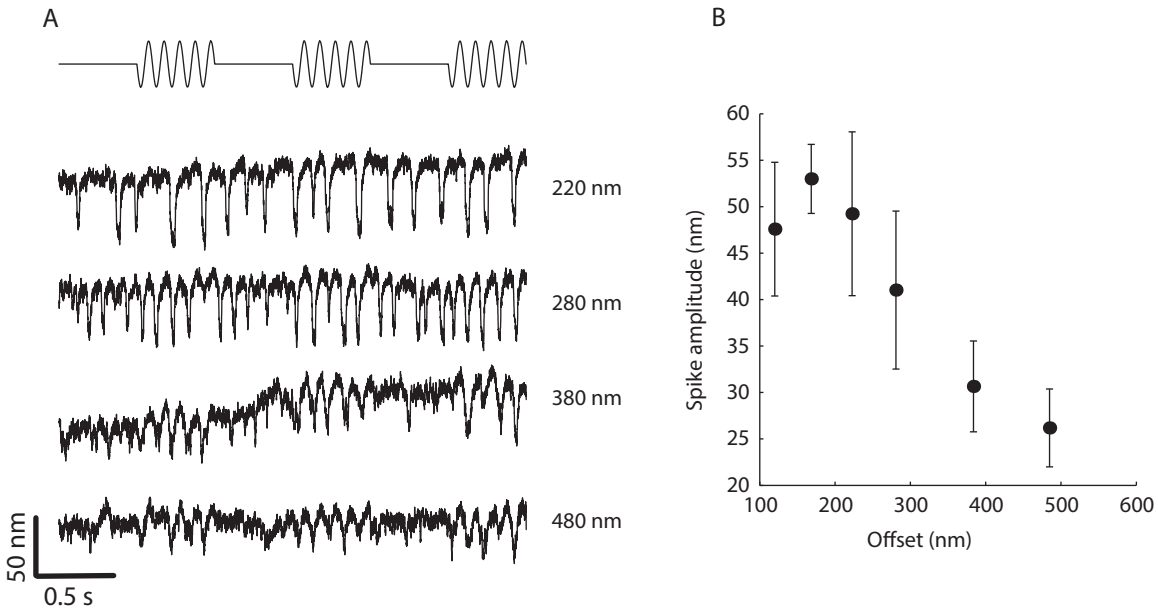

Figure 5.4: Spikes recorded at high frame rate.
(A) Hair bundle motion recorded at 2000 frames per second. Different steady-state offsets were applied to the bundle simultaneously with a burst of 20-nm sinusoidal stimulus at 10 Hz (top trace). (B) Averaged spike amplitude at different offsets. Spiking regime start at ∼200-nm offset.

5.3.2 Hair bundle response at different deflections

We next superposed sinusoidal stimuli onto the slow ramps. The stimulus frequency was chosen to match the characteristic frequency of the bundle oscillation at zero offset. In the spontaneously oscillating regime, the imposed signal entrained the innate motion (Fig 2A, *0 nm offset*), as shown in prior literature. The phase-locking behavior gradually transitioned from one-to-one mode-locking to higher-order mode-locking as the characteristic frequency of the oscillation increased due to larger deflections (Fig 2A, *100 nm offset*). This was clearly illustrated by the number of spikes per stimulus cycle reaching 2 at the end of the oscillating regime (Fig 2B).

As the bundles transitioned from the oscillatory to the spiking regime, they exhibited spikes superposed onto a passive response to the imposed sinusoidal stimulus (Fig. 5.5A). Larger mechanical offsets led to a decrease in the amplitudes

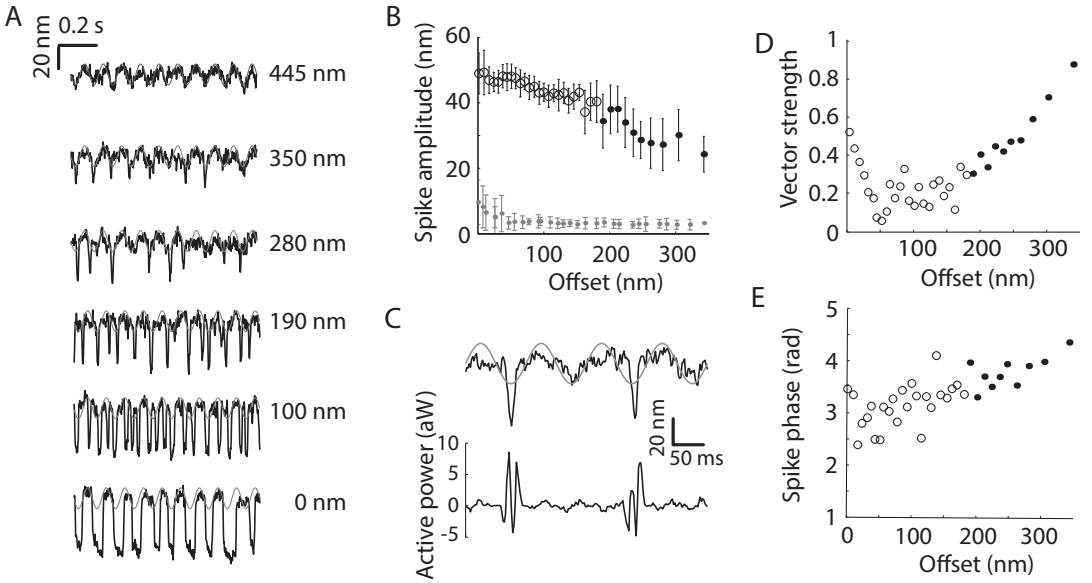

Figure 5.5: Phase-locking in the spiking regime.
(A) Hair bundle oscillation measured at different offsets, with an applied sinusoidal stimulus of 15 nm amplitude at 10 Hz (gray lines). From (B), (D), and (E), open circles indicate the oscillating regime, and filled circles indicate the spiking regime. Each point represents the average of values obtained from 10 successive spikes. (B) Spike amplitude (black dots) and passive response (gray dots). The passive response remained constant $\sim$3 nm. (C) Time-dependent active power generated by hair bundle, corresponding to the bundle motion in the top trace, with stimulus superposed (gray line). (D) Averaged spike phase drifted from π in the oscillating regime, to $\sim 1.5\pi$ rad in the spiking regime. (E) Vector strength showed a decrease in the oscillating regime, then rapidly increased as spikes occurred.

of the evoked spikes (Fig. 5.5B),while the passive response remained constant. For the particular experiment shown, spike amplitude was as large as 10 times that of the passive response. This characteristic response provides a potential mechanism for mechanical amplification by a hair bundle rendered quiescent by an imposed load. Calculation of work done by a bundle over the course of a stimulus cycle indicated that the hair bundle generated active work only during spikes, but not during passive response (Fig. 5.5C). This provides a potential mechanism for mechanical amplification by a hair bundle rendered quiescent by an imposed load.

Spikes showed an increased probability of occurrence at a preferential phase within the stimulus cycle. This was illustrated by a significant increase in the vector strength of the spike phase during the spiking regime (Fig. 5.5D). Upon further deflection, the occurrence of spikes became rare; however, a preferential phase was maintained and the vector strength continued to rise rapidly (Fig. 5.5D). The averaged spike phase fluctuated around π in the oscillatory regime (Fig. 5.5E), indicating 1-to-1 mode-locking; note that spikes are defined as excursions in the negative direction, hence the channel-closing coincided with the zero-crossing of the stimulus. The phase of the spikes slowly drifted to $3\pi/2$ in the spiking regime. This shift in the phase implied the possibility that spikes can be evoked by an external stimulus, with an increasing threshold at larger deflections.

Under negative deflections, similar response was observed, as shown in Fig. 5.6. In the spiking regime, spikes occurred as brief excursions in the channel-opening state. As the offset became more negative, unlike spikes under positive deflections, spike duration was not significantly affected by the offsets. Spike rate and spike amplitude, however, decreased as a function of offset.

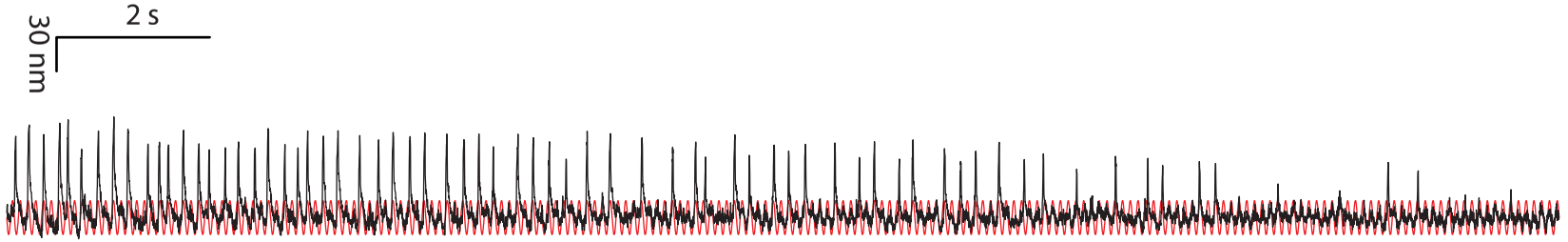

Figure 5.6: Mechanical response of hair bundle under negative offset.
A negative ramp was applied to the bundle, away from the kinocilium. A sinusoidal stimulus of 15 nm, at 10 Hz was superposed to the offset, shown in red.

5.3.3 Mechanical amplification

To test the hypothesis that spikes can be evoked by an external signal, we applied bursts of 10-Hz sinusoidal stimulus, with amplitudes of 5, 10, and 20 nm (corresponding to 0.75, 1.5, and 3 pN) applied to the base of the stimulus fiber, superposed onto slow ramps. As can be readily seen from the trace measured at 97-140 nm offset (Fig. 5.7A, lower trace), there was a regime where spikes could only be observed during the application of a stimulus. This clearly illustrated the ability of a quiescent hair bundle to respond to mechanical signals with an amplified movement.

The number of spikes per unit time did not show an overall increase with respect to the spontaneous rate, until stimuli of 20 nm amplitude or higher were imposed. A 10-nm stimulus only evoked an increase in the number of spikes in the regime of low spontaneous spiking rate (Fig. 5.7B, top panel), corresponding to the spiking regime near suppression. The vector strength of the spike phase, on the contrary, showed a significant improvement upon the application of even very weak signals (5 nm) (Fig. 5.7C). In contrast, comparable enhancement of phase-locking in the oscillatory regime required a higher stimulus amplitude (10 nm or higher). Hence, the spiking regime proved to be more sensitive to entrainment by mechanical stimuli.

5.3.4 Spikes at different stimulus amplitudes

To explore amplification by a hair bundle in the quiescent state, we applied a large static offset (100 pN) to the tip of the bundle in the positive direction. This offset was observed to suppress the active motility in most hair bundles. To avoid the effects of long-term adaptation, the offset was applied as a square wave, with the bundle returning to the original position upon the cessation of each sinusoidal stimulus train.

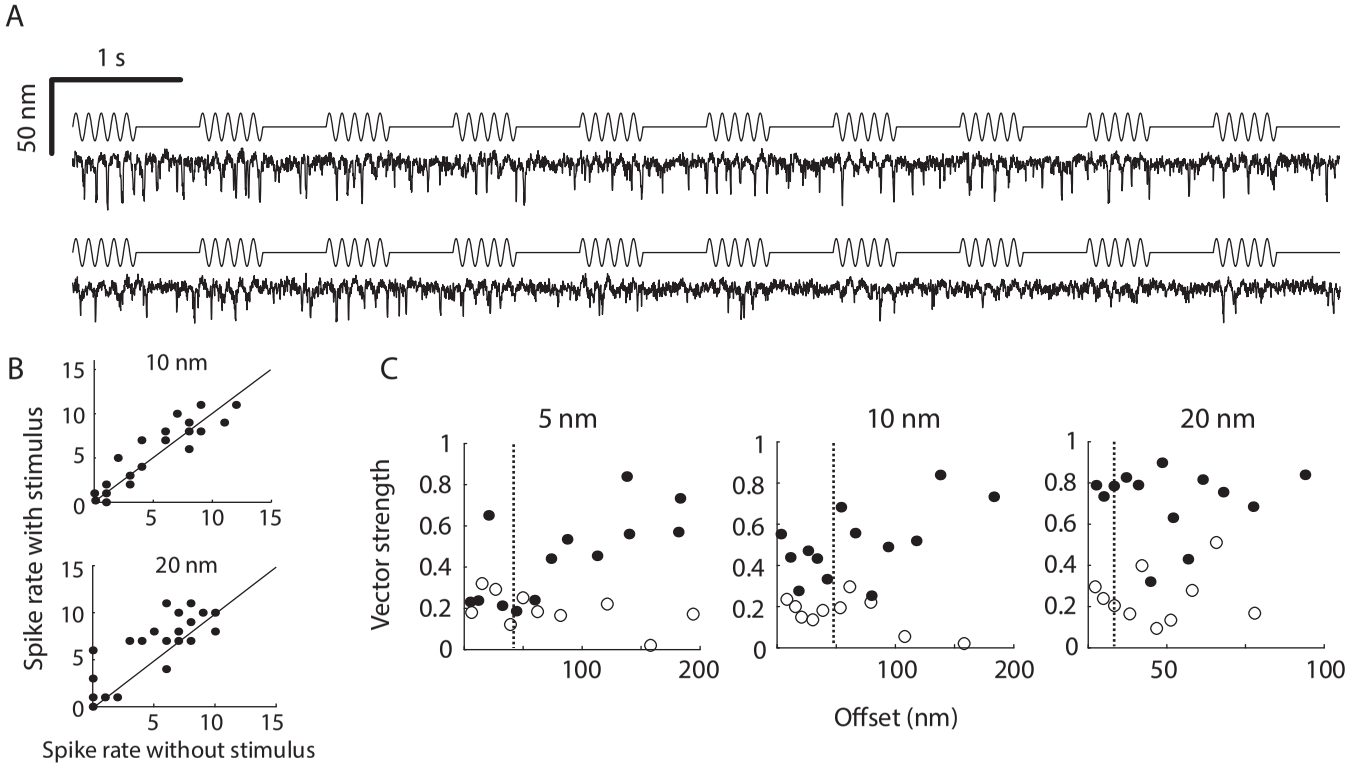

Figure 5.7: Effects of stimulus amplitude.
(A) Hair bundle oscillations with 20 nm stimulus. The offset in the top trace varied from 45-97 nm, and 97-140 nm in the lower trace. The drift due to the increasing offset had been subtracted. (B) Comparison of the number of spikes per stimulus cycle with versus without an imposed stimulus at 10 and 20 nm stimulus amplitudes. Data were obtained from the spiking regime only. 20-nm stimulus clearly increased the number of spikes at any offset. (C) Vector strength of spike phase with (filled circles) and without (open circles) stimulus at 5, 10, and 20 nm stimulus amplitudes. Dashed lines separates the oscillating and spiking regime.

We examined the effects of increasing amplitudes (3, 4, 8, 10, 12, 14, 16, 20, 30, 40, 50, 70, and 100 nm) on the bundle response (Fig. 5.8A). The order of stimuli presented was randomized to avoid any consistent cumulative effects of adaptation.

We decomposed the response of the bundle and measured separately the amplitude of the passive response and the amplitude of the superposed spikes. The threshold for spike detection was fixed for all applied stimulus amplitudes. We found that the spike amplitude remained largely constant, with a slight increase at very large stimuli, while the passive response increased linearly with the stimulus amplitude (Fig. 5.8B). The number of spikes per stimulus cycle gradually increased with signal amplitude, with the increase well described by a Boltzmann curve with thresholds between 60-100 nm, variant among cells. The vector strength, on the other hand, increased rapidly at small stimuli ($\sim$ 10-20 nm), and saturated to $\sim$ 0.9 at stimuli larger than 20 nm (Fig. 5.8C).

By observing the passive response and the spike amplitude separately, we can define an amplitude gain due to the spiking: ratio of spike amplitude to the passive movement. The amplitude gain was highest at small stimulus amplitudes, reaching a 100-fold increase, then dropped off with increasing stimuli (Fig. 5.9A). Calculation of active work generated per spike showed a significant reduction upon increasing stimulus amplitude, with zero crossing occurring at $\sim$ 40-80 nm (Fig. 5.9B), corresponding to $\sim$ 6-12 pN of force applied to the bundle. This indicated the range during which the hair bundle no longer amplified. Comparison with spike probability and gain showed that this range of amplification cutoff also corresponded to the amplitude gain $\sim$ 1-2, and spike probability $\sim$ 0.3-0.5, when spiking is a relatively rare event.

Not only did the spike amplitude remain largely constant over a wide range of stimulus amplitudes, it also did not show much variation with stimulus frequency, as shown in Fig. 5.10. The passive response exhibited a reduction at high stimulus

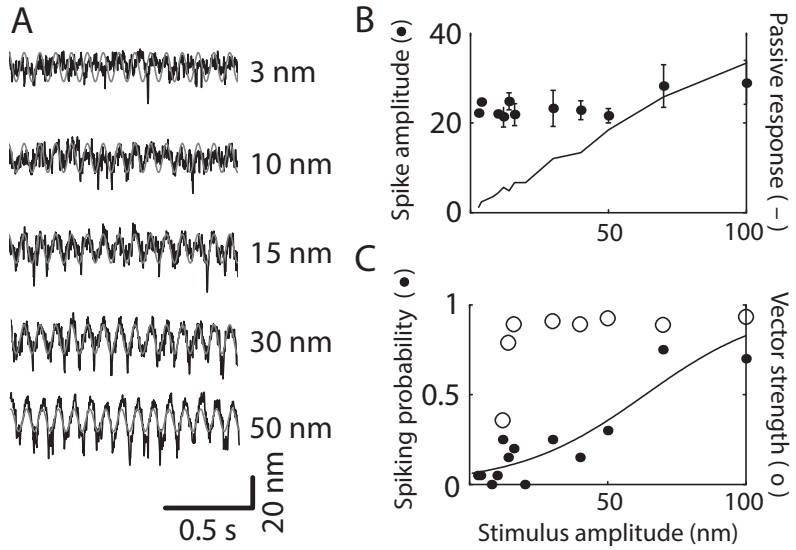

Figure 5.8: Mechanical amplification by a quiescent hair bundle at different signal amplitudes.
(A) Hair bundle motion in the quiescent state with different amplitudes of the imposed stimulus (3, 10, 15, 30, and 50 nm). (B) Spike amplitude (dots) and passive response (solid line) as a function of the stimulus amplitude. (B) Vector strength (open circles) and number of spikes per stimulus cycle (closed circles). Solid line is a Boltzmann fit to the number of spikes.

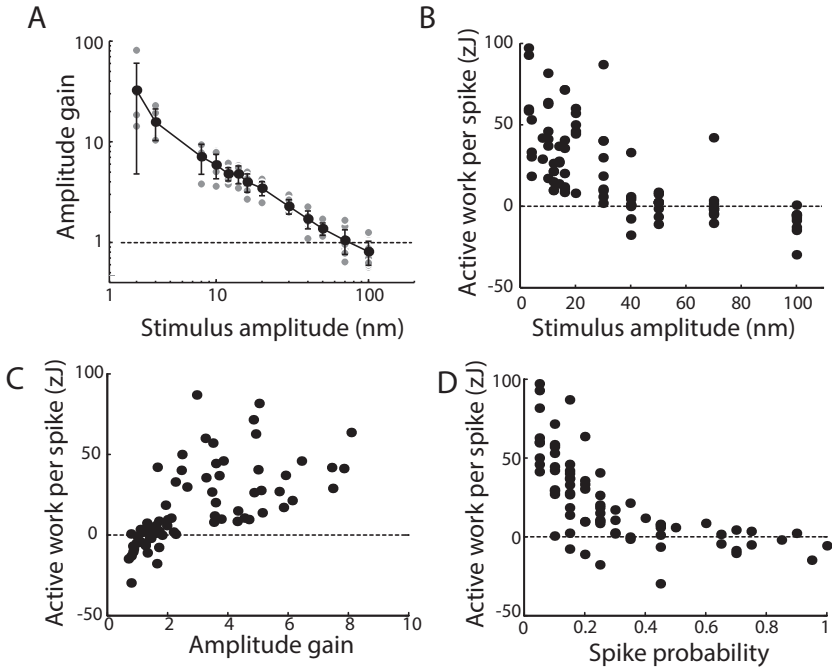

Figure 5.9: Mechanical amplification cutoff by quiescent hair bundles. (A) Gain at different stimulus amplitudes obtained from the ratio between spike amplitude and passive response from 12 bundles. Dashed line indicates unit gain. (B)-(D), dashed lines indicate zero active work. (B) Active work per spike evoked by the stimulus as a function of stimulus amplitude from 12 bundles. (C) Active work per spike as a function of amplitude gain. (D) Active work per spike as a function of spike probability.

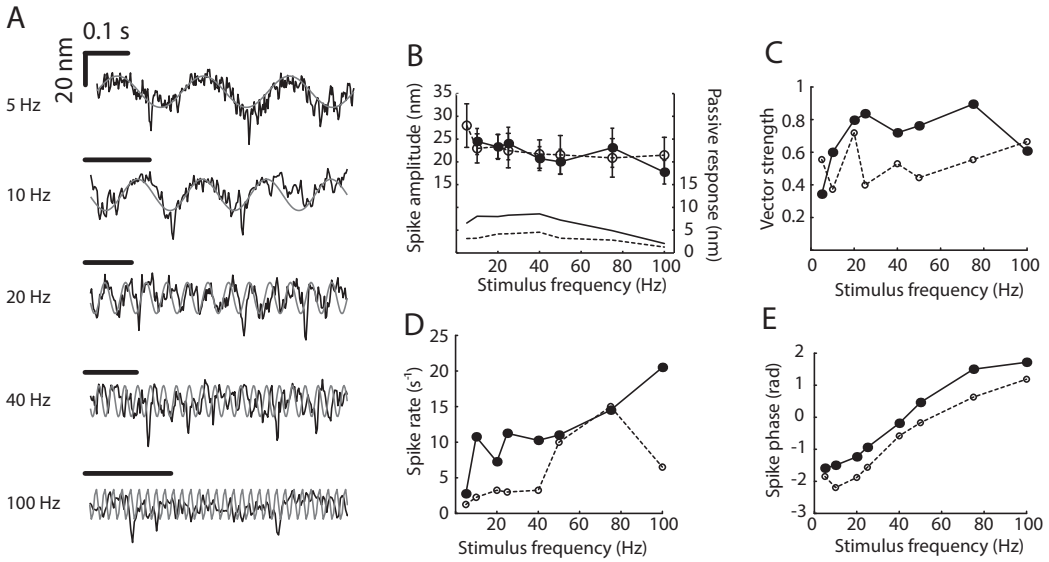

Figure 5.10: Mechanical amplification by a quiescent hair bundle at different signal frequencies.
(A) Hair bundle oscillations at different stimulus frequencies. The imposed stimuli are overlaid in gray lines. B-E: Responses were obtained from stimulus amplitude 10 nm (open circles, dashed lines), and 20 pN (filled circles, solid lines). (B) Spike amplitude and passive response at different stimulus frequencies. (C) Vector strength of the spike phase. (D) Spike rate. (E)Averaged spike phase.

frequencies possibly due to the low-pass filtering by the glass fiber. The vector strength of spike phase also fluctuated about a constant value over a wide range of stimulus frequencies (5-100 Hz).

We also observed similar effects of stimulus amplitudes and frequencies on hair bundles under large negative offset. As seen in Fig. 5.11, small stimulus amplitude evoked only passive response with small spiking probability, the number of spikes then increased as a function of signal amplitude. Spike amplitude seemed large unaffected by the stimulus, while the passive response increased with signal amplitude.

Fig 5.12 illustrates spike occurrence by different signal frequencies. Spikes were evoked on cycle-by-cycle basis up to ∼10 Hz. Higher stimulus frequencies evoked a spike, followed by a ∼0.2-0.5 s period of passive response. This passive period is reminiscent of the "refractory period" in action potential and was set by the

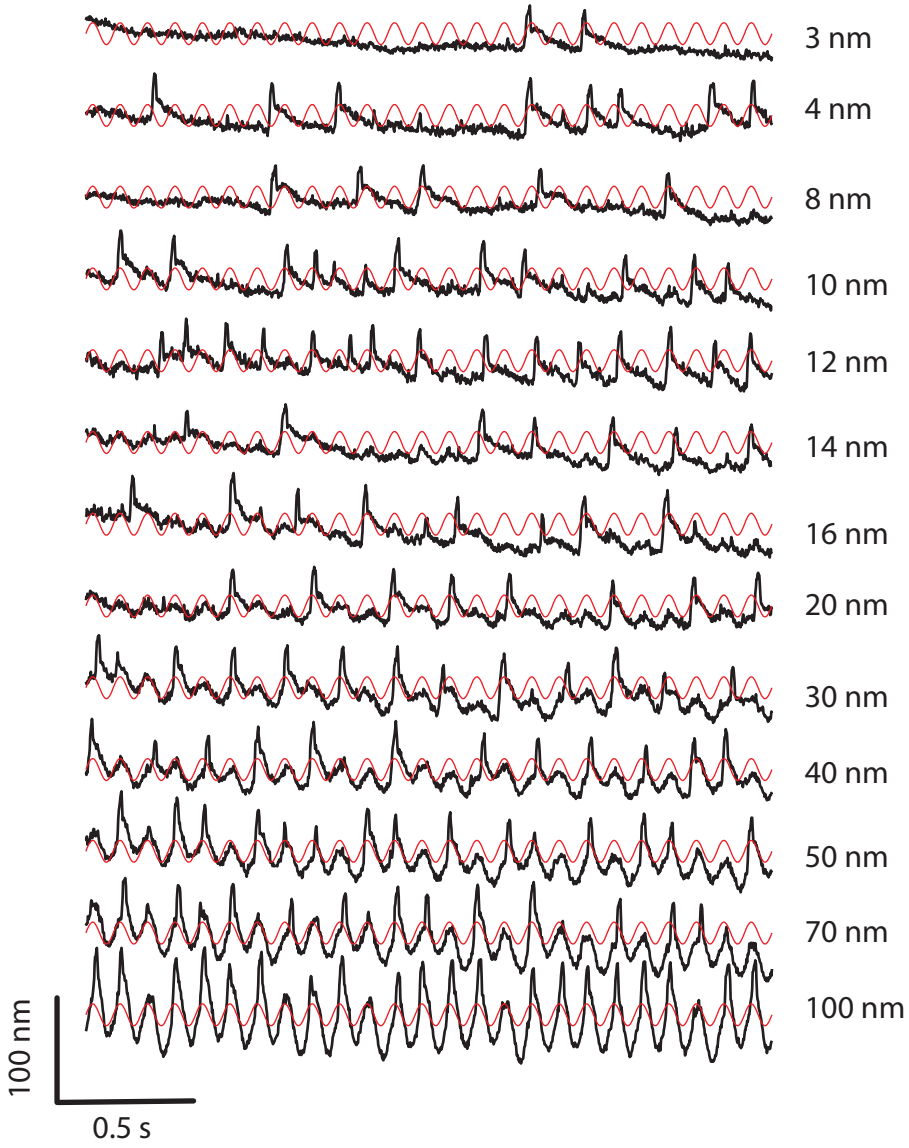

Figure 5.11: Mechanical amplification by a quiescent hair bundle at different signal amplitudes under negative offset.
Hair bundle motion under large negative offset, superposed by sinusoidal stimulus at 10 Hz, shown in red lines.

characteristic frequency of the hair bundle.

5.3.5 Numerical simulations

We performed a numerical simulation, based on the model described in Chapter 3, to explore the underlying mechanisms of bundle motility in the spiking regime. The model can reproduce the spiking regime (Fig. 5.3G), with the reduction in spike amplitude being captured with the existence of a variable gating spring –an internal spring with a calcium-dependent whose dynamics are slow with respect to those of myosin motors.

Based on the numerical model, the dynamics of a hair bundle can be described by using a double-well potential, corresponding to channel-opening and -closing state. Adaptation activity imposes an increasing tilt on the energy landscape, promoting channel opening or closing. This tilting of the double-well potential corresponds to the shift of the force-displacement curve along a sloped line [32].

At the onset of the spiking regime, at moderate deflections, the bundle resides in a shallow local minimum in the channel-opening state prior to a spike, even though the global minimum is the channel-closing state. A small perturbation due to noise or an external stimulus promotes the system to overcome the barrier and leads to the channel-closing excursion. Adaptation then plays a role to modify the energy landscape until the channel-closing state becomes unstable, leading to the re-opening of the channels (Fig. 5.13A). The double-well potential configuration is gradually restored after $\sim$10-20 ms.

As the bundle is further deflected into the spiking regime and away from the oscillatory regime, the channel-opening state gains its stability, until it becomes the global minimum (Fig. 5.13B). Noise and external stimulus can excite the system across the energy barrier causing channel closing. Channel re-opening then occurs spontaneously; the effects of adaptation process are minimal or absent, particu-

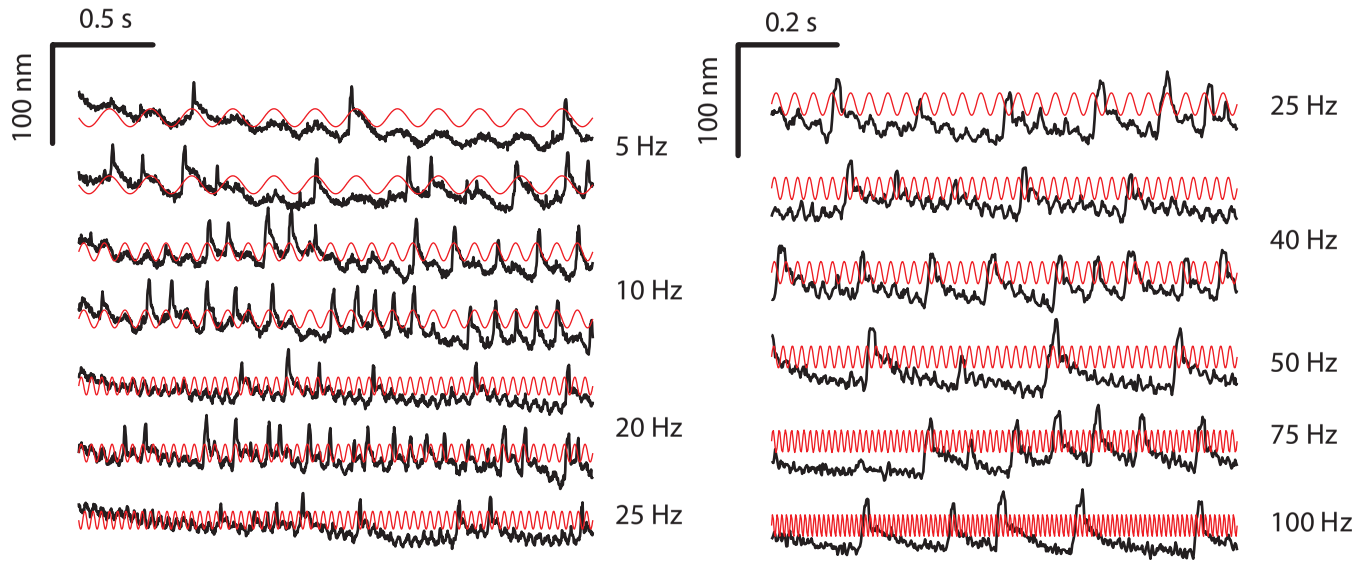

Figure 5.12: Mechanical amplification by a quiescent hair bundle at different signal frequencies under negative offset. Hair bundle motion under large negative offset, superposed by sinusoidal stimulus at 20 nm, shown in red lines.

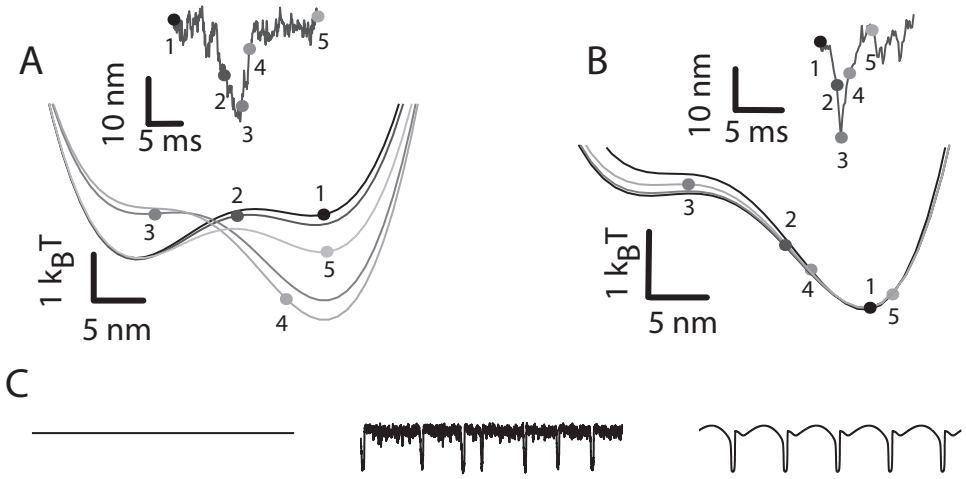

Figure 5.13: Numerical simulations of bundle dynamics during a spike. (A) Energy landscapes corresponding to different states of a bundle during a spontaneous spike at moderate deflections indicated in the inset. Adaptation plays a crucial role in modifying stability of the system. (B) Energy landscapes at different states of a bundle during a noise-induced spontaneous spike indicated in the inset. Effects of adaptation process was minimal, and the channel-reopening occurred due to the instability of the channel-closing state. (C) Numerical simulations of bundle motion in the absence of adaptation with a steady state deflection. *left* Bundle motion in the absence of noise. *middle* Bundle motion shows spikes with noise. *right* Spikes evoked by a 7 nm external stimulus at 5 Hz in the absence of noise.

larly when the channel-closing state is unstable at very large offsets. Numerical simulations with the adaptation rate set to zero also exhibited a spiking regime (Fig 5.13C) when a steady state deflection was applied to the bundle. Without thermal fluctuations from noise, the bundle remained quiescent. Noise and/or an applied stimulus could evoke spikes (middle and right panel, respectively). The active motility is completely suppressed once the energy barrier becomes too large ($\sim$2-3 k_BT, variant among cells).

5.3.6 Non-spiking Hair Bundles

Under slowly increasing positive offset, some fraction of hair bundles did not display a spiking regime, as shown in Fig. 5.14A. Instead, the oscillation remained

symmetric and the frequency increased, with a decrease in the amplitude until the oscillation vanished into the noise floor of the recording. According to the model, this would corresponded to small oscillations of hair bundle motion around a resting position at which the channel open probability is ~ 0.5, indicating a minimal energy barrier between the channel-closing, and -opening state. Mechanical response of these bundles at different offsets are shown in Fig. 5.14B.

Preliminary results indicated that the existence of the spiking regime did not correspond to the ramp speed. However, the spiking regime was often observed when the stimulus fiber used for deflection was far less stiff than the bundle. We calculated the skewness of the bundle motion near the suppression of the spontaneous activity. As seen in Fig. 5.15, large negative skewness, corresponding to the spiking regime, occurs at small stiffness ratio, defined as the ratio between the fiber stiffness to the combined stiffness of the bundle and that of the fiber. This finding is in agreement with the theoretical prediction based on the numerical model described in Chapter 2, in the absence of variable gating spring [57].

Based on morphology, hair cells from the bullfrog sacculus are previously shown to fall into two different subgroups. The first group consists of cylindrical cells, while the other one includes flask-shaped cell body, with smaller diameter [12, 13]. To verify whether the spiking behavior correlates with this classification, we plotted the skewness versus hair cells' diameter and bundle size. As shown in Fig. 5.16, no correlation was observed.

Results from numerical simulations showed that hair bundle motion near the suppression of the active motility can be modified by the variable gating spring: larger $k_{gs,1}$ (strong dependence of gaiting spring stiffness on calcium concentration) led to an absence of the spiking regime. Without variable gating spring, the spiking regime was always observed. This implied that calcium concentration played a central role in determining the bundle dynamics under positive offsets. In fact, numerical simulations suggested that applying a positive ramp to a hair

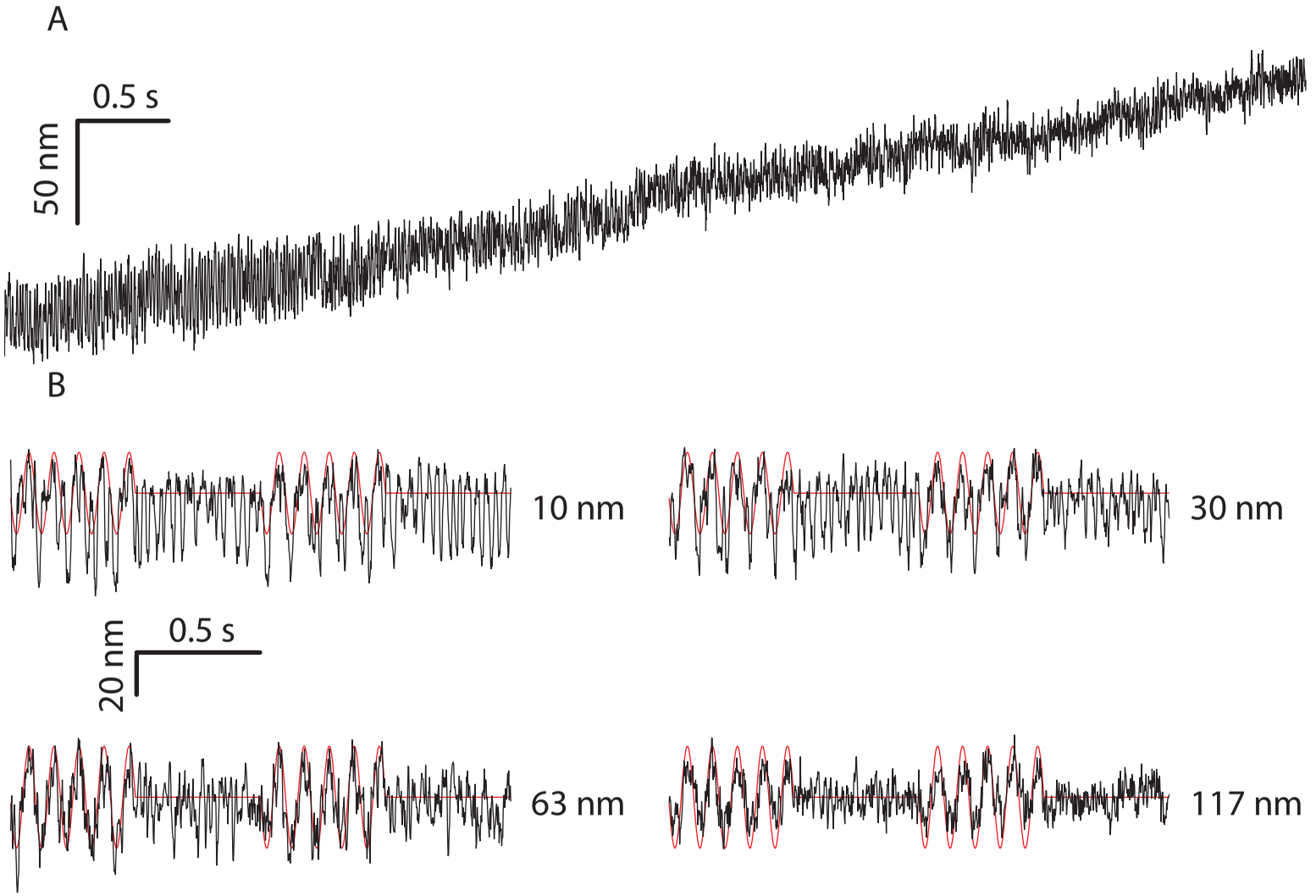

Figure 5.14: Non-spiking hair bundle.
(A) Spontaneous motion of a non-spiking hair bundle under a positive ramp. The oscillation remains symmetric and no spikes are observed until the supression of the active motility. (B) Mechanical response to bursts of 10-Hz stimulus at 20 nm amplitude. The stimulus is overlaid in red. The absolute offset of the hair bundle is shown next to each trace.

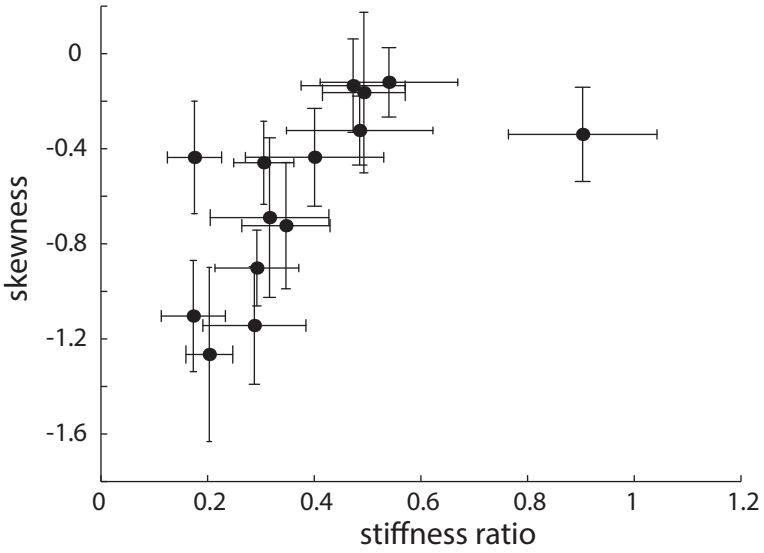

Figure 5.15: Effects of elastic loading
Skewness is calculated from bundle motion near the suppression of spontaneous motility, with large negative values corresponding to the spiking regime. The stiffness ratio is defined as the ratio between the fiber stiffness to the combined stiffness of the bundle and that of the fiber.

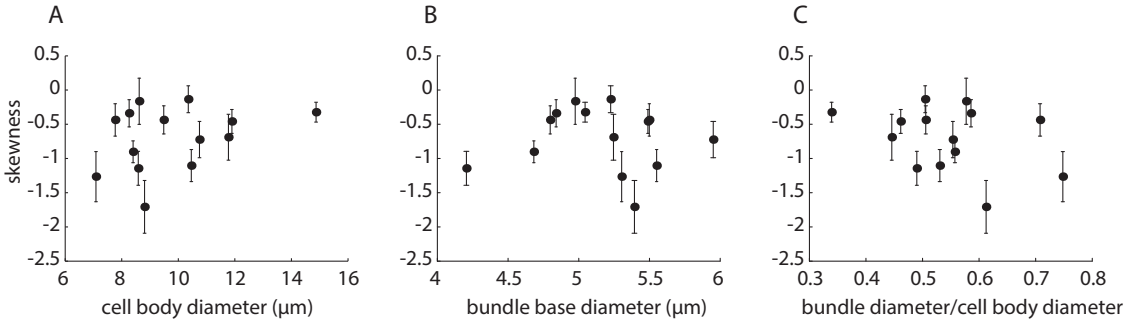

Figure 5.16: Correlation with cell body morphology
Skewness of bundle motion at different (A) cell body diameter, (B) diameter of the base of the bundle, and (C) the ratio between the bundle diameter to cell body diameter.

bundle in high calcium concentration abolished the spiking regime. We explored these effects experimentally and the preliminary results were consistent with the simulations, as shown in Fig. 5.17. Upon increasing calcium concentration, the range of offsets during which the bundle exhibit spontaneous activity became narrower, and the spiking regime disappeared.

5.4 Conclusion

A number of *in vivo* studies have demonstrated the presence of an amplification process in the inner ear, and yet its precise mechanism at a single-cell level remains unknown. In non-mammalian species, amplification of an applied signal has been demonstrated *in vitro* in spontaneously oscillating hair bundles [59]. This amplification occurred via the entrainment of a large-amplitude innate limit cycle oscillation by a smaller sinusoidal stimulus. The response exhibited a compressive nonlinearity, consistent with theoretical predictions, and weak frequency selectivity, consistent with the characteristics of the amphibian sacculus [60]. However, there are thus far no observations of spontaneous oscillations under *in vivo* conditions. Even *in vitro*, these oscillations are absent when the natural loading by the overlying otolithic membrane is maintained. Hence, a question that has remained open is how these cells might amplify a signal if their innate oscillations are suppressed.

The occurrence of spikes exhibited by hair bundles under mechanical offset constitutes a potential amplification mechanism for hair bundles that are poised in the quiescent regime. These sharp and sudden movements constitute a large excursion in the phase space, which corresponds to closure and re-opening of the transduction channels. This indicates that the system is in the excitable regime, where a minute signal can send it across the threshold and around a full limit cycle.

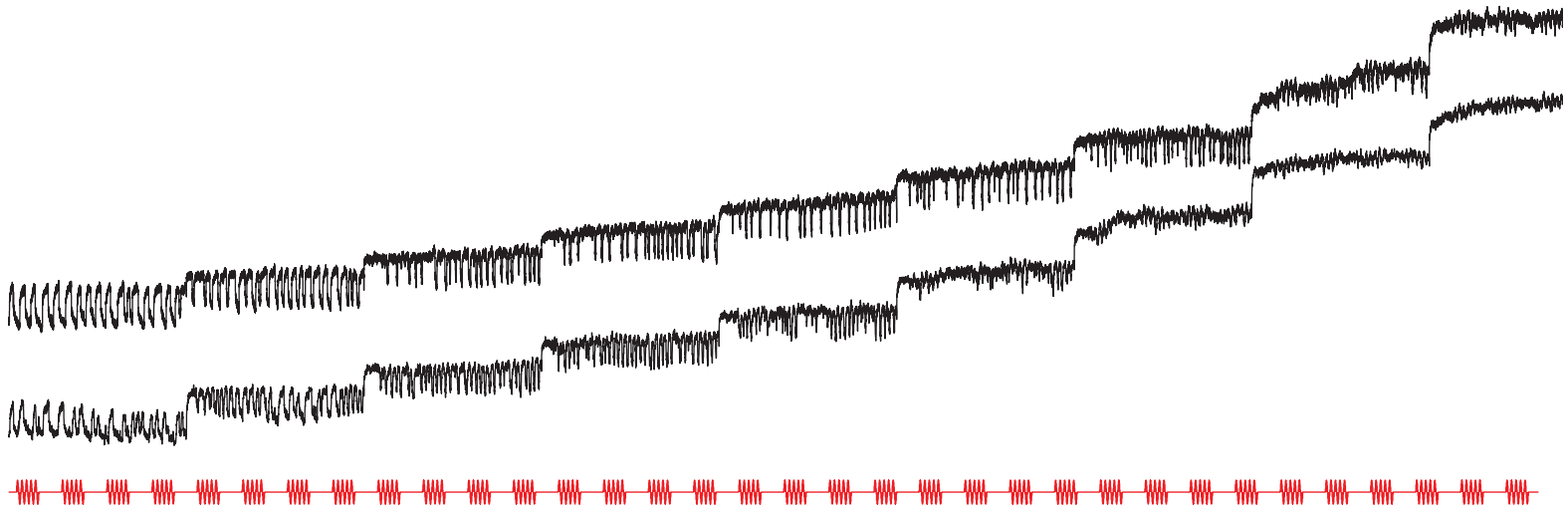

Figure 5.17: Effects of external calcium concentration
Experimental data of hair bundle motion under increasing step deflection, under regular- (top panel), and high- (bottom panel) calcium concentration endolymph. Bursts of sinusoidal stimulus was imposed onto the offset, shown in red line.

The characteristics of spiking behavior shown here are consistent with a theoretical study that modeled hair cell motion with a time-dependent Adler equation [76]. The Adler equation describes a system moving in a tilted washboard potential, and the addition of an offset term leads to a time-dependent modulation of the barriers. It was shown that such a model leads to the occurrence of spikes, which can be entrained by a weak signal. Our data confirm the existence of spikes, and show that this entrainment occurs at extremely weak signals, before any effects on spike amplitude or rate are observed.

The temporal profile of a spike indicates that the myosin motors would be too slow to exert much effect. As shown in our numerical model, the excursion of the motors over the duration of a spike was far smaller than would be observed in a limit-cycle spontaneous oscillation. The adaptation process hence plays a minimal role in the spiking regime near suppression of the spontaneous activity. The model indicates that the mechanism responsible for the excursion is the sudden closure and re-opening of the transduction channels.

One of the questions that remain open is why only a certain fraction of hair bundles exhibit a spiking regime under a slow ramp. A number of other species demonstrate the existence of two subpopulations of cells, one of which is responsible for amplification and the other for detection of signals. It is plausible that a comparable division exists to some extent in the amphibian system, with one set of cells showing the spiking regime and thus acting as non-frequency-selective amplifiers, whereas another group may serve as weakly tuned detectors. Such a division has however not yet been demonstrated and remains outside the scope of this work.

CHAPTER 6

Phase-Locking Behavior of Coupled Hair Bundles

6.1 Introduction

Under *in vitro* conditions, free-standing hair bundles from bullfrog sacculus display spontaneous oscillations, a manifestation of its active process. Amplification of external stimulus by single hair bundles have been previously studied, also described in Chapter 4, and 5. Prior literature demonstrated that this amplification occurred via the entrainment of a large-amplitude spontaneous oscillation by a smaller sinusoidal stimulus [59]. The amplitude of the phase-locked response exhibited a compressive nonlinearity, and weak frequency selectivity [60]. However, under a more natural condition, hair bundles are mutually coupled via the overlying structure, i.e., the otolithic membrane [48, 5]. Previous studies based on numerical simulations of hair bundle dynamics showed that mechanical coupling of a small number of hair bundles with small mismatch in their characteristic frequencies enhanced both frequency tuning and sensitivity of the system [19, 4]. This would benefit a system with tonotopic organization, such as the cochlear and the amphibian papilla, in which strong coupling occurs between neighboring hair bundles with similar characteristic frequencies. However, since frequencies of oscillating hair bundles from bullfrog sacculus are shown to be randomly distributed, how mechanical coupling enhances the sensitivity of the sacculus remains an open question.

Hair bundle dynamics have been previously described as a system poised near a Hopf bifurcation [11, 36, 24, 63]. Theoretical study of mechanically coupled Hopf oscillators suggests the existence of an "amplitude death" regime in which coupling suppresses the spontaneous motion of the oscillator [1]. The coupled system is also shown to exhibits a reduction in the noise level, rendering enhanced sensitivity. These predictions are similar to behaviors experimentally observed in the sacculus: the threshold of detection is lower than that of single hair bundles [52], and spontaneous oscillations do not occur under the otolithic membrane [25]. Therefore, in this chapter, we experimentally explore the effects of mechanically coupling two adjacent hair bundles on their mechanical response. Further, we test the prediction of noise reduction by extracting noise level from the phase of the coupled bundles oscillations, compared to those from single bundles. Frequency selectivity and sensitivity are also calculated from amplitude of the response. Finally, effects of mechanical offsets, similar to those described in Chapter 5, were studied.

6.2 Materials and Methods

Biological preparation and tracking of hair bundle motion are as described in Chapter 2.

6.2.1 Mechanical coupling of two adjacent hair bundles

Two adjacent hair bundles were mechanically coupled via a modified glass fiber. As described in Chapter 2, a glass fiber was placed in the proximity of the tip of the microforge. Thermal expansion causes bending of the glass fiber, resulting in an eyelash-shaped probe. This allowed us to simultaneously attach the top rows of stereocilia of two vertically adjacent hair bundles at the tips, while avoiding other bundles on the epithelium, as depicted in the schematic diagram in Fig.

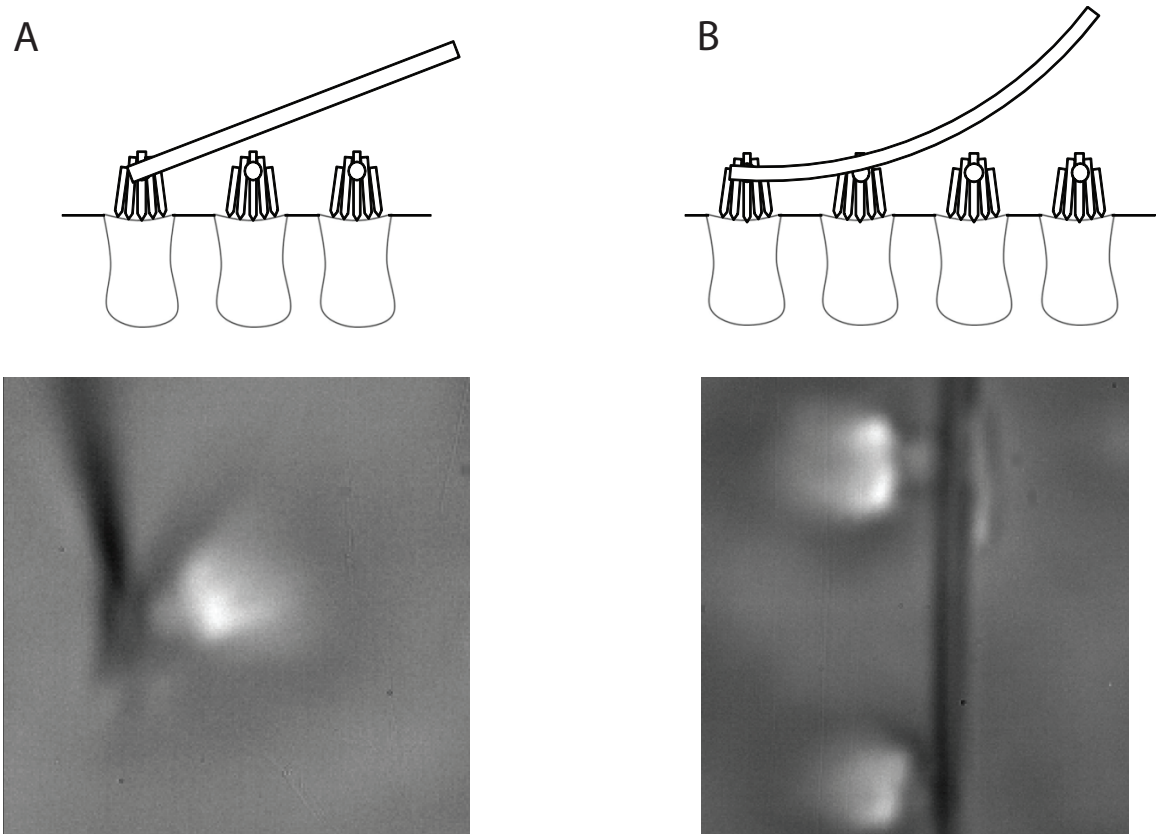

Figure 6.1: Probe attachment to two hair bundles
(A) Top panel shows schematic diagram of probe attachment to a single hair bundle. The probe is adjusted with an angle, to avoid attaching neighboring bundles. Lower panel shows a top-down optical image of a single bundle with a probe attached. (B) Top panel shows schematic diagram of mechanically coupled bundles. The modified probe allows both bundles to be attached at the tips, while avoiding other bundles.

6.1B. Stimuli were sent to the base of the fiber by a piezo actuator, as described earlier.

6.3 Results

In this chapter, we explored the effects of mechanical coupling of hair bundles on their spontaneous activity and mechanical response to sinusoidal stimuli. Using a modified probe allowed us to simultaneously couple and stimulate two adjacent

hair bundles. We found that synchronized motion of hair bundles was always observed. Characteristics of mechanical response of coupled systems were similar to those measured from single bundles.

6.3.1 Synchronization of spontaneous oscillations

Two vertically adjacent hair bundles were simultaneously attached to the same glass fiber, one to the tip, and the other closer to the base of the fiber, as illustrated in Fig. 6.1. Although the overall stiffnesses of the fibers used in this chapter were $\sim$ 100-200 μN/m, the coupling stiffness between hair bundles appears to be far higher, due to small separation between bundles ($\sim$ 20 μm). Calculation based on the bending rigidity of a rod yielded the coupling stiffness $\sim$ 25 mN/m [54]. This ensured perfect synchronization between hair bundles: with no degree of freedom observed. Fig. 6.2A demonstrates an example of hair bundles motion prior to, and with coupling. The motion of uncoupled hair bundles was uncorrelated; upon mechanical coupling, the correlation coefficient significantly improved (to $\sim$ 0.93 in this particular example).

Coupling of hair bundles with a large mismatch between their original characteristic frequencies (ω_0) also yielded synchronized motion, as shown in Fig. 6.2B. The motion of the coupled bundles was qualitatively similar to that of single bundles, with channel-opening, and -closing excursions followed by slow bundle displacement due to the adaptation process. However, significant variation in oscillation amplitude was observed, as shown in Fig. 6.2A. In some cases, an unusual oscillation profile was observed, as shown in Fig 6.2C, where small oscillations were superposed on a typical oscillation profile, both in the channel-opening and -closing state.

The characteristic frequency of the coupled system (ω) showed a linear dependence on the averaged ω_0, with significant scatter, shown in Fig. 6.3. This is

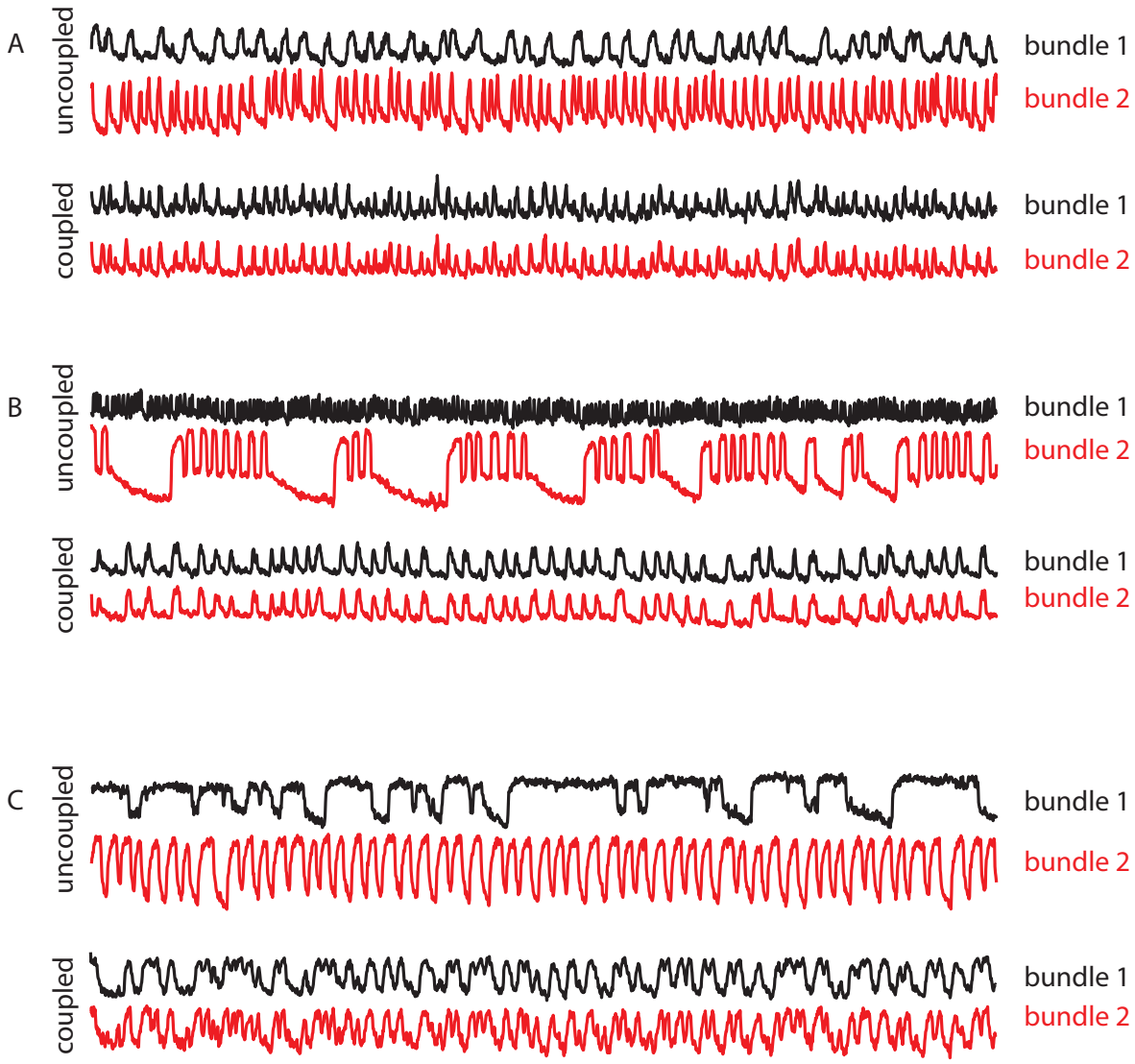

Figure 6.2: Synchronization of oscillating hair bundles
Examples of hair bundle motion before, and after mechanical coupling by a glass fiber. In each panel, the top (bottom) 2 traces represent uncoupled (coupled) hair bundle motion. Motion of the same hair bundle is plotted in the same color. (A) Coupling of single-mode oscillators. The coupled system exhibits variation in oscillation amplitude. (B) Coupling of single- and multi-mode oscillators. (C) Anomalous oscillation profile is sometimes observed upon coupling oscillators with significantly different profiles. All the recordings shown are 2 seconds.

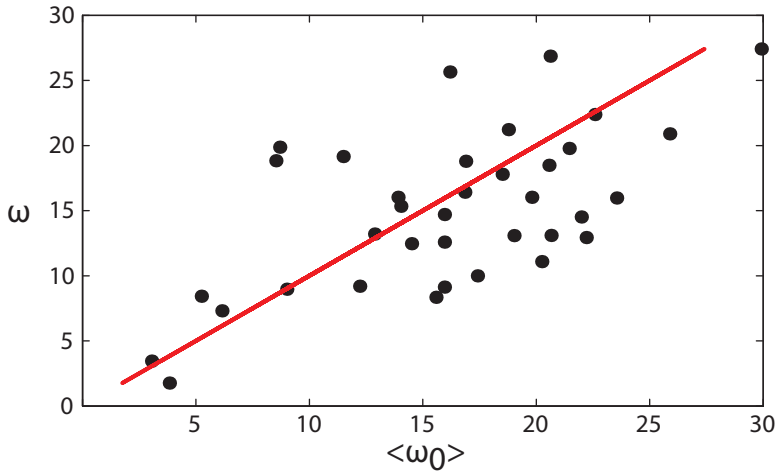

Figure 6.3: Characteristic frequency of the coupled systems
Characteristic frequency of mechanically coupled hair bundles as a function of the averaged characteristic frequency of the same bundles before coupling. Red line shows a linear dependence with slope = 1.

presumably due to small mechanical offsets and elastic loading imposed on hair bundles upon attachment of the glass fiber. Hence, the estimate of the averaged ω_0 did not accurately represent the actual frequency of an uncoupled hair bundle, with a fiber attached.

In order to estimate the noise level of the bundle motion, we extracted the phase of the oscillations, and calculated the effective diffusion coefficients (D_{eff}), following the procedure described in Chapter 4. D_{eff} represents the noise level of the system, with a larger value corresponding to a broader peak in the power spectral density (lower quality factor). The noise level did not exhibit any dependence on the difference between ω_0 of the bundles before coupling, Fig 6.4A. Moreover, D_{eff} obtained from the coupled systems, and those from single bundles with a fiber attached (different cells) were comparable, with the averaged value $\sim$62.7 for single bundles, and $\sim$70.3 for coupled bundles, shown in Fig. 6.4B.

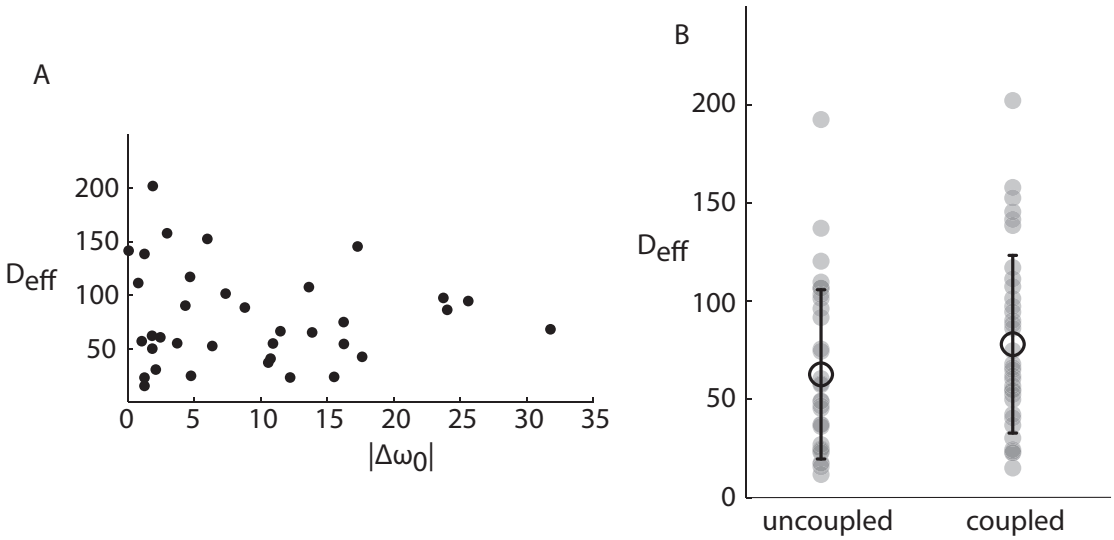

Figure 6.4: Effective diffusion coefficient of the phase of oscillations in coupled systems
(A) D_{eff} shows no dependence on the mismatch in the characteristic frequency of bundles before coupling. (B) Comparison between D_{eff} obtained from single and coupled bundles oscillations.

6.3.2 Compressive nonlinearity in the amplitude response of the coupled system

Next, we applied mechanical sinusoidal stimuli of different amplitudes to the base of the fiber. The stimulus frequency was chosen to match the characteristic frequency of the system (small detuning). Similar to single bundles, amplitude of the phase-locked response exhibited compressive nonlinearity, as shown in Fig 6.5. Note that, in this particular case, the regime of very small signal amplitude showed an expansive response, with a slope of $\sim$2 on the log-log plot.

To investigate the sensitivity to external stimuli of the coupled systems, the phase difference ($\Delta\phi(t)$) between the bundle oscillations and the stimulus was extracted. We calculated the variance (S) of the distribution of $\Delta\phi(t)$, such that complete phase-locking corresponded to $S = 0$, and the absence of phase-locking resulted in $S = 1$. We found that the variance decayed exponentially with stimulus amplitude, as shown in Fig 6.6A. The detection threshold was defined

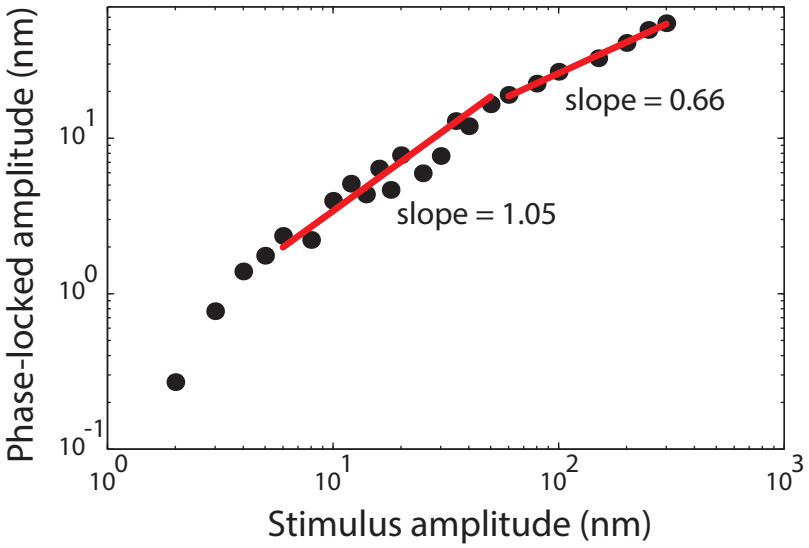

Figure 6.5: Compressive nonlinearity in phase-locked amplitude
Phase-locked amplitude obtained from the Fourier transform is shown as a function of stimulus amplitude, plotted on a log-log scale. Red lines show linear fits, with compressive nonlinearity corresponding to slope smaller than 1.

as the decay constant (Δ_c) obtained from the exponential fit. We then compared Δ_c obtained from the coupled systems, to those from single bundles, and found that the detection thresholds in both cases were comparable, with $< \Delta_c >_{single} = 0.88 \pm 0.57$pN (n = 14), and $< \Delta_c >_{coupled} = 0.93 \pm 0.7$pN (n = 13).

6.3.3 Frequency tuning of the coupled system

Phase-locked response to sinusoidal stimuli with different frequencies were also measured. The stimulus amplitude was fixed at 10 nm at the base of the fiber, corresponding to ∼1 pN force applied to a stationary bundle. The coupled system generally exhibited frequency selectivity, with the quality factor $\sim 1.24 \pm 0.36$ (n = 10), slightly larger than the value reported in single bundles [4]. The quality factor was found to be independent of the difference in ω_0 before coupling. In some cases, as illustrated in Fig. 6.7, the coupled system exhibited a sharp frequency tuning, with quality factor ∼3, larger than that observed in single bundles.

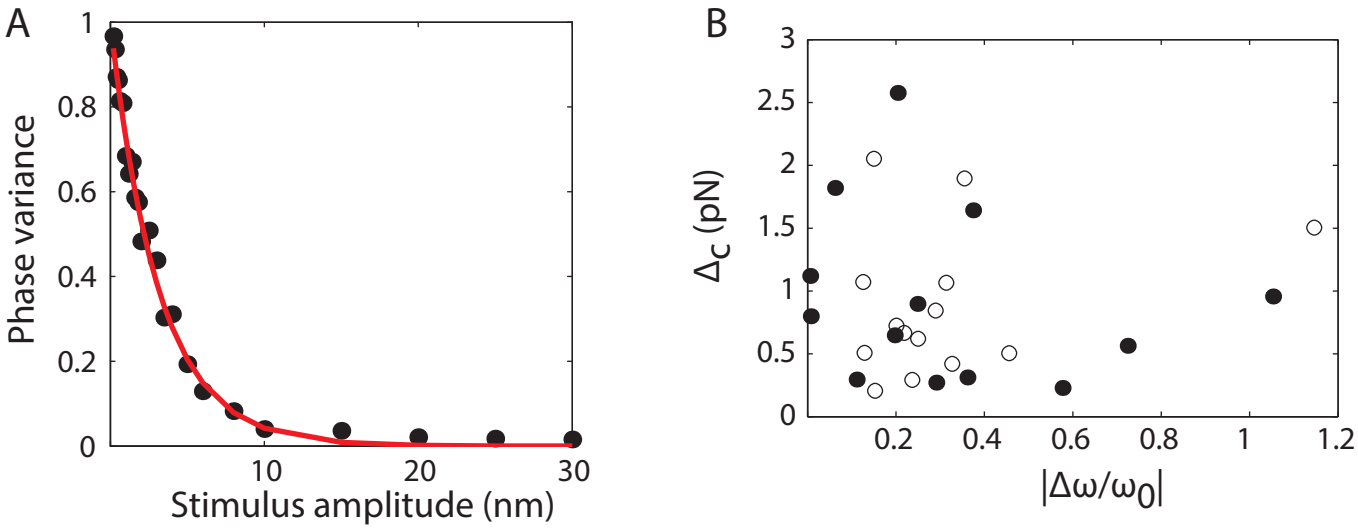

Figure 6.6: Detection threshold
(A) Phase variance (S) obtained from the distribution of phase difference decays with stimulus amplitude. Red line indicates an exponential fit. (B) Threshold of detection (Δ_c) does not depend on the mismatch between the characteristic frequency and the stimulus frequency. ω_0 is the characteristic frequency of hair bundles, coupled or uncoupled. There is no significant difference between the detection threshold of single (open circles) and coupled (filled circles) hair bundles.

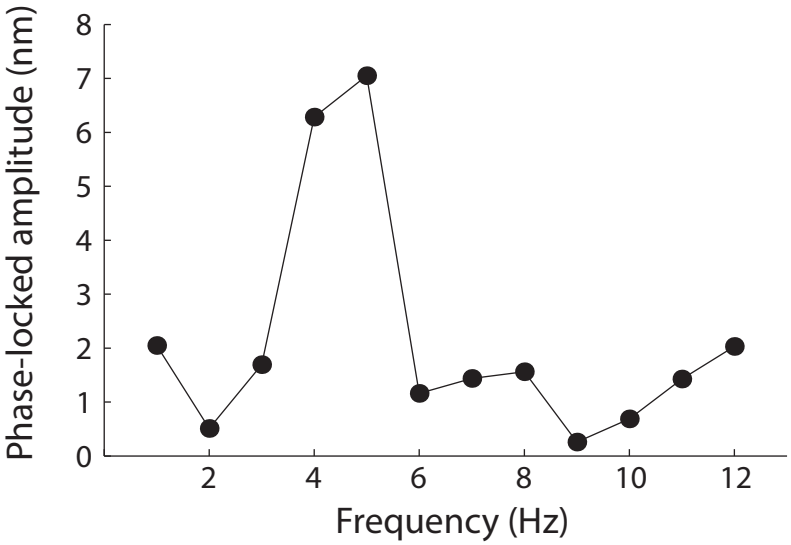

Figure 6.7: Frequency tuning
Phase-locked amplitude as a function of stimulus frequency. The stimulus amplitude was fixed at 10 nm. In this example, the quality factor is 3.18.

6.3.4 Effects of mechanical offsets

Finally, we explored the effects of mechanical offsets on spontaneous oscillation profile of the coupled systems. We imposed a slowly varying offset, as a triangular wave, to the base of the fiber. In some cases, the effects of mechanical offsets were similar to those observed in single hair bundles, described in Chapter 5, with positive offsets (toward the kinocilia) leading to faster, and smaller oscillations, and negative offset resulting in longer durations spent in the channel-closing state between oscillations, as illustrated in Fig 6.8A.

In most cases, however, due to the geometry of the system, one of the bundles could act as a pivot point and the probe appeared to rotate, thus imposing different offsets onto each bundle. As shown in Fig. 6.8B, the position of the bundle at the tip of the fiber (Fig 6.8B, black trace) seemed largely unaffected by the offset, while the other followed the imposed stimulus. As seen from the figure, positive offset led to a reduction in the oscillation frequency, and the suppression occurred in the channel-closing state. This might be due to the rotation of the probe, which imposed negative offsets to one of the bundles.

We also studied the transient response to step deflections of the coupled system. Upon negative deflection, the transient response was similar to those observed in single bundles, with the recovery of oscillation occurring following the channel-opening excursion, and the oscillation amplitude rapidly increasing, as shown in Fig. 6.9A. In some cases, the response to positive deflection was distinct from that observed in single bundles, in that the recovery of oscillation occurred via channel-opening, illustrated in Fig. 6.9B.

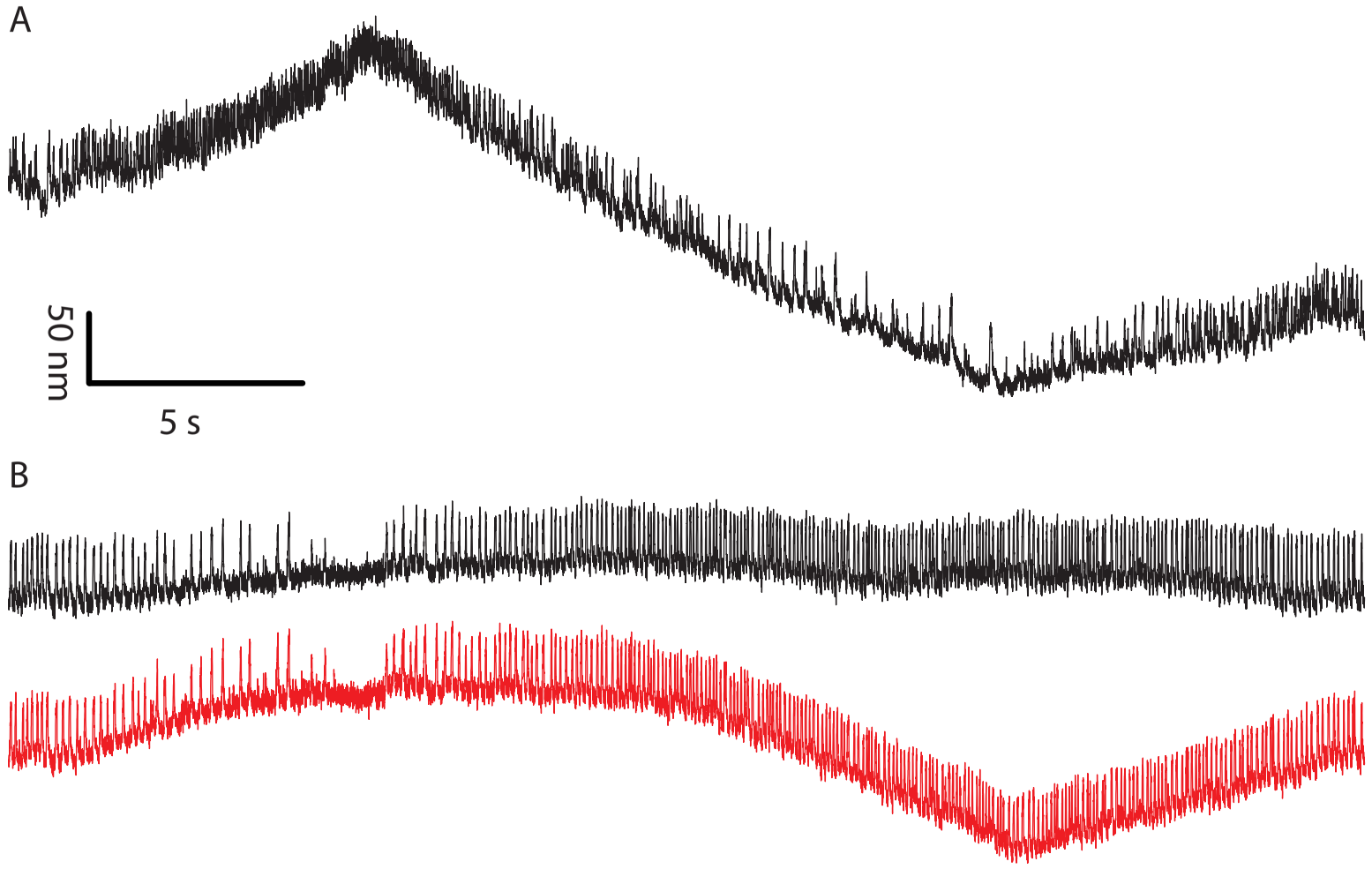

Figure 6.8: Effects of slow ramps

(A) Coupled hair bundle motion under a slow ramp. Only the motion of one bundle is shown since perfect synchronization was achieved in this example. (B) Coupled hair bundle motion under the same tricangular stimulus, during which probe rotation was observed. The offset of the bundle closer to the tip of the probe seemed unaffected. The oscillation profile near the suppression under positive offset was never observed in single bundles.

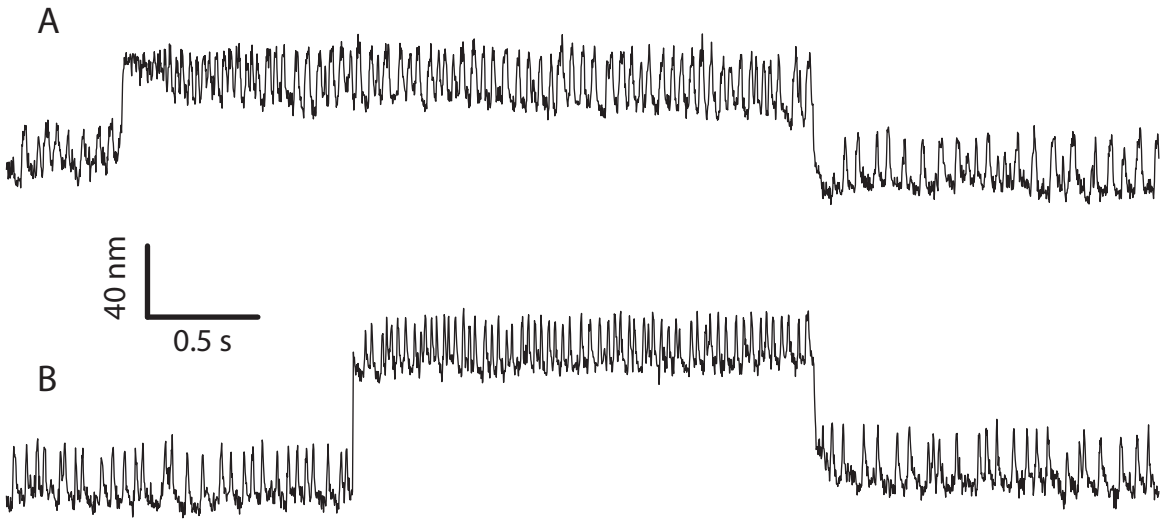

Figure 6.9: Transient response to step deflections
(A)Transient motion of coupled hair bundle under a positive step deflection. The response at the onset and after the step are similar to those observed in single bundles. (B) Anomalous response to positive step, where the recovery of the oscillation starts with channel-opening excursion.

6.4 Conclusion

Although hair bundles from the bullfrog sacculus possess an active process, manifested as spontaneous oscillations observed under *in vitro* conditions, these bundles do not oscillate when coupled to the otolithic membrane. There are several possibilities as to how the membrane suppresses their spontaneous activity. Apart from elastic and mass loading, the membrane seems to impose a mechanical offset on hair bundles, the effects of which was investigated in chapter 5. In this chapter, we explore another effect of otolithic membrane on bundles, mechanical coupling. We found that with large coupling strength, synchronized motion of hair bundles are always observed. The oscillation profile is similar to those of single bundles, with an exception of large variations in the oscillation amplitude. Calculation of diffusion coefficient indicates that the noise level in the coupled system is not significantly reduced. Analysis of the phase-locked response of the coupled system to mechanical sinusoidal stimuli of different amplitude and frequency showed

that a coupled system does not respond very differently from a single bundle; it exhibits a compressive nonlinearity, and comparable threshold. Frequency tuning, however, can be drastically enhanced in some cases.

CHAPTER 7

Conclusions

Detection of sound and seismic vibrations by the inner ear occurs when mechanical stimuli are converted into electrical signals. This process of mechano-electrical transduction is mediated by deflections of hair bundles, which leads to opening and closing of mechano-sensitive transduction channels located within the bundles. Understanding of mechanical entrainment of hair bundles is, therefore, a key to elucidating how the inner ear detects and amplifies the incoming signals. Under some *in vitro* conditions, hair bundles from some species can undergo spontaneous oscillations, a manifestation of active processes within the bundles. Prior experimental studies focus on entrainment of spontaneously oscillating hair bundles by sinusoidal stimuli [60, 61, 59]. The results support the theoretical description based on Hopf bifurcation, with observations of frequency selectivity, compressive nonlinearity, and amplification associated with active power generated by hair bundles in response to the stimuli. However, in most species, hair bundles are coupled to an overlying membrane, such as the otolithic membrane in bullfrog sacculus and the tectorial membrane in mammalian cochlea. Under the overlying structure, hair bundles are mutually coupled, and do not exhibit spontaneous movement. In this work, we study mechanical entrainment of active hair bundles whose spontaneous movements are suppressed via the application of offsets to the bundles' position, and entrainment of systems of two mutually coupled hair bundles.

Under *in vitro* conditions, a fraction of hair bundles exhibit spontaneous os-

cillation with a complex temporal profile, with oscillations interrupted by quiescent intervals, resulting in multimode oscillations. This behavior is more pronounced upon an application of small negative mechanical offsets [75]. This oscillation profile cannot be captured by the existing model of hair bundle dynamics [58, 63, 83, 36]. We propose an additional element of "variable gating spring" - a gating spring with calcium dependent stiffness with very slow dynamics with respect to those of the myosin motors. The variable gating spring enables us to reproduce a broad range of experimental data, including mechanical and chemical manipulations on hair bundles' spontaneous oscillations.

Prior studies indicate that hair bundles operate on different timescales: with fast adaptation occurring within a few ms, and slow adaptation within a few tens of ms [20]. The underlying mechanisms of both processes are thought to be mediated by calcium binding to different elements within the stereocilia, including myosin motors for the slow adaptation. Our results shown in Chapter 3 suggest the existence of another slow adaptation process occurring on the order of $\sim$100 ms, based on an assumption that calcium binding to an intracellular element can reduce the gating spring stiffness. In a recent study, oscillating hair bundles are found to undergo higher-order mode-locking to mechanical stimuli, with frequency much lower than the characteristic frequency of the bundles [75]. This indicates that the variable gating spring assists in entrainment of hair bundles by low-frequency stimuli.

Next, we study one-to-one mode-locking behavior of oscillating hair bundles with no additional offsets. In Chapter 4, we explore the time-dependent phase-locking dynamics under small sinusoidal stimuli. The stimulus frequency is chosen to match the characteristic frequency of the bundle. Very weak stimuli, with amplitude of $\sim$1.7 nm (0.4 pN), can evoke a peak in the histogram of the phase difference, indicating an exquisite sensitivity of the bundles. Further increase in stimulus amplitude reveals a time-dependent phase-locking behavior, with the

occurrence of phase slips. Various quantities extracted from experimental data show an agreement with predictions based on the stochastic Adler equation. This suggests that entrainment of hair bundles by small stimuli occurs via a SNIC bifurcation.

To further imitate a more natural condition, in which hair bundles are coupled to the otolithic membrane, we explore the entrainment of quiescent hair bundles in Chapter 5. Mechanical offsets are imposed onto the resting bundles' position to achieve suppression of oscillations. The spiking regime is observed in some fraction of hair bundles under large positive offsets. Upon application of sinusoidal stimulus, hair bundles are shown to amplify the signal by exhibiting spikes superposed onto the passive component of the response. Calculation of the vector strength indicates that spikes were at least twice more sensitive to external stimulus than limit-cycle oscillations. This suggests an amplification threshold of $\sim$1-nm stimulus. Spikes evoked in quiescent hair bundles by stimuli of different amplitudes and frequencies exhibited a constant amplitude, another indication of a system poised near a SNIC bifurcation.

Results from numerical simulations, based on the model developed in chapter 3, demonstrate that the slow adaptation process is not required for spike generation. Therefore, under a large positive offset imposed by the otolithic membrane, adaptation process presumably provides self-tuning to the system, such that the bundle is poised near the onset of the spontaneous activity. Small perturbations due to noise or external signals can thus evoke spikes. The system therefore relies on an incomplete adaptation to set the threshold of amplification.

Finally, we explore the effects of mechanical coupling on hair bundle entrainment. Synchronization between two oscillating hair bundles always occurs, with the oscillation profiles, in some cases, different from those observed in uncoupled bundles. Analysis of noise level in phase space, the detection threshold, and the frequency tuning do not show significant difference to those of single bundles.

However, mechanical response of some coupled hair bundles to a step deflection in positive direction showed anomalous behavior in hair bundle motion, with the recovery of the oscillations occurs via a channel-opening excursion. This implies a more complicated adaptation process due to interactions between the bundles, and also suggests our future direction in studying mechanical entrainment of coupled hair bundles under positive offsets.

APPENDIX A

Source Codes

Numerical simulations in this thesis were performed in Matlab. In order to include noise terms into the model, a home-built algorithm was developed following the Runge-Kutta fourth-order method. At each time step of the calculation, a random number was generated. The source codes are included as followed.

A.1 Solver

```
function X = ode4(odefun,f,A,kf,tspan,x0,noise)
%f = frequency of sinusoidal stimulus
%A = amplitude of sinusoidal stimulus
%kf = stiffness of stimulus fiber
%x0 = initial conditions
%noise = 0 for deterministic calculation, and 1 for calculation with
%fluctuations

L = length(tspan);
N = length(x0);
X = zeros(N,L);
k1 = zeros(N,L);
k2 = zeros(N,L);
k3 = zeros(N,L);
k4 = zeros(N,L);
h = diff(tspan);
```

```
%initial position
X(:,1) = x0;

for i = 1:L-1
    ti = tspan(i);
    hi = h(i);
    xi = X(:,i);
    k1(:,i) = hi*odefun(f,A,kf,ti,xi,noise);
    k2(:,i) = hi*odefun(f,A,kf,ti+0.5*hi,xi+0.5*k1(:,i),noise);
    k3(:,i) = hi*odefun(f,A,kf,ti+0.5*hi,xi+0.5*k2(:,i),noise);
    k4(:,i) = hi*odefun(f,A,kf,ti+hi,xi+k3(:,i),noise);
    X(:,i+1) = xi+(1/6)*(k1(:,i)+2*k2(:,i)+2*k3(:,i)+k4(:,i));
end
```

A.2 Numerical Model

```
function xdot = hairmechn3(f,A,kpro,t,x,noise)

xp = x(1);
xa = x(2);
pr = x(3);
pm = x(4);

global x1
global xa1
global pr1
global pm1
global p


if t == 0
```

```
    x1 = x(1);
    xa1 = x(2);
    pr1 = x(3);
    pm1 = x(4);
end

noisefac = 1;
%constants
F = 96490;              %Faraday constant   (C/mol)
z = 2.;                 %valence of calcium ion
T = 300;
a = 0.;                 %coupling parameter for cca
e = 1.6*(10^-19);
kb = 1.381*(10^-23);

%calcium current
dca = 800.*(10^-12);  %diffusion coefficient of free calcium (m^2/s)
pca = 1.*(10^-18);    %calcium permeability of transduction channel (m^3/s)
vm0 = -50.*(10^-3);   %resting membrane potential of hair cell (V)
ccaext = 0.25*(10^-3);%extracellular calcium concentration (M)
ccasoma = 50.*(10^-9);%resting intracellular calcium concentration (M)

%geometrical parameters
gamma = 0.14;             %geometric factor
si = (130+370).*(10^-9); %drag coefficient of hair bundle (Ns/m)

if kpro == 0
    si = 130*10^(-9);    %drag without glass fiber
end
n = 45;                 %number of transduction channels
d = 7*(10^-9);          %swing of transduction channel's gate (m)
kes = 140.*(10^-6);     %stiffness of adaptation extent spring (N/m)
rm =20.*(10^-9);        %distance from the channel to adaptation motor's
                        %binding site (m)
```

```
%adaptation
kmon =30*(10^6); %rate constant for calcium binding to adaptation motor (1/sM)
kmoff =15*10^3;  %rate constant for calcium unbinding to adaptation motor (1/s)
kmr = kmoff/kmon;%ratio kmoff/kmon

smin =1.5*10^(3);  %minimum rate constant for motor slipping (m/sN)
cmin = 0;          %minimum rate constant for motor climbing (m/s)
smax = 170*10^(3); %maximum rate constant for motor slipping (m/sN)
cmax = 0.05*(10^-6); %maximum rate constant for motor climbing (m/s)

xsp = 2.5*10^(-7); %resting position of the bundle without the tip link (m)
xes = 8*10^(-8);   %resting position of the extension spring (m)
xc = 18*(10^-9);   %extension of spring due to channels closing (m)

ksp =310*10^(-6);  %stiffness of the stereociliary pivot (N/m)

kgszero =1500;     %tip link stiffness in the absence of calcium (10^-6 N/m)
kgsone = -1000;    %maximal reduction in tip link stiffness in the presence
                   %of calcium (10^-6 N/m)
kron = 5*10^(6);   %binding rate of calcium to variable gating spring
kroff = 5;         %unbinding rate of calcium from variable gating spring

%calculation of parameters at resting position
nbsite = 1;
p0 = 0.5;     %channel open probability at rest
Ica0 = p0*pca*(z^2)*e*F*vm0*ccaext/(kb*T*(1-exp(z*e*vm0/(kb*T))));
%calcium influx through channels at rest
ccam0 = -Ica0/(2*pi*z*F*dca*rm)+ccasoma;
%calcium concentration at the motor at rest
pr0 = 1/(1+(kroff/kron)/(ccam0));
%probability of calcium binding to variable gating spring at rest
pm0 = 1/(1+(kmr)/ccam0); %probability of calcium binding to the motor at rest
kgs0 = kgszero+kgsone*pr0; %gating spring stiffness at rest
```

```
C0 = (1-pm0)*(cmax-cmin)+cmin; %rate of myosin climing at rest

deltae0 = (kb*T)*log((1/p0)-1)+kgs0*10^(-6)*d*(xc-d/2);
%difference in energy between open and closed states

%calculate p when t=0
if t == 0
    kgs1 = kgszero+kgsone*pr1;
    p = 1/(1+exp((deltae0-kgs1*10^(-6)*d*(gamma*x1-xa1+xc-d/2))/(kb*T)));
end

%parameters in dynamics
vm = vm0;
Ica = p*pca*(z^2)*e*F*vm*ccaext/(kb*T*(1-exp(z*e*vm/(kb*T))));
%calcium influx through channel

%noise in calcium concentration at the motor
tc = 10^(-3);
Cm = -(pca*(z^2)*e*F*vm*ccaext/(kb*T*(1-exp(z*e*vm/(kb*T)))))/(2*pi*z*F*dca*rm)
     +ccasoma+a*ccasoma;
sig3 = sqrt(2*2*(Cm^2)*(1/n)*p*(1-p)*tc);
n3 =sig3*randn;

if noise == 0
    n3 = 0;
end

ccam = (-Ica/(2*pi*z*F*dca*rm)+(1-a)*ccasoma+a*ccasoma+noisefac*n3)*(1.);
%calcium concentration at the motor
if ccam<0
    ccam = 0;
end
```

```
kgs = kgszero+kgsone*pr;

if kgs<0
    pr0
    pr
    error('negative kgs')
end

s = nbsite*pm*(smax-smin)+smin;
C = C0;
p = 1/(1+exp((deltae0-kgs*10^(-6)*d*(gamma*xp-xa+xc-d/2))/(kb*T)));
%probability of channel opening

%noise in passive bundle motion
lambda = si;
sig1 = sqrt(2*kb*T*lambda/0.0001);
n11 = sig1*randn;
n1 = n11+0;

%noise in adaptation motor position
lambdaa = 10*10^(-6);
sig2 = sqrt(3*kb*T*lambdaa/0.0001);
n2 = sig2*randn;

if noise == 0
    n1 = 0;
    n2 = 0;
end

%stimulation
xpro = A*10^(-9)*sin(2*pi*f*t);
fstim = kpro*(xpro-xp)-00*10^(-9)*xpro;
forceramp = 52*10^-12;
```

```
%Differential equations
pos = gamma*xp-xa+xc-p*d;
alpha = 0;
mult = 1;

xpprime = (1/si)*(-n*gamma*kgs*10^(-6)*(pos)-ksp*(xp-xsp)-ksp*alpha)
          +(1/si)*fstim+(1.*noisefac*n1/si)+(forceramp/si);
xaprime = mult*(-C+s*(kgs*10^(-6)*(pos+abs(pos))/2-kes*(xa-xes)-kes*alpha))
          +noisefac*n2*gamma/(lambdaa);
prprime = (1-pr)*ccam*kron-kroff*pr;
pmprime = (1-pm)*ccam*kmon-kmoff*pm;

xdot = [xpprime;xaprime;prprime;pmprime];
end
```

References

[1] K.-H. Ahn. Enhanced signal-to-noise ratios in frog hearing can be achieved through amplitude death. *J. R. Soc. Interface*, 10:20130525, 2013.

[2] V. Ambegaokar and B. I. Halperin. Voltage due to thermal noise in the dc josephson effect. *Phys. Rev. Letts.*, 22:1364 – 1366, 1969.

[3] J. A. Assad, G. M. Shepherd, and D. P. Corey. Tip-link integrity and mechanical transduction in vertebrate hair cells. *Neuron*, 7:985 – 994, 1991.

[4] J. Barral, K. Dierkes, B. Lindner, F. Julicher, and P. Martin. Coupling a sensory hair-cell bundle to cyber clones enhances nonlinear amplification. *Proc. Natl. Acad. Sci.*, 107:8079 – 8084, 2010.

[5] M. E. Benser, N. P. Issa, and A. J. Hudspeth. Hair-bundle stiffness dominates the elastic reactance to otolithic membrane shear. *Hear. Res.*, 68:243 – 252, 1993.

[6] M. E. Benser, R. E. Marquis, and A. J. Hudspeth. Rapid, active hair bundle movements in hair cells from the bullfrog?s sacculus. *J. Neurosci.*, 16:5629 – 5643, 1996.

[7] M. Beurg, M. G. Evans, C. M. Hackney, and R. Fettiplace. A large-conductance calcium-selective mechanotransducer channel in mammalian cochlear hair cells. *J. Neurosci*, 26:10992 – 11000, 2006.

[8] M. Beurg, R. Fettiplace, J.-H. Nam, and A. J. Ricci. Localization of inner hair cell mechanotransducer channels using high-speed calcium imaging. *Nat Neurosci*, 12:553 – 558, 2009.

[9] S. Boccaletti, E. Allaria, R. Meucci, and F. T. Arecchi. Experimental characterization of the transition to phase synchronization of chaotic co_2 laser systems. *Phys. Rev. Lett.*, 89:194101, 2002.

[10] D. Bozovic and A. J. Hudspeth. Hair-bundle movements elicited by transepithelial electrical stimulation of hair cells in the sacculus of the bullfrog. *Proc. Natl. Acad. Sci.*, 100:958 – 963, 2003.

[11] S. Camalet, T. Duke, F. Julicher, and J. Prost. Auditory sensitivity provided by self-tuned critical oscillations of hair cells. *Proc. Natl. Acad. Sci.*, 97:3183 – 3188, 2000.

[12] M. Castellano-Munoz, S. H. Israel, and A. J. Hudspeth. Efferent control of the electrical and mechanical properties of hair cells in the bullfrog's sacculus. *PLoS ONE*, 5:e13777, 2010.

[13] C. H. Chabbert. Heterogeneity of hair cells in the bullfrog sacculus. *Eur. J. Physiol.*, 435:82–90, 1997.

[14] E. L. M. Cheung and D. P. Corey. Ca^{2+} changes the force sensitivity of the hair-cell transduction channel. *Biophys. J.*, 90:124 – 139, 2006.

[15] Y. Choe, M. O. Magnasco, and A. J. Hudspeth. A model for amplification of hair-bundle motion by cyclical binding of ca^{2+} to mechanoelectrical transduction channels. *Proc. Natl. Acad. Sci.*, 95:15321 – 15326, 1998.

[16] D. P. Corey and A. J. Hudspeth. Kinetics of the receptor current in bullfrog saccular hair cells. *J. Neurosci.*, 3:962 – 976, 1983.

[17] A. C. Crawford and R. Fettiplace. The mechanical properties of ciliary bundles of turtle cochlear hair cells. *J. Physiol.*, 364:359 – 379, 1985.

[18] W. Denk, W. W. Webb, and A. J. Hudspeth. Mechanical properties of sensory hair bundles are reflected in their brownian motion measured with a laser differential interferometer. *Proc. Natl. Acad. Sci.*, 86:5371 – 5375, 1989.

[19] K. Dierkes, B. Lindner, and F. Julicher. Enhancement of sensitivity gain and frequency tuning by coupling of active hair bundles. *Proc. Natl. Acad. Sci.*, 105:18669 – 18674, 2008.

[20] R. A. Eatock. Adaptation in hair cells. *Annu. Rev. Neurosci.*, 23:285 – 314, 2000.

[21] R. A. Eatock, D. P. Corey, and A. J. Hudspeth. Adaptation of mechanoelectrical transduction in hair cells of the bullfrog's sacculus. *J. Neurosci.*, 7:2821 – 2836, 1987.

[22] V. M. Eguiluz, M. Ospeck, Y. Choe, A. J. Hudspeth, and M. O. Magnasco. Essential nonlinearities in hearing. *Phys. Rev. Lett.*, 84:5232 – 5235, 2000.

[23] A. Flock, B. Flock, and E. Murray. Studies on the sensory hairs of receptor cells in the inner ear. *Acta Otolaryngol.*, 83:85 – 91, 1977.

[24] L. Fredrickson-Hemsing, S. Ji, R. Bruinsma, and D. Bozovic. Mode-locking dynamics of hair cells of the inner ear. *Phys. Rev. E*, 86:021915, 2012.

[25] L. Fredrickson-Hemsing, C. E. Strimbu, Y. Roongthumskul, and D. Bozovic. Dynamics of freely oscillating and coupled hair cell bundles under mechanical deflection. *Biophys. J.*, 102:1785 – 1792, 2012.

[26] J. A. Garcia, A. G. Yee, P. G. Gillespie, and D. P. Corey. Localization of myosin-iβ near both ends of tip links in frog saccular hair cells. *J. Neurosci.*, 18:8637 – 8647, 1998.

[27] P. G. Gillespie and D. P. Corey. Myosin and adaptation by hair cells. *Neuron*, 19:955 – 958, 1997.

[28] P. G. Gillespie and J. L. Cyr. Myosin-1c, the hair cell's adaptation motor. *Annu. Rev. Physiol.*, 66:521 – 545, 2004.

[29] P. G. Gillespie, R. A. Dumont, and B. Kachar. Have we found the tip link, transduction channel, and gating spring of the hair cell? *Curr. Opin. Neurobiol.*, 15:389–396, 2005.

[30] P. G. Gillespie and A. J. Hudspeth. Pulling springs to tune transduction: adaptation by hair cells. *Neuron*, 12:1 – 9, 1994.

[31] P. G. Gillespie, M. C. Wagner, and A. J. Hudspeth. Identification of a 120 kd hair-bundle myosin located near stereociliary tips. *Neuron*, 11:581 – 594, 1993.

[32] L. Le Goff, D. Bozovic, and A. J. Hudspeth. Adaptive shift in the domain of negative stiffness during spontaneous oscillatfion by hair bundles from the internal ear. *Proc. Natl. Acad. Sci.*, 102:16996 – 17001, 2005.

[33] R. E. Goldstein, M. Polin, and I. Tuval. Noise and synchronization in pairs of beating eukaryotic flagella. *Phys. Rev. Lett.*, 103:168103, 2009.

[34] C. Gosse and V. Croquette. Magnetic tweezers: micromanipulation and force measurement at the molecular level. *Biophys. J.*, 82:3314 – 3329, 2002.

[35] N. Hacohen, J. A. Assad, W. J. Smith, and D. P. Corey. Regulation of tension on hair-cell transduction channels: displacement and calcium dependence. *J. Neurosci.*, 9:3988 – 3997, 1989.

[36] L. J. Han and A. B. Neiman. Spontaneous oscillations, signal amplification, and synchronization in a model of active hair bundle mechanics. *Phys. Rev. E*, 81:041913, 2010.

[37] T. Hasson, P. G. Gillespie, J. A. Garcia, R. B. MacDonald, and Y. Zhao. Unconventional myosin's in inner-ear sensory epithelia. *J. Cell Biol.*, 137:1287 – 1307, 1997.

[38] B. Hille. *Ion channels of excitable membranes*. Sinauer Associates Inc., Sunderland, MA, third edition, 2001.

[39] J. R. Holt, S. K. H. Gillespie, D. W. Provance Jr., K. Shah, K. M. Shokat, D. P. Corey, J. A. Mercer, and P. G. Gillespie. A chemical-genetic strategy implicates myosin-1c in adaptation by hair cells. *Cell*, 108:371 – 381, 2002.

[40] T. Holton and A. J. Hudspeth. The transduction channel of hair cells from the bullfrog characterized by noise analysis. *J. Physiol.*, 375:195 – 227, 1986.

[41] J. Howard and A. J. Hudspeth. Mechanical relaxation of the hair bundle mediates adaptation in mechanoelectrical transduction by the bullfrog's saccular hair cell. *Proc. Natl. Acad. Sci.*, 84:3064 – 3068, 1987.

[42] J. Howard and A. J. Hudspeth. Compliance of the hair bundle associated with gating of mechanoelectrical transduction channels in the bullfrog's saccular hair cell. *Neuron*, 1:189 – 199, 1988.

[43] A. J. Hudspeth. The cellular basis of hearing: the biophysics of hair cells. *Science*, 230:745 – 752, 1985.

[44] A. J. Hudspeth. Making an effort to listen: Mechanical amplification in the ear. *Neuron*, 59:530 – 545, 2008.

[45] A. J. Hudspeth, Y. Choe, A. D. Mehta, and P. Martin. Putting ion channels to work: Mechanoelectrical transduction, adaptation, and amplification by hair cells. *Proc. Natl. Acad. Sci.*, 97:11765 – 11772, 2000.

[46] A. J. Hudspeth and R. S. Lewis. Kinetic analysis of voltage- and ion-dependent conductances in saccular hair cells of the bull-frog, *Rana Catesbeiana*. *J. Physiol.*, 400:237 – 274, 1988.

[47] E. M. Izhikevich. Neural excitability, spiking and bursting. *Int. J. Bifurc. Chaos*, 10:1171 – 1266, 2000.

[48] B. Kachar, M. Parakkal, and J. Fex. Structural basis for mechanical transduction in the frog vestibular sensory apparatus: I. the otolithic membrane. *Hear. Res.*, 45:179 – 190, 1990.

[49] B. Kachar, M. Parakkal, M. Kurc, Y Zhao, and P. G. Gillespie. High-resolution structure of hair-cell tip links. *Proc. Natl. Acad. Sci.*, 97:13336 – 13341, 2000.

[50] E. R. Kandel, J. H. Schwartz, and T. M. Jessell, editors. *Principles of neural science*. Elsevier Science Publishing Co., Inc., New York, NY, third edition, 1991.

[51] D. T. Kemp. Evidence of mechanical nonlinearity and frequency selective wave amplification in the cochlea. *Arch. Oto.-Rhino.-Laryngol.*, 224:37 – 45, 1979.

[52] H. Koyama, E. R. Lewis, E. L. Leverenz, and R. A. Baird. Acute seismic sensitivity in the bullfrog ear. *Brain Res.*, 250:168 – 172, 1982.

[53] A. S. Kozlov, T. Risler, and A. J. Hudspeth. Coherent motion of stereocilia assures the concerted gating of hair-cell transduction channels. *Nat. Neurosci.*, 10:87 – 92, 2007.

[54] L. D. Landau and E. M. Lifshitz. *Theory of elasticity.* Butterworth-Heinemann, Burlington, MA, 1986.

[55] B. Lindner, K. Dierkes, and F. Julicher. Local exponents of nonlinear compression in periodically driven noisy oscillators. *Phys. Rev. Lett.*, 103:250601, 2009.

[56] E. A. Lumpkin and A. J. Hudspeth. Detection of ca2+ entry through mechanosensitive channels localizes the site of mechanoelectrical transduction in hair cells. *Proc. Natl. Acad. Sci.*, 92:10297 – 10301, 1995.

[57] D. Ó Maoiléidigh, E. M. Nicola, and A. J. Hudspeth. The diverse effects of mechanical loading on active hair bundles. *Proc. Natl. Acad. Sci.*, 109:1943 – 1948, 2012.

[58] P. Martin, D. Bozovic, Y. Choe, and A. J. Hudspeth. Spontaneous oscillation by hair bundles of the bullfrog's sacculus. *J. Neurosci.*, 23:4533 – 4548, 2003.

[59] P. Martin and A. J. Hudspeth. Active hair-bundle movements can amplify a hair cell's response to oscillatory mechanical stimuli. *Proc. Natl. Acad. Sci.*, 96:14306 – 14311, 1999.

[60] P. Martin and A. J. Hudspeth. Compressive nonlinearity in the hair bundle's active response to mechanical stimulation. *Proc. Natl. Acad. Sci.*, 98:14386 – 14391, 2001.

[61] P. Martin, A. J. Hudspeth, and F. Julicher. Comparison of a hair bundle's spontaneous oscillations with its response to mechanical stimulation reveals the underlying active process. *Proc. Natl. Acad. Sci.*, 98:14380 – 14385, 2001.

[62] P. Martin, A. D. Mehta, and A. J. Hudspeth. Negative hair-bundle stiffness betrays a mechanism for mechanical amplification by the hair cell. *Proc. Natl. Acad. Sci.*, 97:12026 – 12031, 2000.

[63] B. Nadrowski, P. Martin, and F. Julicher. Active hair-bundle motility harnesses noise to operate near an optimum of mechanosensitivity. *Proc. Natl. Acad. Sci.*, 101:12195 – 12200, 2004.

[64] A. Pikovsky, M. Rosenblum, and J. Kurths. *Synchronization: A universal concept in nonlinear sciences.* Cambridge University Press, Cambridge, England, 2001.

[65] R. Probst, B. L. Lonsbury-Martin, and G. K. Martin. Review of otoacoustic emissions. *J. Acoust. Soc. Am.*, 89:2027 – 2067, 1991.

[66] D. Purves, G. J. Augustine, D. Fitzpatrick, L. C. Katz, A.-S. LaMantia, J. O. McNamara, and S. M. Williams, editors. *Neuroscience.* Sinauer Associates Inc., Sunderland, MA, second edition, 2001.

[67] D. Ramunno-Johnson, C. E. Strimbu, L. Fredrickson, K. Arisaka, and D. Bozovic. Distribution of frequencies of spontaneous oscillations in hair cells of the bullfrog sacculus. *Biophys. J.*, 96:1159 – 1168, 2009.

[68] D. Ramunno-Johnson, C. E. Strimbu, A. Kao, L. Fredrickson Hemsing, and D. Bozovic. Effects of the somatic ion channels upon spontaneous mechanical oscillations in hair bundles of the inner ear. *Hear. Res.*, 268:163 – 171, 2010.

[69] P. Reimann, C. Van dan Broeck, H. Linke, P. Hanggi, J. M. Rubi, and A. Perez-Madrid. Diffusion in tilted periodic potentials: Enhancement, universality, and scaling. *Phys. Rev. E*, 65:031104, 2002.

[70] L. Robles and M. A. Ruggero. Mechanics of the mammalian cochlea. *Physiol. Rev.*, 81:1305 – 1352, 2001.

[71] M. A. Ruggero and N. C. Rich. Application of a commercially-manufactured doppler-shift laser velocimeter to the measurement of basillar-membrane vibration. *Hear. Res.*, 51:215 – 230, 1991.

[72] M. A. Ruggero, N. C. Rich, A. Recio, S. S. Narayan, and L. Robles. Basilar-membrane responses to tones at the base of the chinchilla cochlea. *J. Acoust. Soc. Am.*, 101:2151 – 2163, 1997.

[73] M. A. Rutherford and W. M. Roberts. Spikes and membrane potential oscillations in hair cells generate periodic afferent activity in the frog sacculus. *J. Neurosci.*, 29:10025 – 10037, 2009.

[74] G. M. G. Shepherd and D. P. Corey. The extent of adaptation in bullfrog saccular hair cells. *J. Neurosci.*, 14:6217 – 6229, 1994.

[75] R. Shlomovitz, L. Fredrickson-Hemsing, A. Kao, S. W. F. Meenderink, R. Bruinsma, and D. Bozovic. Low frequency entrainment of oscillatory bursts in hair cells. *Biophys. J.*, 104:1661 – 1669, 2013.

[76] R. Shlomovitz, Y. Roongthumskul, R. Bruinsma, and D. Bozovic. Phase-locked spiking and stochastic resonance of hair cells. *Interface focus*, 2014. submitted.

[77] M. S. Smotherman and P. M. Narins. Hair cells, hearing and hopping: A field guide to hair cell physiology in the frog. *J. Exp. Biol.*, 203:2237 – 2246, 2000.

[78] M. Sotomayor, D. P. Corey, and K. Schulten. In search of the hair-cell gating spring: Elastic properties of ankyrin and cadherin repeats. *Structure*, 13:955 – 959, 2005.

[79] M. Sotomayor, W. A. Weihofen, R. Gaudet, and D. P. Corey. Structure of a force-conveying cadherin bond essential for inner-ear mechanotransduction. *Nature*, 492:128 – 132, 2012.

[80] C. E. Strimbu, A. Kao, J. Tokuda, D. Ramunno-Johnson, and D. Bozovic. Dynamic state and evoked motility in coupled hair bundles of the bullfrog sacculus. *Hear. Res.*, 265:38 – 45, 2010.

[81] S. H. Strogatz. *Nonlinear dynamics and chaos*. Westview Press, Cambridge, MA, 1994.

[82] B. Sul and K. H. Iwasa. Gating of two mechanoelectrical transducer channels associated with a single tip link. *Biophys. J.*, 99:1027 – 1033, 2010.

[83] J. Y. Tinevez, F. Julicher, and P. Martin. Unifying the various incarnations of active hair-bundle motility by the vertebrate hair cell. *Biophys. J.*, 93:4053 – 4067, 2007.

[84] M. Tinkham. *Introduction to superconductivity*. McGrawHill, New York, 1996.

[85] M. A. Vollrath, K. Y. Kwan, and D. P. Corey. The micromachinery of mechanotransduction in hair cells. *Annu. Rev. Neurosci.*, 30:339 – 365, 2007.

[86] E. N. Yamoah, E. Lumpkin, R. A. Dumont, P. J. S. Smith, A. J. Hudspeth, and P. G. Gillespie. Plasma membrane ca^{2+}-atpase extrudes ca^{2+} from hair cell stereocilia. *J. Neurosci.*, 18:610 – 624, 1998.